ULTRAFAST LASER DRIVEN SPIN GENERATION IN METALLIC FERROMAGNETS

BY

GYUNG-MIN CHOI

DISSERTATION

Submitted in partial fulfillment of the requirements
for the degree of Doctor of Philosophy in Materials Science and Engineering
in the Graduate College of the
University of Illinois at Urbana-Champaign, 2015

Urbana, Illinois

Doctoral Committee:

Professor David G. Cahill, Chair
Professor Jian-Min Zou
Assistant Professor Daniel P. Shoemaker
Assistant Professor Matthew Gilbert

ABSTRACT

This dissertation presents experimental studies of spin generation in metallic ferromagnets (FM) driven by ultrafast laser light using a pump-probe technique. The pump light gives a driving force for spin generation by depositing energy or spin angular momentum on FM. The probe light measures spin responses by magneto-optical Kerr effect or temperature responses by time-domain thermoreflectance. I find that ultrafast laser light generates spins in FM in three distinct mechanisms: (i) demagnetization; (ii) spin-dependent Seebeck effect (SDSE); (iii) optical helicity.

The demagnetization-driven spin generation is due to energy transport between electrons and magnons of FM and conservation of angular momentum for electron-magnon coupling. Ultrafast laser light deposits its energy in electrons of metallic layers and leads to a sharp increase of the electron temperature. The excited electrons transport energy to magnons of FM by the electron-magnon coupling. The magnon excitation results in ultrafast demagnetization of FM. I find that the spin loss by magnon excitations during the demagnetization process is converted to the spin generation in electrons of FM by the conservation of angular momentum for electron-magnon coupling. The generated spins diffuse to other layers and leads to spin accumulation in nonmagnetic metals (NM) or spin transfer torque on other FMs. I measure the demagnetization-driven spin accumulation in a NM/FM1/NM structure and spin transfer torque in a NM/FM1/NM/FM2 structure.

The SDSE-driven spin generation is due to a heat current at FM/NM interfaces and spin-dependent Seebeck coefficient of FM. Ultrafast laser light deposits its energy in a heat absorbing layer of a multilayer structure and leads to a heat current from the heat absorbing layer to heat sinking layer. When an FM is incorporated in the multilayer structure, the spin-dependent Seebeck

coefficient of FM converts the heat current to spin generation at interfaces between FM and NM. The interfacial spin generation rate is proportional to the heat current through FM and spin-dependent Seebeck coefficient of FM. I find that the heat current and spin-dependent Seebeck coefficient can be controlled by thickness of the heat sink layer and composition of FM, respectively. The generated spins diffuse to other layers and leads to spin accumulation on NM or spin transfer torque on other FM. I measure the SDSE-driven spin accumulation in a NM/FM1/NM structure and spin transfer torque in a NM/FM1/NM/FM2 structure.

The optical helicity-driven spin generation is due to angular momentum transport between light and electrons of FM and spin-orbit splitting of FM. A circularly polarized light with a wavelength of 785 nm triggers a dipolar transition from occupied 3*d* to unoccupied 4*p* bands of 3*d* transition FMs. The selection rule predicts a significant spin polarization for the dipolar transition from spin-orbit 3*d*-sub-bands ($3d_{3/2}$ and $3d_{5/2}$) to 4*p* band. However, energy degeneracy between $3d_{3/2}$ and $3d_{5/2}$ leads to zero spin polarization. I find that a small-but-finite spin-orbit splitting of the 3*d* bands leads to a finite spin generation from a circularly polarized light. The generated spins in electrons can be absorbed by magnetization of FM and lead to spin transfer torque. I measure the optical helicity-driven spin transfer torque in a single FM structure.

Dedicated to my parents, Ju-Taek Choi and Cha-Ja Ha,

and my wife, Mi-Youn Ham,

for their love and supports.

ACKNOWLEDGEMENTS

I am deeply grateful to my Ph.D. advisor, Prof. David Cahill, for his support, encouragement, and inspiration throughout my Ph.D. study. Due to his open mind and challenge spirit, I was able to study new research area of spin generation by ultrafast laser. During my Ph.D. study, I was truly impressed by his physical intuition and scrupulous attitude for experiment. I will always remember his guidance to do research after my Ph.D.

I also would like to appreciate my collaborators in Korea, Dr. Byoung-Chul Min in Korea Institute of Science and Technology and Prof. Kyung-Jin Lee and Mr. Chul-Hyun Moon in Korea University, for their cooperation and discussion. Their collaboration has a detrimental role for integrity and productivity in my research during my Ph.D.

I also want to thank all members of Prof. Cahill's group: Dr. Yee-Kan Koh, Dr. Joseph Feser, Dr. Xiaojia Wang, Dr. Jun Liu, Dr. Johannes Kimling, Dr. Judith Kimling, Dr. Ji-Yong Park, Trong Tong, Wei Wang, Gregory Hohensee, Richard Wilson, Jong-Lo Park, Dongyao Lee, Hyejin Zang, Ella Pek. Many thanks for their help in experiments and discussions. In addition, special thanks to Prof. Robert Averback and his students, Dr. Xuan Zhang, Calvin Lear, and Jae-Yel Lee, for their help in preparation of my samples.

Finally, I am grateful to my parents, Ju-Taek Choi and Cha-Ja Ha, and my wife, Mi-Youn Ham, for their love and support.

This work was partially supported by the US Department of Energy Office of Basic Energy Science under grant No. DE-FG02-07ER46459 and by the Army Research Office under grant No. W911NF-14-1-0016.

TABLE OF CONTENTS

LIST OF ACRONYMS

TRMOKE	Time-resolved Magneto-optical Kerr Effect
TDTR	Time-domain Thermoreflectance
FM	Ferromagnetic Metal
NM	Nonmagnetic Metal
STT	Spin Transfer Torque
2TM	Two Temperature Model
3TM	Three Temperature Model
SDSE	Spin-dependent Seebeck Effect
SSE	Spin Seebeck Effect
DOS	Density of States

CHAPTER 1

INTRODUCTION

1.1 Motivations

The field of spintronics is concerned with the efficient generation of spin currents and the control of magnetic elements. Conventionally, spin currents are generated by passing electrical currents through ferromagnetic metals (FM) [1-4]. The generated spin can interact with other FMs and transfer its spin angular momentum to the magnetization of FM. This phenomenon is called spin transfer torque (STT) [1, 2]. STT has been intensely studied because of its potential for applications in magnetic random access memories, programmable logics, and microwave oscillators [5, 6].

One of the major challenges for magnetic memories is that when the size of a magnetic element becomes smaller it is harder to switch the magnetization by magnetic fields, a conventional way of magnetization switching. Contrary to the field switching, STT relies on the spin polarizability of FM and electrical current density. Because the spin polarizability and electrical current density do not depend on the size of magnetic elements, STT is considered to be an ideal way to operate magnetic memories.

However, the electrical spin generation and electrical STT require a large electrical current density to switch magnetic elements. Especially when a magnetic element has a high thermal stability, the critical electrical current density for switching is ~10^{11} A m^{-2} [5, 6]. In addition, a

typical time scale for switching of nanomagnets by the electrical STT is order of a few nanoseconds [5]. For more efficient and faster control of magnetic elements, spin generation on a much shorter times scale is desirable.

Recently, much effort has been extended to generate spins by methods other than electrical currents. Particularly, regarding the interaction between ultrafast laser light and FM, there are three distinct mechanisms for the spin generation: (i) demagnetization; (ii) spin-dependent Seebeck effect (SDSE); and (iii) optical helicity. The first and second mechanisms can be classified in the thermal spin generation as energy of photons is the driving force. A theoretical study suggested that the thermal spin generation has a potential of a higher efficiency for spin generation than does the conventional electrical method [7]. The third mechanism should be classified in the non-thermal spin generation as angular momentum of photons is the driving force. For all three mechanisms, the underlying physics is still on debate, and STT has not been reported prior to studies described in this dissertation. Observation of STT is necessary to reveal the physics and to quantify the energy efficiency and time scale of these mechanisms.

1.2 Outline of dissertation

In this dissertation, I investigate the demagnetization-driven, SDSE-driven, and optical helicity-driven spin generation in metallic ferromagnets using ultrashort laser light. By measuring spin accumulation and STT on a sub-ps timescale, I reveal the underlying physics and quantify the energy efficiency and relevant time scale of each mechanism.

This dissertation is organized as follows.

In Chapter 2, I explain theoretical backgrounds for STT and literature reviews for the demagnetization-driven, SDSE-driven, and optical helicity-driven spin generation.

In Chapter 3, I describe experimental methods that I use. First, I explain the physical origin and experimental setup for time-resolved magneto-optical Kerr effect. Second, I describe interpretation and analysis of time-domain thermoreflectance. Parts of this chapter were published in "Indirect heating of Pt by short-pulse laser irradiation of Au in a nanoscale Pt/Au bilayer" Gyung-Min Choi, Richard B. Wilson, and David G. Cahill, Phys. Rev. B **89**, 064307 (2014).

In Chapter 4, I describe experimental results of the demagnetization-driven spin accumulation. I show that ultrafast demagnetization of FM creates a transient spin signal on the adjacent non-magnetic metals (NM) due to spin accumulation. Quantifying spin accumulation allows to determine spin-orbit coupling of conduction electrons of NM. Parts of this chapter were published in "Kerr rotation in Cu, Ag, and Au driven by spin accumulation and spin-orbit coupling" Gyung-Min Choi and David G. Cahill, Phys. Rev. B **90**, 214432 (2014).

In Chapter 5, I describe experimental results of the demagnetization-driven STT. I show that ultrafast demagnetization of the first FM trigger magnetization dynamics of the second FM, separated from the first FM by an NM, by STT. Quantifying STT allows to determine the spin relaxation time of the first FM. Parts of this chapter were published in "Spin current generated by thermally driven ultrafast demagnetization" Gyung-Min Choi, Byoung-Chul Min, Kyung-Jin Lee, and David G. Cahill, Nature Commun. **5**, 4334 (2014).

In Chapter 6, I describe experimental results of the SDSE-driven STT. I show that the spin-dependent Seebeck effect converts heat current to spin current and triggers magnetization dynamics by STT. Quantifying STT allows to determine the spin-dependent Seebeck coefficient

of FM. Parts of this chapter will be published in "Thermal spin transfer torque driven by spin-dependent Seebeck effect in metallic spin-valve structures" Gyung-Min Choi, Chul-Hyun Moon, Byoung-Chul Min, Kyung-Jin Lee, and David G. Cahill, Nature Phys. accepted.

In Chapter 7, I describe experimental results of the optical helicity-driven STT. I show that a direct transfer of angular momentum from light to FM is possible due to the spin-orbit splitting of the *d* band of FM. Parts of this chapter will be published in "Optical helicity-driven spin transfer torque in metallic ferromagnets" Gyung-Min Choi and David G. Cahill, in preparation.

In Chapter 8, in conclusion, I compare the energy efficiency of the demagnetization-driven, SDSE-driven, and optical helicity-driven STT.

In Appendix A, I describe experimental results of the spin accumulation driven by spin Seebeck effect (SSE). I show that there is spin signal in NM/ferrite structure driven by ultrafast heating of electrons of NM. However, the measurement does not agree with the SSE theory in terms of the magnitude and time response.

1.3 References

1. J. C. Slonczewski, J. Magn. Magn. Mater. **159**, L1 (1996).
2. L. Berger, Phys. Rev. B **54**, 9353 (1996).
3. M. Tsoi, A. G. M. Jansen, J. Bass, W.-C. Chiang, M. Seck, V. Tsoi, and P. Wyder, Phys. Rev. Lett. **80**, 4281 (1998).
4. J. A. Katine, F. J. Albert, R. A. Buhrman, E. B. Myers, and D. C. Ralph, Phys. Rev. Lett. **84**, 3149 (2000).
5. D. C. Ralph and M. D. Stiles, J. Magn. Magn. Mater. **320**, 1190 (2008).

6. A. Brataas, A. D. Kent, and H. Ohno, Nature Mater. **11**, 372 (2012).

7. J. C. Slonczewski, Phys. Rev. B **82**, 054403 (2010).

CHAPTER 2

THEORY AND LITERATURE REVIEW

2.1 Ferromagnetism

2.1.1 Origin of Ferromagnetism

Ferromagnetism arises when there is a local magnetic moment at each atom and a coupling between local magnetic moments. In isolated atoms, Hund's rules determine the spin configuration in atomic energy levels to minimize energy [1]: put electrons with spins in one direction into a partially filled atomic orbital before start adding spins in the other direction. The physical origin of the Hund's rule is the Pauli exclusion principle that keeps electrons with the same spin further apart thereby lower the Coulomb repulsion between them. In accordance with the Hund's rule, virtually all isolated atoms with partially filled orbital levels have non-zero spin moments.

The atomic magnetic moment is not a sufficient condition for a spontaneous magnetization. One more ingredient is the exchange interaction between neighboring atoms. According to the Heisenberg model [1], this interaction can be described by,

$$\hat{H} = -\sum_{\langle i,j \rangle} J_{ij} \hat{S}_i \cdot \hat{S}_j, \tag{2.1}$$

where J_{ij} is the exchange integral, S_i is the spin of the i_{th} atom, and S_j is the spin of the j_{th} atom. The physical origin of the J_{ij} is the same as that of the Hund's rule: an overlap between atomic orbitals splits the energy level depending on the spin alignment due to the Coulomb repulsion. If J_{ij} is positive, spins at neighboring positions favor a parallel alignment, which leads to

ferromagnetism. The ground state of the Heisenberg model is that all spins point in the same direction and the total magnetization is the sum of atomic magnetic moments.

2.1.2 Effect of Band Structure

When atoms are brought to a periodic lattice, electron states on neighboring atoms hybridize and form bands. Band formation acts to suppress magnetic moments in two ways. First, hybridization breaks spherical symmetry for the environment of each atom and quenches the orbital component of the magnetic moments. Second, hybridization produces overlap between bands and reduce spin polarization.

The 3*d*-transition metallic ferromagnets have partially filled *d*-bands at the Fermi level. These partially filled *d*-band produces a strong exchange splitting. The exchange splitting can stabilize a spin polarization even in the presence of band formation. For 3*d*-transition metallic ferromagnets, the magnetic moment per ion is 2.1, 1.7, and 0.6 μ_B for bcc Fe, hcp Co, and fcc Ni, respectively. There are two simplified models to describe the exchange splitting in the band structure: the free-electron Stoner model and the *s*-*d* model (Fig. 2.1). The former assumes that the electron bands for spin-up and spin-down electrons have a relative shift in energy due to an exchange interaction but otherwise they both have a free-electron dispersion, $E = \frac{\hbar^2 k^2}{2m} \pm \Delta$, where Δ is the exchange splitting. The latter distinguish the delocalized "*s*" electrons and the localized "*d*" electrons and assumes a weak interaction between "*s*" and "*d*" electrons. The simplified models can be useful for illustrating physical concepts, but they are far from realistic. A more realistic model is the local spin density approximation [2]. It treats the atomic-like exchange and correlation effect in mean field theory and treats the hybridization correctly.

2.1.3 Effect of Temperature

An increase in temperature favors randomization of the spin alignment and leads to a reduction of the total magnetization. The Heisenberg model describes the randomization of spin by spin reversal, and the spin reversal costs energy. Considering the nearest neighbor interaction, one spin reversal increases energy by $2zJ_{ij}$, where z is the number of the nearest neighbor. However, much lower energy can excite the spin reversal if all spins share the reversal, which is a spin wave. According to the spin wave theory [1], one spin reversal corresponds to the excitation of one magnon, and the magnon occupation follows the Bose-Einstein distribution. Then the magnetization reduction can be estimated by calculating the total number of magnons at a temperature T,

$$\sum_k n_k = \int d\omega \, D(\omega) \, \langle n(\omega) \rangle, \tag{2.2}$$

where $D(\omega)$ is the magnon density of states (DOS), $\langle n(\omega) \rangle$ is the Bose-Einstein distribution for magnons. The $D(\omega)$ can be obtained from the dispersion relation of magnon; at small wave vectors, the dispersion relation approximately is $\hbar\omega = 2\,J\,S\,a^2k^2$,

$$D(\omega) = \frac{1}{(2\pi)^3} 4\pi k^2 \frac{dk}{d\omega} = \frac{1}{4\pi^2} \left(\frac{\hbar}{2JSa^2}\right)^{3/2} \omega^{1/2}. \tag{2.3}$$

Then the total number of magnons is,

$$\sum_k n_k = \frac{1}{4\pi^2} \left(\frac{k_B T}{2JSa^2}\right)^{3/2} \int_0^\infty dx \frac{x^{1/2}}{e^x - 1}. \tag{2.4}$$

This result is the Bloch $T^{3/2}$ law that well explains magnetization vs. temperature at relatively low temperature compared to the Curie temperature (Fig. 2.2).

However, at high temperature, near the Curie temperature, the Bloch $T^{3/2}$ law fails indicating that magnon excitation is not a dominant mechanism for the spin reversal or the dispersion relation is not quadratic. Instead, the mean field theory is often used to explain spin reversal at high temperature [1]. The exchange interaction should depend on the position as the spin configuration is slightly different for each position. The mean field theory avoids this complexity and assumes that each atom experiences the same effective field, derived from the thermal equilibrium mean value of the exchange interaction of the nearest neighbor,

$$B_{eff} = \lambda M, \tag{2.5}$$

$$\lambda = \frac{2zJ}{Ng^2\mu_B^2}, \tag{2.6}$$

where z is the number of the nearest neighbor, g is the g-factor close to 2, and μ_B is the Bohr magneton. For S = ½ , the spontaneous magnetization is obtained by solving (Fig. 2.3),

$$M = N\mu_B \tanh\left(\frac{\mu_B \lambda M}{k_B T}\right). \tag{2.7}$$

At just below the Curie temperature, the mean field theory predicts $M \sim (T_C - T)^{1/2}$ regardless of the dimensionality. In real situation, $M \sim (T_C - T)^{1/8}$ for 2D from the Ising model and $M \sim (T_C - T)^{1/3}$ for 3D from experiments. Note, though, the agreement between the mean field theory and real situation gets better with the dimensionality and number of the nearest neighbor increase.

2.2 Interaction between spin current and magnetization

2.2.1 Electrical spin polarization

Electrons have a charge and a spin, but mostly charges and spins have been considered separately. In conventional electronics, charges are manipulated by electric fields but spins are ignored. In 1936, Mott first suggested the influence of spins on mobilities of electrons in ferromagnetic metals [3]: the conductivity of electron can then be expressed as the sum of two independent parts for two different spin projections (Fig. 2.4),

$$\sigma = \sigma_{\uparrow} + \sigma_{\downarrow}, \tag{2.8}$$

where $\sigma_{\uparrow}$ and $\sigma_{\downarrow}$ are conductivities of spin-up and spin-down channel, respectively. This is called the two-current model [3] and had been experimentally demonstrated by Campbell and Fert in 1968 [4].

Adapting the relaxation time approximation, the spin-dependent conductivity can be expressed by the Drude formula,

$$\sigma_{\uparrow,\downarrow} = \frac{e^2 n_{\uparrow,\downarrow} \tau_{\uparrow,\downarrow}}{m}, \tag{2.9}$$

where e is the electron charge, n is the conduction electron density, τ is the momentum relaxation time, and m is the electron mass. From the Fermi golden rule, the spin-dependent scattering rate is given by,

$$\frac{1}{\tau_{\uparrow,\downarrow}} = \frac{2\pi}{\hbar} \left| V_{\uparrow,\downarrow}^{sc} \right|^2 N_{\uparrow,\downarrow}(E_F), \tag{2.10}$$

where $V_{\uparrow,\downarrow}^{sc}$ is the spin-conserving potential and $N_{\uparrow,\downarrow}(E_F)$ is the DOS at the Fermi level. The spin dependence of scattering in the elementary 3*d*-transition metals Fe, Co and Ni can be understood from the spin-dependent DOS (Fig. 2.5).

The conductivity, which is determined predominantly by the contribution from the light *sp*-electrons, is decreased when *d*-states (to which scattering can take place) are present at the Fermi level. For Co and Ni, the majority spin *d*-band is fully occupied and is situated well below the Fermi level, whereas the minority spin 3*d*-band is only partially occupied. So when the scattering potential is spin-independent, the majority spin conductivity of Co and Ni is expected to be larger than the minority spin conductivity.

2.2.2 Spin transfer torque

When a spin-polarized electronic current enters a ferromagnet, there is a transfer of angular momentum between the propagating electrons and the magnetization of the ferromagnet. This concept of ‘‘spin transfer torque’’ was proposed independently by Slonczewski [5] and Berger [6] in 1996. Experimental confirmation came when the phenomenon of giant magnetoresistance was used to detect magnetization reversal in ferromagnetic multilayers with large current densities flowing perpendicular to the plane of the layers [7, 8].

The origin of the spin transfer torque is the absorption of transverse spin current at the interface between the non-magnetic and ferromagnetic layers. There are three distinct processes that contribute to the absorption [9] (Fig. 2.6): (i) spin filter effect at the interface; (ii) spin rotation at the interface; and (iii) spin precession in the ferromagnet. The spin filter effect occurs because the wave function for an incident electron with a spin component transverse to the magnetization spin can always be written as a linear combination of spin-up and spin-down components. Then, because the reflection and transmission amplitudes differ for up and down spins, the up and down spin contents of the reflected and transmitted wave functions differ both from each another and

from the incident state. This difference leads unavoidably to different transverse spin components and thus to a discontinuity in the transverse spin current.

The spin rotation arises because the spin of an electron rotates when it is reflected or transmitted at the interface between a non-magnet and a ferromagnet. The rotation is quantum mechanical result, and the amount of rotation differs considerably for electrons with wave vectors from different portions of the Fermi surface. Phase cancellation occurs after summing over all electrons. In the end, the transverse component of the reflected spin is negligible. The cancellation of the transmitted spin current is less dramatic than that of the reflected spin current.

The spin precession occurs due to exchange splitting of the ferromagnet. The electrons that transmit into the ferromagnet possess spin-up and spin-down components with the same total energy E_F, but different kinetic energy and so different wave vectors. This fact implies that each electron spin precesses (in space) as it propagates away from the interface. However, like the spin rotation angles, the spatial precession frequency varies considerably over the Fermi surface. Consequently, rapid dephasing of the transverse spin components of the individual electrons occurs as the conduction electron ensemble propagates into the ferromagnet. The net result is a precessing spin current that damps out algebraically within a few lattice constants of the interface (Fig. 2.7).

When summed over all Fermi surface electrons, these processes reduce the transverse component of the transmitted and reflected spin currents to nearly zero for most systems of interest. Therefore, to a good approximation, the torque on the magnetization is proportional to the transverse piece of the incoming spin current.

2.2.3 Magnetization dynamics

Magnetization dynamics is most easily investigated using the macrospin approximation. The macrospin approximation assumes that the magnetization of a sample stays spatially uniform throughout its motion and can be treated as a single macroscopic spin. Since the spatial variation of the magnetization is frozen out, calculating the dynamics of magnetic systems is much easier using the macrospin approximation than it is using full micromagnetic simulations. However, if there is a situation for a spatially non-uniform magnetization, the micromagnetic simulations is necessary.

When a magnetic configuration is away from equilibrium, the magnetization precesses around the instantaneous local effective field. In the absence of dissipation, the magnetization distribution stays on a constant energy surface. In order to account for energy loss, Landau and Lifshitz [10] introduced a phenomenological damping term into the equation of motion, and Gilbert [11] introduced a slightly different form several decades later,

$$\dot{\mathbf{m}} = -\gamma_e \mathbf{m} \times \mathbf{H}_{\text{eff}} + \alpha \mathbf{m} \times \dot{\mathbf{m}}, \tag{2.11}$$

where $\mathbf{m}$ is the unit vectors in the direction of the magnetization, $\dot{\mathbf{m}}$ is the time derivative of $\mathbf{m}$, $\mathbf{H}_{\text{eff}}$ is the effective field due to applied field, shape anisotropy, and crystalline anisotropy, γ_e $=1.76\times10^{11}$ rad s^{-1} T^{-1} is the electron gyromagnetic ratio, α is the Gilbert damping constant.

To calculate the effects of the spin transfer torque on magnetic dynamics, an additional spin transfer torque term is simply inserted in the Landau–Lifshitz–Gilbert equation. For the case of a symmetric two-magnetic-layer device with a metal spacer, Slonczewski [12] calculated the spin transfer torque using a simplified Boltzmann equation grafted with circuit theory. He found

that the torque on the free layer magnetization **m** due to the misalignment with fixed layer magnetization $\mathbf{m}_{\text{fixed}}$ can be described by,

$$\dot{\mathbf{m}} = -\gamma_e \mathbf{m} \times \mathbf{H}_{\text{eff}} + \alpha \mathbf{m} \times \dot{\mathbf{m}} + \frac{J_S}{M_S h} \mathbf{m} \times (\mathbf{m} \times \mathbf{m}_{\text{fixed}}), \quad (2.12)$$

where $\mathbf{m}_{\text{fiexd}}$ are unit vectors in the direction of the fixed magnetization, in which the spin current is produced, M_S and h are respectively the saturation magnetization and thickness of the free magnetization, where the spin current produces spin transfer torque, and J_S is the transverse spin current that is absorbed by the free magnetization. When the direction of spin transfer torque is opposite to that of damping, STT can move magnetization away from its equilibrium position (Fig. 2.8).

When the spin current generates larger STT than damping and persists for long enough time, a multiple of several times of magnetization precession period, it can eventually lead to magnetization switching (Fig. 2.9). With the magnetic element that has a high thermal stability factor over $\Delta E/k_B T = 60$, where ΔE is the energy barrier due to magnetic anisotropy, the typical electrical current density for switching is ~10^{11} A m^{-2} [13]. This large current density is difficult to achieve with a small sized transistor and limits its application in device operations.

2.3 Demagnetization-driven spin generation

Ultrafast demagnetization by an ultrashort laser pulse has been investigated extensively in recent years [14-18]. After sub-100 femtosecond laser excitation, a characteristic demagnetization timescale is a few hundreds of femtoseconds. However, the mechanism for dissipation of magnetization on such a short time is still under debate. Recently, several theoretical and experimental works claim that ultrafast demagnetization can generate spin currents by spin-

dependent transport of hot electrons [19-22]. However, this explanation contradicts the phenomenological thermodynamic description of demagnetization.

2.3.1 Three temperature model

Phenomenologically, ultrafast demagnetization has been described by the so-called three-temperature (3TM) model [14]. The 3TM model assumes the electronic, magnon, and phonon systems are internally in thermal equilibrium so that each system can be characterized by its own temperature (T_e, T_m, and T_p) and heat capacity (C_e, C_m, and C_p) (Fig. 2.10). Given the initial condition, the temperature evolution of each system is described by a set of three coupled differential equations,

$$C_e \frac{dT_e}{dt} = -g_{ep}(T_e - T_p) - g_{em}(T_e - T_m), \tag{2.13}$$

$$C_p \frac{dT_p}{dt} = -g_{ep}(T_p - T_e) - g_{mp}(T_p - T_m), \tag{2.14}$$

$$C_m \frac{dT_m}{dt} = -g_{em}(T_m - T_e) - g_{mp}(T_m - T_p), \tag{2.15}$$

where g_{ep} is the electron-phonon coupling, g_{em} is the electron-magnon coupling, g_{mp} is the magnon-phonon coupling, and they define the rate of energy transfer between systems. In laser-heating experiments, absorption of photons leads mostly to electronic excitations, causing a quasi-instantaneous increase of the electron temperature. The overshoot of the magnon temperature can be explained by assuming g_{em} is much larger than g_{mp}.

2.3.2 Microscopic three temperature model

The 3TM model considers energy conservation, but does not explain the dissipation channel for angular momentum. Koopmans *et al*. incorporated the spin relaxation mechanism into the 3TM [18] (Fig. 2.11): spin relaxation is mediated by Elliott-Yafet-like processes [23, 24], with a spin-flip probability a_{sf} for electron-phonon momentum scattering events. According to this model, so-called microscopic 3TM (M3TM) [18], whereas it is the excess energy in the electron system that provides the energy for the demagnetization, the electron-phonon mediated spin-flip scattering provides a dissipative channel for angular momentum. Although M3TM explains both energy transport and dissipation of angular momentum, it does not predict that demagnetization can produce spin currents.

2.3.3 Superdiffusive model

For another theory for demagnetization, Battiato *et al.* proposed that spin-dependent relaxation and fast transport of hot electrons play a crucial role [19] and suggested that ultrafast demagnetization is due to the spin-polarized hot electrons which move to an adjacent metallic layer by a so-called "superdiffusive current" (Fig. 2.12). This model is sharp contrast to 3TM or M3TM as it explains demagnetization in terms of the motion of the hot electrons, not by coupling among electrons, magnons, and phonons. Nonetheless, this model is the first attempt to predict the demagnetization-driven spin current.

The findings of several subsequent experiments have been interpreted as supporting this hypothesis [20-22]. However, most results are based on analysis of demagnetization not spin current, and the transport of thermal energy is not considered in these experiments [20-22]. Recently I have shown that the exchange of thermal energy between metal layers is crucial in the

interpretation of demagnetization of a ferromagnet in a metallic multilayer structure [25]. Therefore, I argue that a comprehensive analysis of the exchange of thermal energy in the system and the implementation of a direct method for detecting demagnetization-induced spin currents are needed.

2.4 Heat current-driven spin generation

Recently, much effort has been extended to understand the generation of spin currents by thermal gradients. This effort has spawned the field of spin caloritronics, which is concerned with non-equilibrium phenomena related to spin, charge, entropy and energy transport in magnetic structures and devices. There are two pronounced mechanisms for thermal spin generation: spin-dependent Seebeck effect and spin Seebeck effect. Although they are similar in nomenclature, the underlying mechanism for them are entirely different.

2.4.1 Spin-dependent Seebeck effect (SDSE)

SDSE applies to metallic ferromagnets where spin-dependent DOS results in spin-dependent Seebeck coefficient. As charge currents can generate spin currents by spin-dependent conductivities, heat currents can generate spin currents by spin-dependent Seebeck coefficient. Adapting the two-current model and Sommerfeld expansion [1],

$$\begin{pmatrix} J_C \\ J_S \\ J_Q \end{pmatrix} = \sigma \begin{pmatrix} 1 & P & ST \\ P & 1 & P'ST \\ ST & P'ST & \Lambda T/\sigma \end{pmatrix} \begin{pmatrix} \nabla\mu_C/e \\ \nabla\mu_S/e \\ -\nabla T/T \end{pmatrix}, \tag{2.16}$$

where J_C is the charge current, J_S is the spin current, J_Q is the heat current, $\nabla\mu_C$ is the gradient of electric chemical potential, $\nabla\mu_S/e$ is the gradient of spin chemical potential, ∇T is the gradient of temperature, S is the Seebeck coefficient, T is the temperature, Λ is the thermal conductivity, σ is the electrical conductivity, and P and P' stand for the spin-polarization of the conductivity and its energy derivative,

$$P = \frac{\sigma_\uparrow - \sigma_\downarrow}{\sigma}\Big|_{E_F};\ P' = \frac{\partial(P\sigma)}{\partial E}\Big|_{E_F}. \tag{2.17}$$

According to this, not only an applied voltage but also a temperature gradient drives a spin current in a conducting ferromagnet. Because the individual Seebeck coefficients for the two spin channels, $S_{\uparrow,\downarrow}$, are not equal, a spin current flows through ferromagnet by the temperature gradient even in the absence of a charge current, creating a spin accumulation at the interface between ferromagnet and non-magnet, which relaxes in the ferromagnet and non-magnet on the length scale of their respective spin relaxation lengths.

Slachter *et al.* reported the SDSE-driven spin generation with the NiFe/Cu structure [26] (Fig. 2.13). While creating a steady-state heat current through NiFe by the Joule heating, they electrically measured spin accumulation in Cu in a non-local geometry. Spins are generated at the NiFe/Cu interface by SDSE and accumulate on Cu with the spin relaxation length of Cu.

2.4.2 Spin Seebeck effect (SSE)

SSE mostly applies to the insulating ferrite/NM structure and relies on hypothetic coupling between magnons of ferrite and electrons of NM. Slonczewski theoretically explained this coupling by assuming the presence of a monolayer of paramagnet at the ferrite/NM interface [27]

(Fig. 2.14). Then the magnetic moment of the ferrite can interact with magnetic moment of the paramagnet by the super-exchange interaction, and the magnetic moment of the paramagnet can interact with the spin moment of the conduction electrons of NM by the *s*-*d* exchange. Since both super-exchange and *s*-*d* exchange conserve angular momentum, angular momentum of magnons of ferrite can be transferred to electrons of NM. When a metallic FM is attached to the other side of NM, spin currents flow from ferrite, through NM, and into FM, thus resulting in STT on FM.

Slonczewski pointed out that this way of thermal spin generation from magnons of ferrite can be much more efficient in terms of energy than the electrical spin generation [27]. The quantum yield for STT can be defined by,

$$\varepsilon = \frac{\text{transferred spin momemtum}/\hbar}{\text{spent electric charge}/e}. \tag{2.18}$$

For the electrical spin generation, ε cannot exceed ½ because one electron can only carry spin momentum ½ $\hbar$. On the contrary, if an electron that passes through ferrite with a voltage of 1 V uses its energy, 1 eV, to excite magnons, whose energy is around $k_B T$, ε could be $\frac{eV}{k_B T} \approx 40$. Although this estimation is based on unjustified assumptions (assuming a strong coupling between magnons of ferrite and electrons of NM and neglecting phonon effect on energy transport), it gives an useful insight about the advantage of thermal spin generation over electrical spin generation.

Another theory for the spin Seebeck effect is based on the spin pumping theory [28, 29]. According the spin pumping theory, when the ferromagnet is thermally excited, it pumps a spin current into the normal metal,

$$J_S^{pump}(t) = \frac{\hbar g_r}{4\pi}\mathbf{m}(t) \times \frac{d\mathbf{m}(t)}{dt}, \tag{2.19}$$

where g_r is the real part of the spin mixing conductance of the FM/NM interface and **m**(t) is the unit vector of the time-dependent magnetization of FM. On the other hand, at finite temperature the NM generates thermal noise in the form of current fluctuations that are partially spin-polarized. At thermal equilibrium, the sum of the time-averaged currents vanishes. When the effective temperature between FM and NM are different, combining the spin pumping theory and fluctuation-dissipation theorem, there would be a net spin current [29],

$$I_S = \frac{\hbar\gamma}{2\pi}\frac{g_r k_B}{M_S V_{coh}}(T_F - T_N), \tag{2.20}$$

where γ is the gyromagnetic ratio, M_S is the saturation magnetization of FM, V_{coh} is the magnetic coherence volume of FM. Recently, Uchida *et al.* have claimed the observation of the spin Seebeck effect in the Pt/ferrite structure [30, 31]. They measured a transverse voltage in Pt applying a temperature gradient between Pt and ferrite. It has interpreted that the temperature gradient creates spin current at Pt by spin Seebeck effect, then this spin current converts to voltage signal by the inverse spin Hall effect [30, 31] (Fig. 2.15).

2.5 Optical helicity-driven spin generation

Optical spin generation is a quantum mechanical phenomena and is determined by the selection rule for the dipolar transition. Optical spin generation is mostly investigated with semiconductor because its band structure allows a high degree of spin polarization in photo-carries [32]. Inversely, spin-polarized carriers in semiconductor can emit circularly polarized light by radiative recombination, and this process permits a simple way to quantify spin polarization of carriers. For 3*d* transition ferromagnets, circularly polarized x-ray has been used to detect the spin-dependent DOS of the 3*d* band, which is called x-ray magnetic circular dichroism (XMCD) [33].

Due to the characteristic energy of the x-ray, it induces the dipolar transition from the core states to the valence 3*d* state. The high degree of localization and strong spin-orbit splitting of the core states allows spin polarization in the 3*d* band.

2.5.1 Optical spin generation in semiconductor

GaAs is an ideal choice for optical spin generation because its direct bandgap allows the generation of a high density of photo-carriers [32]. The valence band of it splits into four-fold degenerate $p_{3/2}$ state, which consists of two-fold degenerate heavy-hole and light-hole subbands, and two-fold $p_{1/2}$ state lying ΔE = 0.34 eV below the $p_{3/2}$ state. The conduction band is two-fold degenerate $s_{1/2}$ state lying ΔE = 1.42 eV above the $p_{3/2}$ state. According to the dipolar selection rule, two transition processes from the $p_{3/2}$ to $s_{1/2}$ are allowed. With a left circularly polarized light, the transition from the heavy/light hole subband of the $p_{3/2}$ leads to the spin up/down in the $s_{1/2}$ state, and the transition probability from the light hole subband is a factor of three larger than those from the heavy-hole subbands. Therefore, the maximum spin polarization is 50 % for GaAs [34] (Fig. 2.16). Even 100 % is possible with the quantum well structure, where the heavy and light hole subbands are separated in energy by quantum confinement [35].

2.5.2 X-ray Magnetic Circular Dichroism (XMCD)

X-ray induces interband transition in transition metals from the *s* or *p* core states to the valence states. Since the core states are highly localized with defined quantum number, the transition can scan the density of final states according to the dipolar selection rule [33]. The measurements can be carried out with different core states (*K*, $L_{2,3}$, or $M_{4,5}$ edges) selecting the

character of the final states (*p*, *d*, or *f* states). Using circularly polarized x-ray, spin-dependent density of the final states can be measured. This simple explanation for XMCD is given by the two-step model [36] (Fig. 2.17). The first step consists of the excitation of a photoelectron that is effectively spin-polarized due to the dipolar selection rule. The spin-polarization is derived for the various absorption edges from atomic considerations [36]. In a second step, the photoelectrons settle according to the available density of final states that in turn is spin-dependent. This model implies that XMCD spectra, i.e. the difference in the absorption cross section for left and right circularly polarized light, directly reflects the spin-polarization of the final states, namely the difference in the DOS for spin up and down electrons.

The absorption cross section can be evaluated from the matrix element of the relevant transition [33] (Fig. 2.18). For the $L_{2,3}$ edge XMCD, the relevant transition is from 2*p* to 3*d* states, and the angular part mostly determines the matrix element. The calculation of the matrix elements with a left circular polarized light shows that $2p_{3/2}$ and $2p_{1/2}$ states prefer spin-up and spin-down polarization, respectively.

2.6 References

1. N. W. Ashcroft and N. D. Mermin, *Solid State Physics* (Cengage Learning, 1976), C. Kittel, *Introduction to Solid State Physics* (Wiley, 1995).
2. R. O. Jones and O. Gunnarsson, Rev. Mod. Phys. **61**, 689 (1989).
3. F. Mott, Proc. R. Soc. London, Ser. A **153**, 699 (1936).
4. A. Fert and I. A. Campbell, Phys. Rev. Lett. **21**, 1190 (1968).
5. J. C. Slonczewski, J. Magn. Magn. Mater. **159**, L1 (1996).

6. L. Berger, Phys. Rev. B **54**, 9353 (1996).
7. E. B. Myers, D. C. Ralph, J. A. Katine, R. N. Louie, and R. A. Buhrman, Science **285**, 867 (1999).
8. J. A. Katine, F. J. Albert, R. A. Buhrman, E. B. Myers, and D. C. Ralph, Phys. Rev. Lett. **84**, 3149 (2000).
9. M. D. Stiles and A. Zangwill, Phys. Rev. B **66**, 014407 (2002).
10. L. Landau, and E. Lifshitz, Phys. Z. Sowietunion, **8**, 153 (1935).
11. T. L. Gilbert, IEEE Trans. Magn. **40**, 3443 (2004).
12. J. C. Slonczewski, J. Magn. Magn. Mater. **247**, 324 (2002).
13. D. C. Ralph and M. D. Stiles, J. Magn. Magn. Mater. **320**, 1190 (2008).
14. E. Beaurepaire, J.-C. Merle, A. Daunois, and J.-Y. Bigot, Phys. Rev. Lett. **76**, 4250 (1996).
15. B. Koopmans, J. J. M. Ruigrok, F. D. Longa, and W. J. M. de Jonge, Phys. Rev. Lett. **95**, 267207 (2005).
16. C. Stamm, T. Kachel, N. Pontius, R. Mitzner, T. Quast, K. Holldack, S. Khan, C. Lupulescu, E. F. Aziz, M. Wietstruk, H. A. Dürr, and W. Eberhardt, Nature Mater. **6**, 740 (2007).
17. C. Boeglin, E. Beaurepaire, V. Halté, V. López-Flores, C. Stamm, N. Pontius, H. A. Dürr, and J.-Y. Bigot, Nature **465**, 458 (2010).
18. B. Koopmans, G. Malinowski, F. Dalla Longa, D. Steiauf, M. Fähnle, T. Roth, M. Cinchetti, and M. Aeschlimann, Nature Mater. **9**, 259 (2010).
19. M. Battiato, K. Carva, and P. M. Oppeneer, Phys. Rev. Lett. **105**, 027203 (2010).
20. G. Malinowski, F. Dalla Longa, J. H. H. Rietjens, P. V. Paluskar, R. Huijink, H. J. M. Swagten, and B. Koopmans, Nature Phys. **4**, 855 (2008).

21. A. Melnikov, I. Razdolski, T. O. Wehling, E. Th. Papaioannou, V. Roddatis, P. Fumagalli, O. Aktsipetrov, A. I. Lichtenstein, and U. Bovensienpen, Phys. Rev. Lett. **107**, 076601 (2011).
22. D. Rudolf, C. La-O-Vorakiat, M. Battiato, R. Adam, J. M. Shaw, E. Turgut, P. Maldonado, S. Mathias, P. Grychtol, H. T. Nembach, T. J. Silva, M. Aeschlimann, H. C. Kapteyn, M. M. Murnane, C. M. Schneider, and P. M. Oppeneer, Nature Commun. **3**, 1037 (2012).
23. R. J. Elliot, Phys. Rev. **96**, 266 (1954).
24. Y. Yafet, *Solid State Physics* Vol. 14 (Academic, 1963).
25. G.-M. Choi, R. B. Wilson, and D. G. Cahill, Phys. Rev. B **89**, 064307 (2014).
26. A. Slachter, F. L. Bakker, J-P. Adam, ad B. J. van Wees, Nature Phys. **6**, 879 (2010).
27. J. C. Slonczewski, Phys. Rev. B **82**, 054403 (2010).
28. Y. Tserkovnyak, A. Brataas, and G. E. W. Bauer, Phys. Rev. Lett. **88**, 117601 (2002).
29. J. Xiao, G. E. W. Bauser, K. Uchida, E. Saitoh, and S. Maekawa, Phys. Rev. B **81** 214418 (2010).
30. K. Uchida, J. Xiao, H. Adachi, J. Ohe, S. Takahashi, J. Ieda, T. Ota, Y. Kajiwara, H. Umezawa, H. Kawai, G. E. W. Bauer, S. Maekawa, and E. Saitoh, Nature Mater. **9**, 898 (2010).
31. K. Uchida, T. Nonaka, T. Ota, and E. Saitoh, Appl. Phys. Lett. **97**, 172505 (2010).
32. F. Meier and B. P. Zakharchnya, *Optical Orientation* (North-Holland, 1984).
33. H. Ebert, Rep. Prog. Phys. **59**, 1665 (1996).
34. T. Taniyama, E. Wada, M. Itoh, and M. Yamaguchi, NPG Asia Mater. **3**, 65 (2011).
35. B. T. Jonker, Proc. IEEE, **91**, 727 (2003).

36. G. Schütz, W. Wagner, W. Wilhelm, P. Kienle, R. Zeller, R. Frahm, and G. Materlik, Phys. Rev. Lett. **58**, 737 (1987).

37. W. Kipferl, M. Dumm, P. Kotissek, F. Steinbauer, and G. Bayreuther, J. Appl. Phys. **95**, 7417 (2004).

38. A. Fert, Rev. Mod. Phys. **80**, 1517 (2008).

39. J. Mathon and A. Umerski, *Physics of Low Dimensional System* (Kluwer/Plenum, 2001).

40. B. Koopmans, *Handbook of Magnetism and advanced magnetic materials*, Vol. 3 (Wiley, 2007).

2.7 Figures

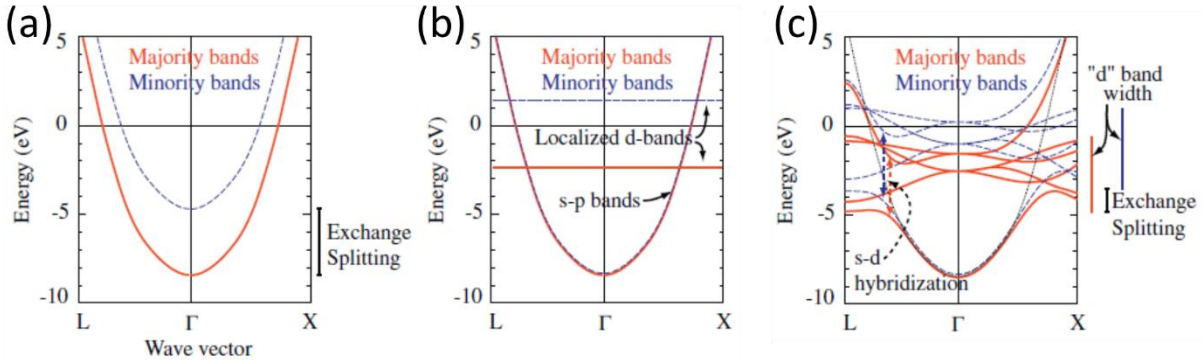

Fig. 2.1: Model band structures for ferromagnets. (a) A schematic band structure by the Stoner model. Free electron-like spin-up and spin-down bands are shifted by exchange splitting. (b) A schematic band structure by the *s-d* model. The current-carrying *s-p* bands have a very small splitting due to the weak exchange interaction with the localized *d*-states. (c) Bands calculation by the local spin density approximation for fcc Co. The bars to the right show the width of the *d* bands and the shift between the spin-up and spin-down bands. The dashed arrows indicate the widths of avoided level-crossings due to the hybridization between the *s-p* and *d* bands of the same symmetry. All plots are reproduced from Ref. 13.

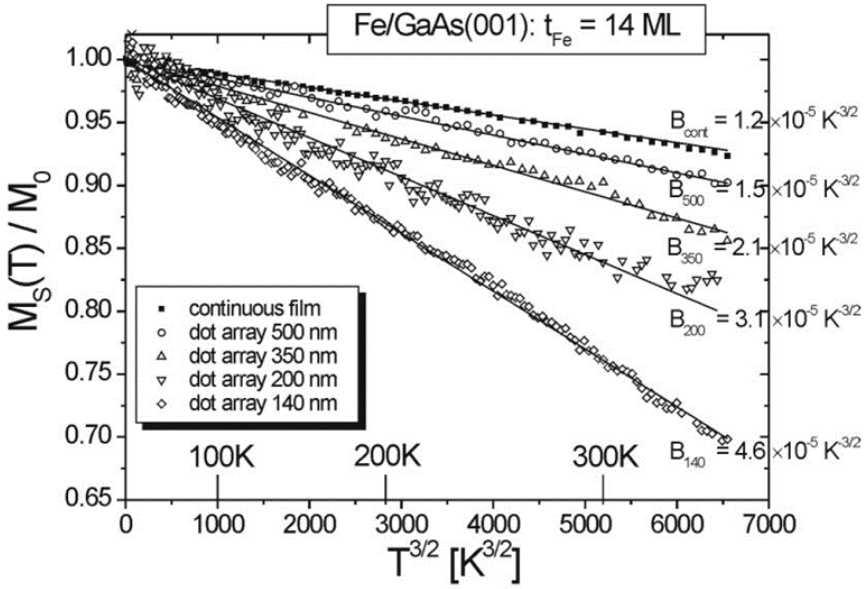

Fig. 2.2: Comparison of the temperature dependence of the spontaneous magnetization for dot arrays with dot diameters of 140–500 nm and a continuous film of the Fe (14 ML)/ GaAs (001) substrate. All plots are reproduced from Ref. 37.

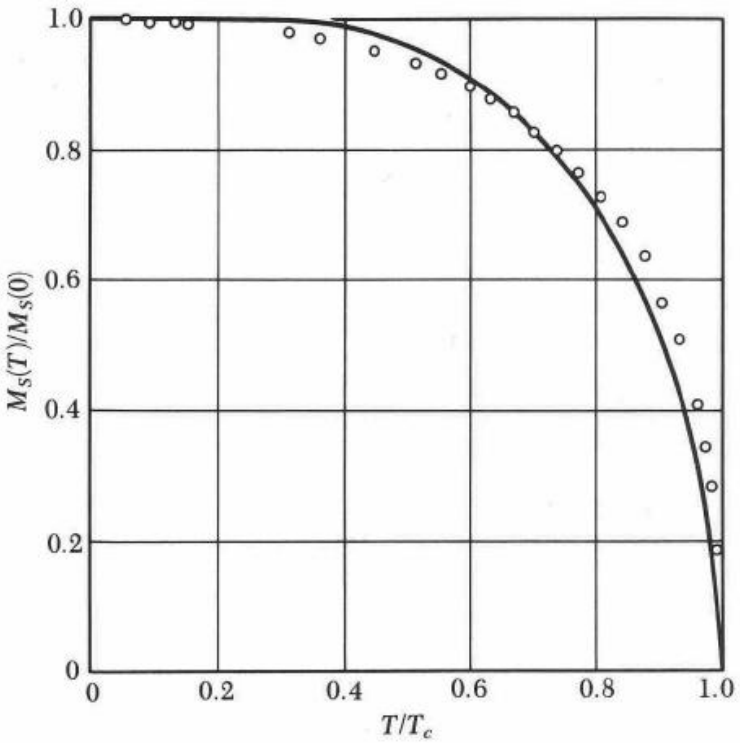

Fig. 2.3: Saturation magnetization of nickel as a function of temperature (black circles) and theoretical prediction of the mean field theory (solid line). All plots are reproduced from Ref. 1.

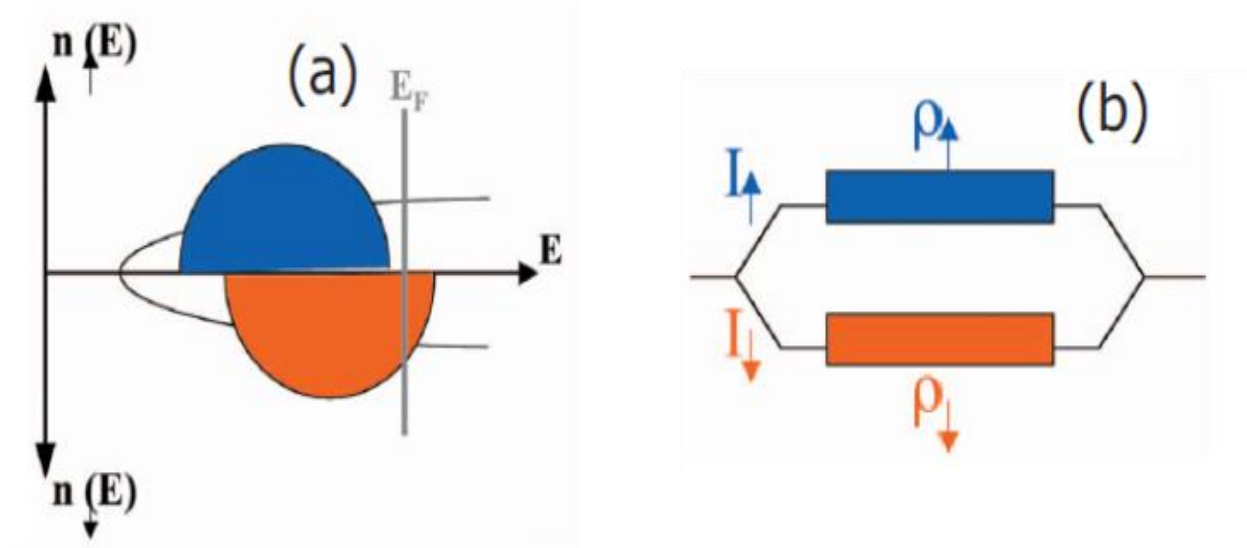

Fig. 2.4: Schematic representation of the two-current model. (a) A simplified representation of spin-dependent DOS of ferromagnet, and (b) a resultant two current channels with different conductivity. All plots are reproduced from Ref. 38.

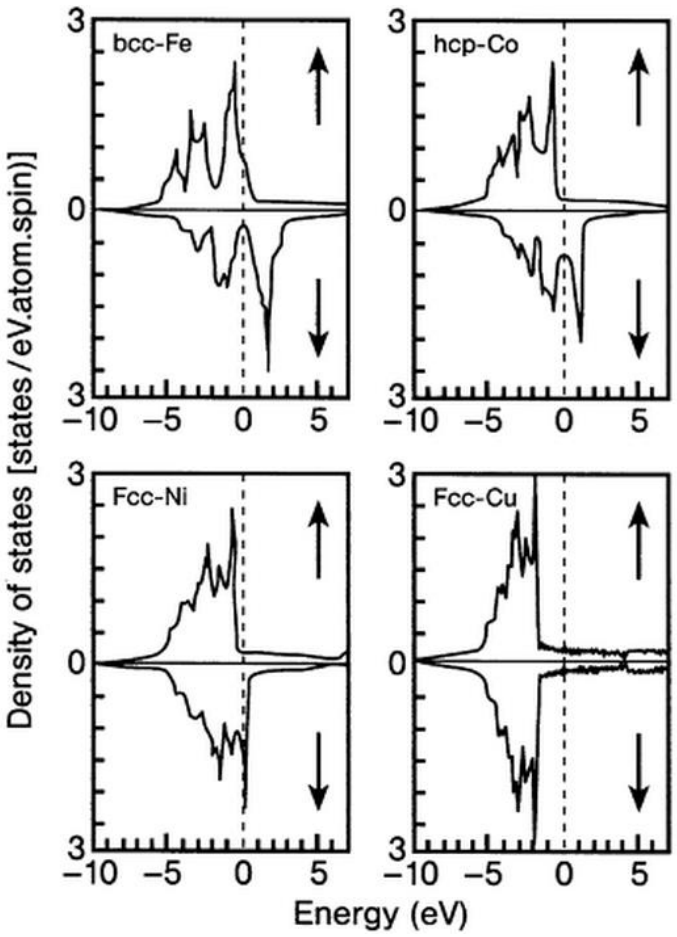

Fig. 2.5: Spin-dependent DOS of fcc Fe, hcp Co, fcc Ni, and fcc Cu, obtained from Local Spin Density Approximation. All plots are reproduced from Ref. 39.

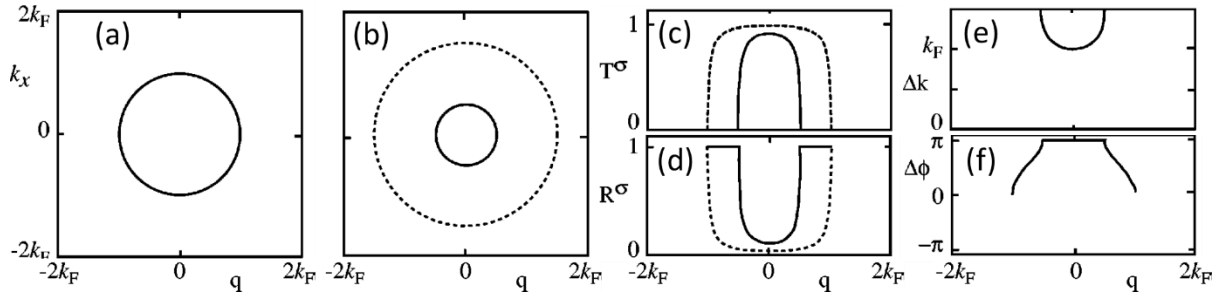

Fig. 2.6: The Fermi surface for the (a) non-magnet and (b) ferromagnet. The probability for (c) transmission into the ferromagnet and (d) for reflection back into the non-magnet for majority (dashed lines) and minority (solid lines) electrons. (e) The wave vector difference for the transmitted electrons. (f) The phase distribution of the reflected electrons. All plots are reproduced from Ref. 9.

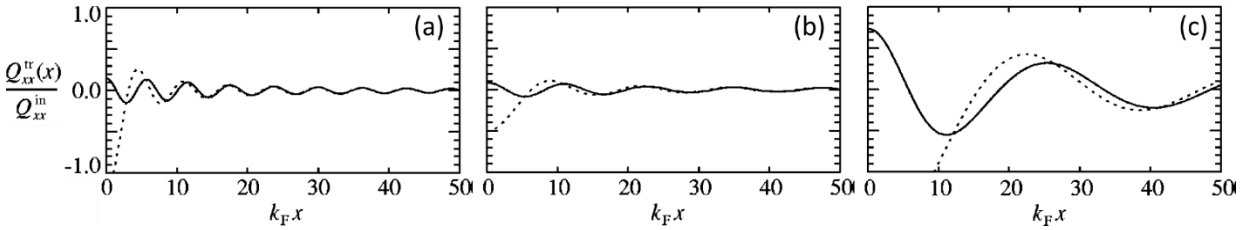

Fig. 2.7: Decay of transverse transmitted spin currents as a function of distance from the interface with different mismatch between the sizes of the Fermi surfaces of non-magnet and ferromagnet: (a) $\frac{k_{F\uparrow}}{k_F} = 1.5$ and $\frac{k_{F\downarrow}}{k_F} = 0.5$; (b) $\frac{k_{F\uparrow}}{k_F} = 1.0$ and $\frac{k_{F\downarrow}}{k_F} = 0.5$; (c) $\frac{k_{F\uparrow}}{k_F} = 1.1$ and $\frac{k_{F\downarrow}}{k_F} = 0.9$. All plots are reproduced from Ref. 9.

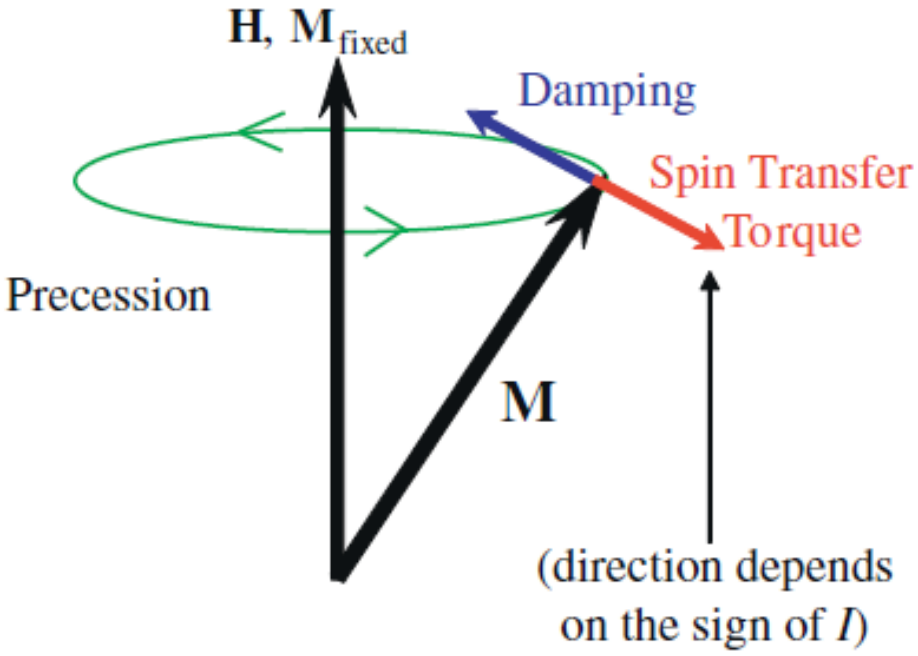

Fig. 2.8: Schematic representation of the effect of STT on the magnetization dynamics, reproduced from Ref. 13.

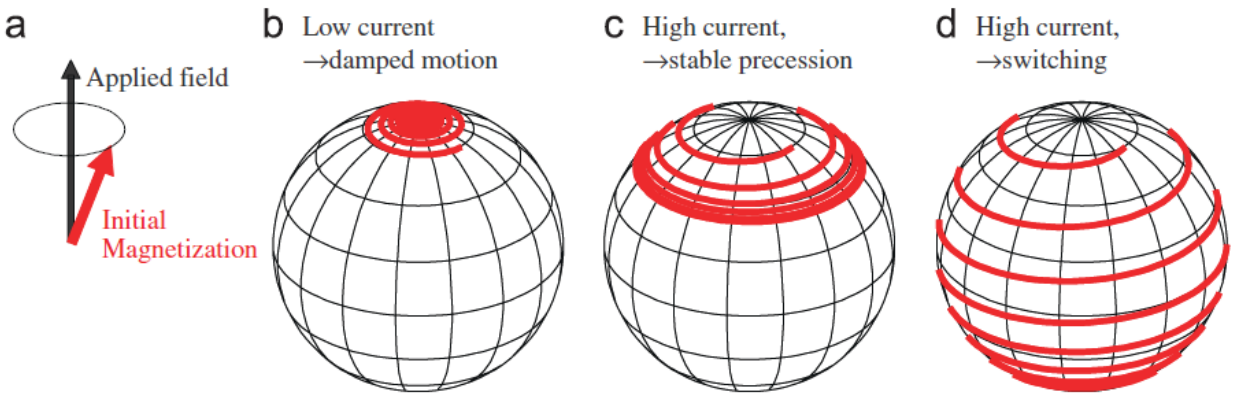

Fig. 2.9: Trajectories of STT-driven magnetization dynamics. With the initial configuration of (a), the magnetization dynamics can be (a) a damped motion, (b) stable precession, and (c) switching depending on the amount of spin current. All plots are reproduced from Ref. 13.

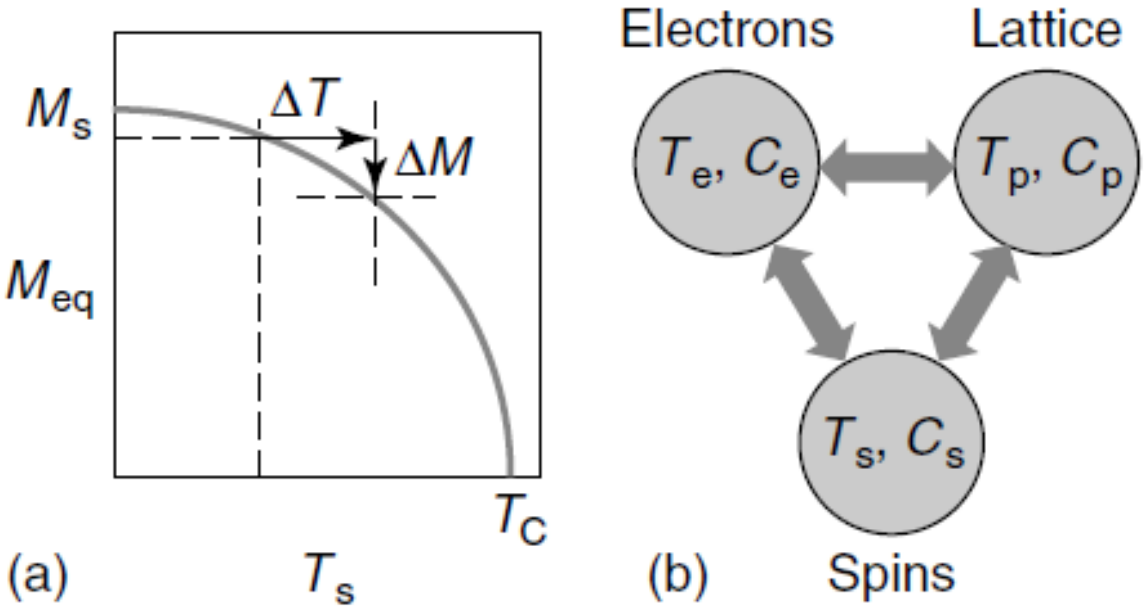

Fig. 2.10: (a) Definition of the spin temperature. Increase of the spin temperature leads to decrease of magnetization. (b) Schematic representation of the three temperature model. All plots are reproduced from Ref. 40.

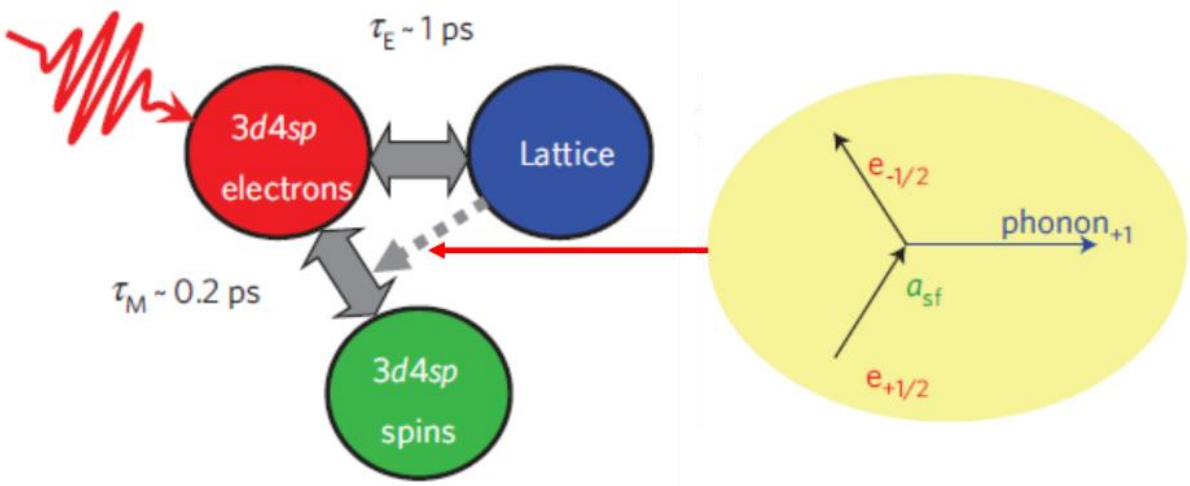

Fig. 2.11: Schematic representation of the M3TM. Two-sided arrows indicate the energy transport between systems and the dashed arrow shows the dissipation channel for angular momentum by the Elliott-Yafet spin-flip scattering on emission of a phonon. All plots are reproduced from Ref. 18.

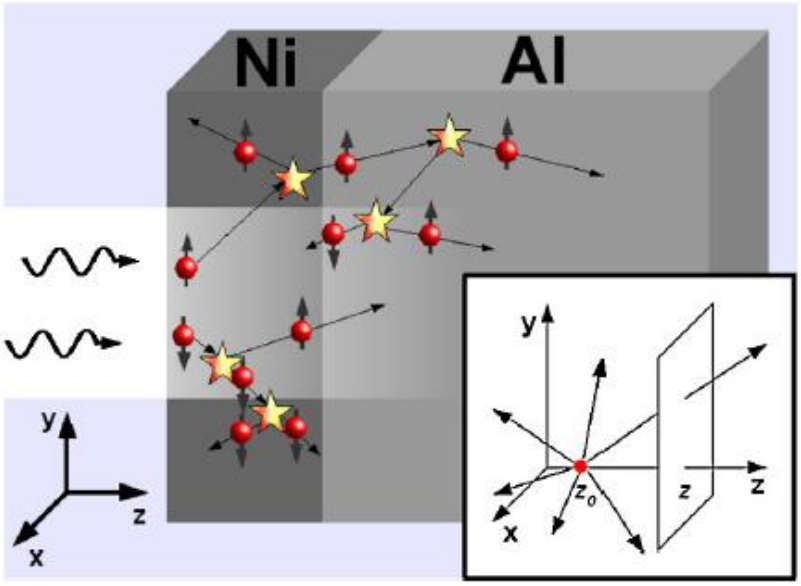

Fig. 2.12: Schematics of the superdiffusive model. Different mean free paths for majority and minority spin carriers are shown and also the generation of a cascade of electrons after an inelastic scattering. All plots are reproduced from Ref. 19.

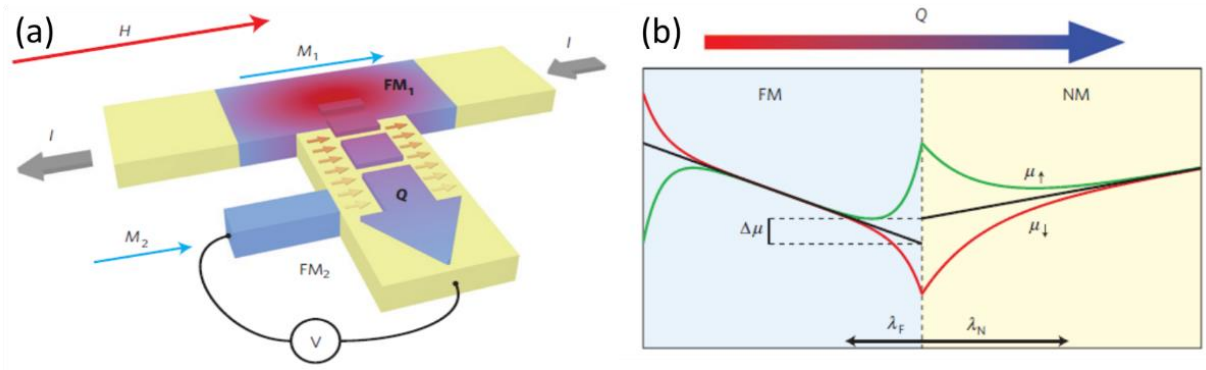

Fig. 2.13: Non-local detection of thermally injected spin accumulation by SDSE. (a) Schematics of measurements. (b) Schematics of spin accumulation at the ferromagnet/non-magnet interface. All plots are reproduced from Ref. 26.

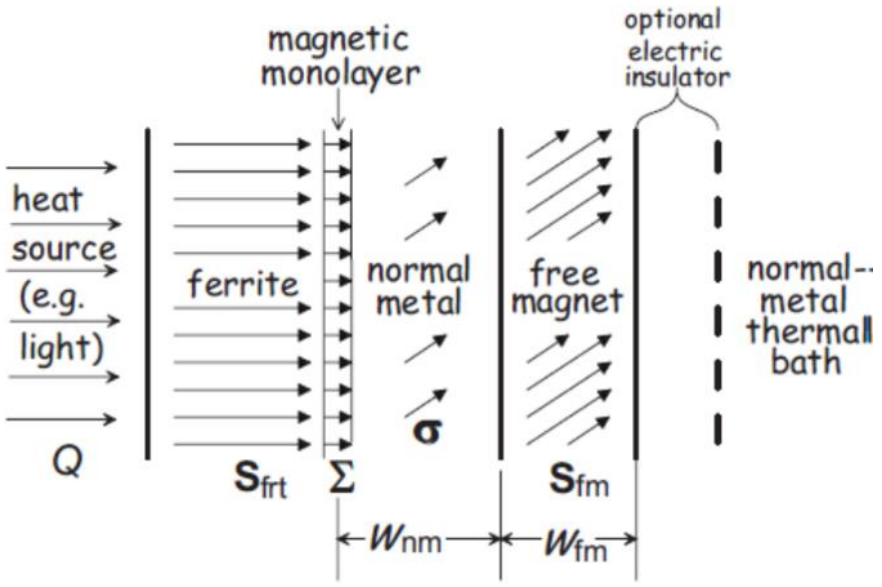

Fig. 2.14: Schematic arrangement of the elements required for creating STT on FM by thermally initiating spin current from magnons of ferrite. All plots are reproduced from Ref. 27.

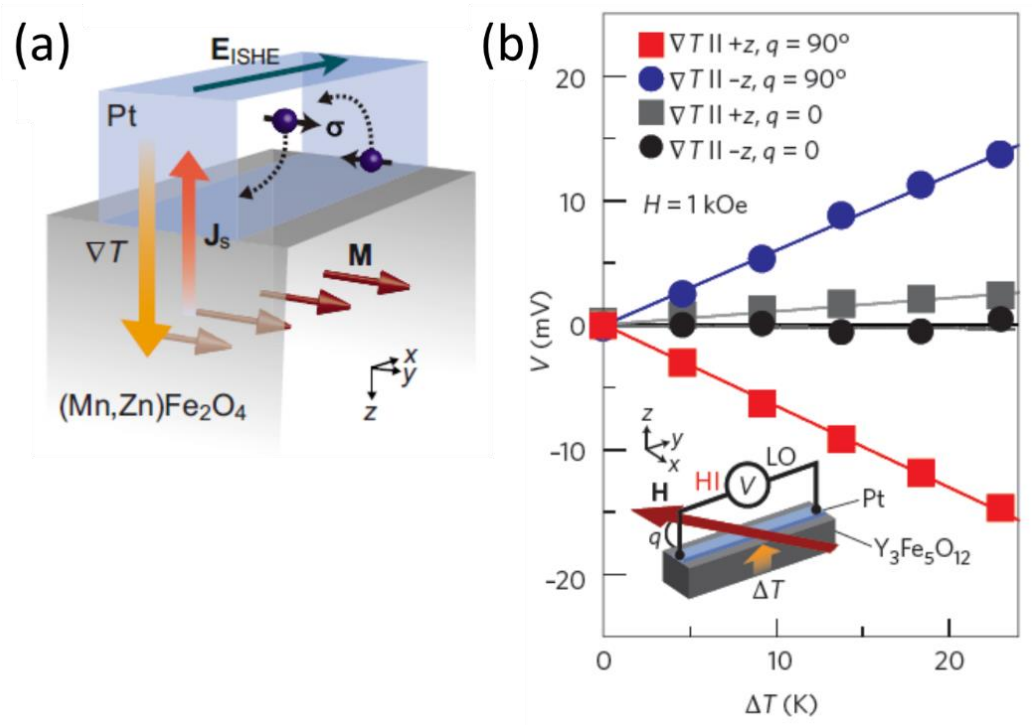

Fig. 2.15: (a) Schematic illustration of the longitudinal spin Seebeck effect with a ferrimagnetic oxide ((Mn.Zn)Fe_2O_4)and non-magnetic metal (Pt). (b) ΔT dependence of voltage between the end of the Pt at applied magnetic field of 0.1 T (=1 kOe). ΔT is the temperature difference between heat baths connected to Pt and (Mn, Zn)Fe_2O_4 side. All plots are reproduced from Ref. 31.

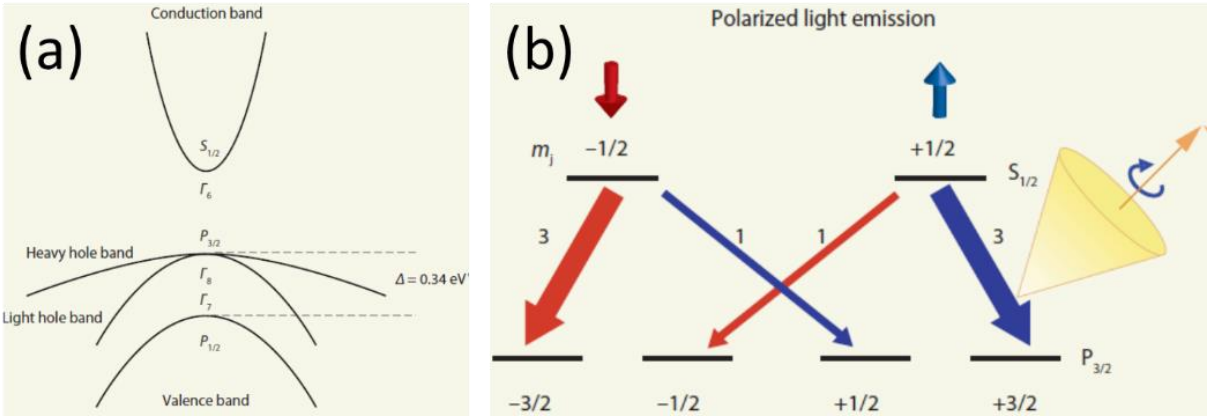

Fig. 2.16: (a) Band diagram for GaAs. (b) Radiative recombination of spin-up and spin-down electrons according to the dipolar selection rule. Optical spin generation is inverse of (b). All plots are reproduced from Ref. 34.

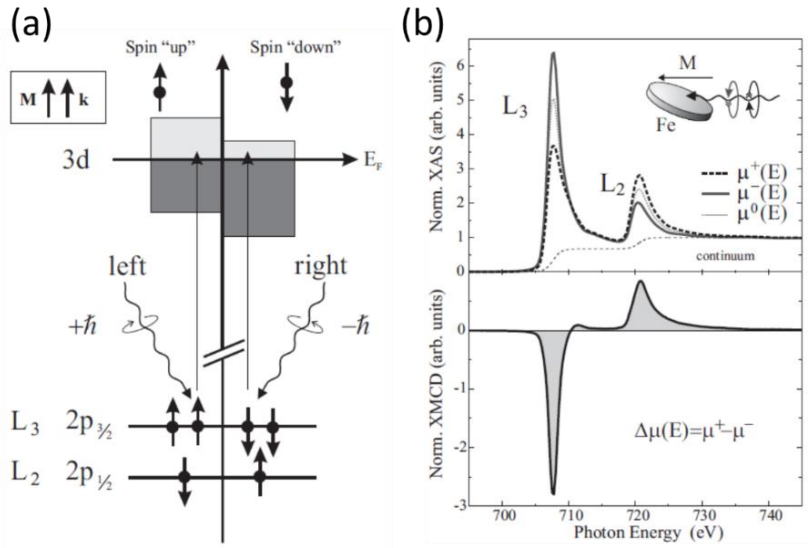

Fig. 2.17: (a) Schematic representation of XMCD at the $L_{2,3}$ edge. In the first step, the circular polarized x-ray creates spin-polarized electrons. In the second step, the spin-dependent d band acts as a spin detector. The top panel of (b) is the helicity dependent absorption spectra with left (solid line) and right (dashed line) circular polarization. The bottom panel of (b) is the different of absorption spectra between left and right circular polarization. All plots are reproduced from Ref. 33.

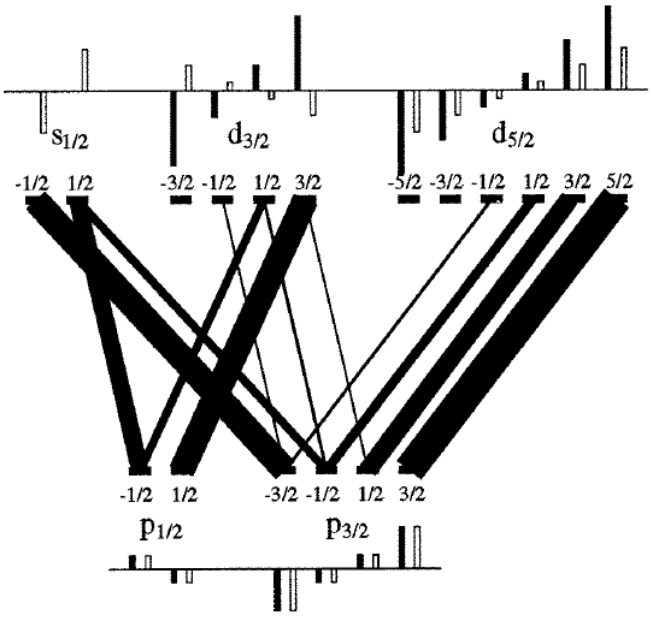

Fig. 2.18: Dipole-allowed transitions from the $2p_{3/2}$ and $2p_{1/2}$ core states to the $3d_{5/2}$ and $3d_{3/2}$ valence states with a left circularly polarized x-ray. The transition probability are reflected by the thickness of the lines. All plots are reproduced from Ref. 33.

CHAPTER 3

EXPERIMENTAL METHODS

Parts of this chapter were published in "Indirect heating of Pt by short-pulse laser irradiation of Au in a nanoscale Pt/Au bilayer" Gyung-Min Choi, Richard B. Wilson, and David G. Cahill, Phys. Rev. B **89**, 064307 (2014).

3.1 Time-Resolved Magneto-Optical Kerr Effect (TRMOKE)

I use TRMOKE to measure spin signal in chapter 4, 5, and 6. The spin signal could be demagnetization of ferromagnet, spin accumulation on non-magnet, or magnetization dynamics of ferromagnet. The interpretation of TRMOKE is based on the assumption that the rotation of the reflected light is proportional to the spin signal.

3.1.1 Physics of MOKE

The MOKE describes the change in the polarization of light when the light is reflected off of a magnetized material, either by spontaneous magnetization or applied magnetic field. For the case of transmitted and reflected light, the effect is referred to as the Faraday effect and Kerr effect, respectively (Fig. 3.1). Both effects have the same origin and can, therefore, be explained using a similar formalism. Since our experiments are carried out in the reflection in the following, I will mainly focus on the Kerr effect.

Linearly polarized light can be described as a superposition of two circularly polarized components with opposite helicities. Due to the magnetization of the medium, these two helicities of light have different refractive indexes. Consequently, a linearly polarized laser beam reflecting off a magnetic sample will undergo a complex Kerr rotation. The optical response is fully described by the dielectric tensor. For isotropic materials with both magnetization and light wavevector along z-axis (polar MOKE configuration), the dielectric tensor is [1, 2],

$$\varepsilon = \begin{pmatrix} \varepsilon_{xx} & \varepsilon_{xy} & 0 \\ -\varepsilon_{xy} & \varepsilon_{xx} & 0 \\ 0 & 0 & \varepsilon_{xx} \end{pmatrix}. \tag{3.1}$$

In this case, two eigenmodes of left-handed circularly polarized light (LCP) and right-handed circularly polarized light (RCP) are described by two eigenvalues of $\varepsilon_{\pm} = \varepsilon_{xx} \pm i\varepsilon_{xy}$, respectively. The different dielectric tensors for LCP and RCP lead to a complex Kerr rotation by [1, 2],

$$\tilde{\theta}_K = \frac{\varepsilon_{xy}}{(\varepsilon_{xx}-1)\sqrt{\varepsilon_{xx}}} = \frac{\sigma_{xy}}{\sigma_{xx}\sqrt{1+\frac{i}{\omega\varepsilon_0}\sigma_{xx}}}, \tag{3.2}$$

where ε_{ij} is the complex dielectric tensor and σ_{ij} is the complex conductivity tensor, which are related by $\varepsilon_{ij} = \delta_{ij} + \frac{i}{\omega\varepsilon_0}\sigma_{ij}$, ε_0 is the vacuum permittivity, and ω is the light frequency.

The conductivity tensor has contributions from interband and intraband transitions. When measuring MOKE with 3*d*-transition ferromagnet with light energy above 1 eV, σ_{xy} mostly due to the interband transition. The real and imaginary parts of σ_{xy} are linked by the Kramers-Kronig relation, and the imaginary part of σ_{xy} is obtained by Kubo formalism [1, 3],

$$\sigma''_{xy} = \frac{\pi e^2}{4\hbar\omega m^2\Omega}\sum_{i,f} f(E_i)\left[1 - f\left(E_f\right)\right][|\langle i|p_-|f\rangle|^2 - |\langle i|p_+|f\rangle|^2]\delta\left(\omega_{fi} = \omega\right), \tag{3.3}$$

where $p_{\pm}=p_x \pm p_y$, $f(E)$ is the Fermi-Dirac distribution, Ω is the total volume, and $\hbar\omega_{fi}=E_f-E_i$. The above expression is interpreted straightforwardly in terms of the absorption of a photon by an electron transiting between an occupied initial state $|i\rangle$ and an unoccupied final state $|f\rangle$. In addition to the energy conservation of $\delta(\omega_{fi}-\omega)$, the transition also conserves momentum by $\delta^{(3)}(\vec{k}_i-\vec{k}_f)$ because the momentum of light is negligible compared to the momentum of electron. The matrix elements $\langle i|p_-|f\rangle$ and $\langle i|p_+|f\rangle$ correspond to dipolar electric transitions, for RCP and LCP, respectively.

The dipolar electric transition also obeys the selection rules, i.e.,

$$\Delta l = \pm 1, \tag{3.4}$$

$$\Delta m_l = \pm 1, \tag{3.5}$$

where, l is the orbital quantum number, and m_l is the magnetic quantum number. The first selection rule implies that only transitions between *s* and *p* levels or *p* and *d* levels are allowed. For the second selection rule, the transitions with $\Delta m_l = +1$ and $\Delta m_l = -1$ correspond to left and right circularly polarized light, respectively.

When I consider 3*d* transition ferromagnet, the dominant interband transition is between 3*d* and 4*p* levels. Due to the exchange splitting, the spin-up and spin-down sub-bands are shifted, and due to the spin-orbit coupling, energy level is further shifted depending on the total angular momentum quantum number, $j=l-s$ or $j=l+s$ (Fig. 3.2). These shifts in energy levels result in different absorption between LCP and RCP. Therefore, in a bulk ferromagnet, the Kerr effect arises from the simultaneous occurrence of exchange splitting and spin-orbit splitting.

3.1.2 Time-resolved measurement of MOKE

In order to achieve a time resolution of a few hundreds of femtosecond, I use a pump-probe technique: the sample is brought out of equilibrium by a strong pump beam and its subsequent evolution is probed by a weak probe beam with controlled time delay. A femtosecond mode-locked Ti: sapphire laser provides a pulsed light with repetition rate of ≈80 MHz and splits into pump and probe beams by a polarized beam splitter. The full width at half maximum (FWHM) of pump and probe beams are ~0.8 and ~0.3 ps, respectively, without any optical filter (Fig. 3.3). The FWHM of pump is larger than that of the probe because of the large dispersion of the electro-optic modulator.

In the TRMOKE experiments I use a double modulation scheme (Fig. 3.4): the pump beam is modulated by an electro-optical modulator at ~10 MHz; the probe beam is modulated by a mechanical chopper at ~200 Hz. The double modulation is used to suppress the artifacts that occur at the same frequency as the modulation of the pump beam, such as diffuse pump scattering and unfiltered pump-light. Pump and probe beams are focused on samples with a near normal incident angle and $1/e^2$ radius of ~6 μm using a 10x objective lens. They can be on the same side or opposite side of samples depending on experiments.

The reflected probe beam is passing through ½ wave plate whose angle is 45^o and separated to vertical and horizontal polarization with respect to the optical table using Wollaston prism. Then the balanced detector measures the difference between intensities of vertical and horizontal polarization. When there is no Kerr rotation, the reflected probe beam is a linearly polarized with angle of 45^o after the ½ wave plate, and the Wollaston prism gives an equal amount of vertical and horizontal polarization. When there is a Kerr rotation, there is a difference between vertical and horizontal polarization, which is proportional to the real part of the Kerr rotation.

The Kerr rotation can be described by the Jones matrix,

$$\begin{pmatrix} E_{out}^{s} \\ E_{out}^{p} \end{pmatrix} = M_{1/2}(\alpha) M_{Kerr}(\tilde{\theta}) \begin{pmatrix} E_{in}^{s} \\ E_{in}^{p} \end{pmatrix}, \tag{3.6}$$

$$\begin{pmatrix} E_{in}^{s} \\ E_{in}^{p} \end{pmatrix} = E_0 \begin{pmatrix} 1 \\ 0 \end{pmatrix}, \tag{3.7}$$

$$M_{Kerr}(\tilde{\theta}) = r_s \begin{pmatrix} 1 & \tilde{\theta} \\ -\tilde{\theta} & r_p/r_s \end{pmatrix}, \tag{3.8}$$

$$M_{1/2}(\alpha) = \begin{pmatrix} \cos(\alpha) & -\sin(\alpha) \\ \sin(\alpha) & \cos(\alpha) \end{pmatrix}, \tag{3.9}$$

where E_{in}^{s} and E_{in}^{p} are vertical and horizontal components of electric field of incident probe beam, E_{out}^{s} and E_{out}^{p} are vertical and horizontal components of electric field of the reflected probe beam (after ½ wave plate), M_{Kerr} is the rotation matrix by the magnetized sample with the complex Kerr rotation of $\tilde{\theta}$, $M_{1/2}$ is the rotation matrix by the ½ wave plate with the angle of α. At the α of 45°, the intensity difference between vertical and horizontal components of reflected probe beam is equal to the real part of $\tilde{\theta}$,

$$\frac{|E_{out}^{p}|^2 - |E_{out}^{s}|^2}{|E_{out}^{p}|^2 + |E_{out}^{s}|^2} = \mathrm{Re}\{\tilde{\theta}_{Kerr}\}. \tag{3.10}$$

The imaginary part of $\tilde{\theta}$ can be measured by inserting ¼ wave plate in the path of the reflected probe beam.

For the balanced detector, I use Thorlabs PDB 450A (150 MHz, gain switchable Balanced Amplified Photodetector). With the transimpedence gain of 10^4 V/A and the power of reflected probe beam of 0.5 mW at each detector, the noise level is around 100 nV/$\sqrt{\mathrm{Hz}}$. The relationship between voltage signal and rotation angle is determined by manually rotating the probe beam: 1 V

corresponds to 10 ^{o} or 0.174 rad (Fig. 3.5). With time constant of 0.7 sec during the measurement, the noise level of 100 $nV/\sqrt{Hz}$ corresponds to the resolution of the Kerr rotation of ~2×10^{-8} rad, and further reduction of noise can be achieved by averaging of multiple measurements.

3.2 Time-Domain Thermoreflectance (TDTR)

I use TDTR to measure temperature of non-magnetic layers in chapter 6. Temperature measurement combined with thermal modeling enables to quantify heat current in metallic multilayers. The interpretation of TDTR is based on the assumption that the reflectivity of the reflected light is proportional to temperature.

3.2.1 Interpretation of TDTR

The TDTR is an ultrafast optical pump-probe technique to measure temperature evolution on a metal film utilizing the change in optical reflectivity with temperature, known as thermoreflectance dR/dT [4, 5]. The reflectivity of metals depends on both electron and phonon temperatures, $\Delta R = a\Delta T_e + b\Delta T_{ph}$, but the dominant contribution comes from phonon temperature unless the electron temperature excursion is very high. A high T_e only exists during the pump pulse, and T_e and T_{ph} equilibrate after a few ps. Therefore, I can assume $\Delta R \approx \Delta T_{ph}$ after a few ps of the pump pulse.

In the TDTR measurement, the observed change in reflectivity has contributions from the temperatures of the metal layer at varying depths below the surface [6]. The weighting function extends over a distance that is approximately the same as the optical attenuation depth. As a

example, I calculate dR/dT vs. film depth from an optical model (transfer matrix method) using the previously reported temperature coefficients of refractive indexes of Pt and Au [7] (Fig. 3.6).

The ΔR signal after the pump pulse is collected by the lock-in amplifier and consists of in-phase signal (V_{in}) and out-of-phase signal (V_{out}). To a good approximation at high modulation frequencies, the V_{in} is proportional to the time-domain thermal response of the sample, i.e., the temperature excursion created by the pump pulse. The V_{out} is mostly determined by the imaginary part of the frequency domain response at the modulation frequency and is approximately independent of delay time. Therefore, I interpret the ratio $|V_{in}/V_{out}|$ as the temperature excursion normalized by the amount of energy absorbed per pulse.

Often, TDTR is used with a metal/oxide (or semiconductor) structure to measure thermal conductivity of the oxide (or semiconductor) and thermal conductance of the metal/oxide (or metal/semiconductor) interface. In this case, a typical time range of analysis is from 100 ps to 4 ns. In my experiment, I use multiple metal layers on top of the sapphire substrate. To analyze thermal transport among multiple metal layers, the time range for most cases is from 0 to 200 ps. After 200 ps, all metal layers are thermally equilibrated and time evolution of TDTR signal is due to total heat capacity of metal layers, thermal conductivity of sapphire (know to be around 30 W m^{-1} K^{-1}), and thermal conductance at metal/sapphire interface (known to be around 100 MW m^{-2} K^{-1}).

3.2.2 Analysis of TDTR using transmission-line circuit model

To analysis TDTR measurements of metallic multilayers even at a few picoseconds, one needs to distinguish electron and phonon systems because they could be out-of-equilibrium for

quite long time when electron-phonon coupling differs a lot in the multilayers. In addition, temperature of electrons or phonons could be different spatially even in the same layer. To make the analysis as quantitative as possible, I analyze thermal transport using a transmission-line circuit model (Fig. 3.7). The circuit model is a discretized version of the continuum two-temperature model (2TM) [8]. I use the circuit model because it is easier to solve than the continuum 2TM equation when the electronic heat capacity, electronic thermal conductivity, and electronic thermal conductance depend on temperature. The discretized model should give the same result as the continuum model as long as the discrete length scale is sufficiently small; I choose the discrete length of the circuit model to more than three times smaller than the characteristic length scale for electron-phonon coupling of $\sqrt{\frac{\Lambda_e}{g_{ep}}}$, where Λ_e is the electronic thermal conductivity and g_{ep} is the electron-phonon coupling parameter.

Figure 3.7 shows a schematic of the approach for the sapphire/Pt/Au structure, where the five capacitors represent the heat capacities for Pt electrons (C_{e_Pt}), Au electrons (C_{e_Au}), Pt phonons (C_{ph_Pt}), Au phonons (C_{ph_Au}), and sapphire phonons (C_{ph_sap}), respectively; and the five resistors represent electron-phonon coupling of Pt (g_{Pt}), electron-phonon coupling of Au (g_{Au}), the electronic thermal conductance of the Pt/Au interface (G_{ee}), the phonon thermal conductance of the Pt/Au interface ($G_{ph\_Pt/Au}$), and the phonon thermal conductance of the sapphire/Pt interface ($G_{ph\_sap/Pt}$).

$$C_1 = C_{e\_Pt}Ah_{Pt}, C_2 = C_{e\_Au}Ah_{Au}, C_3 = C_{ph\_Pt}Ah_{Pt}, C_4 = C_{ph\_Au}Ah_{Au}, C_5 = C_{ph\_sap}Ah_{sap}, \quad (3.11)$$

$$R_1 = \frac{1}{Ah_{Pt}g_{Pt}}, \quad R_2 = \frac{1}{Ah_{Au}g_{Au}}, \quad R_3 = \frac{1}{AG_{ee}}, \quad R_4 = \frac{1}{AG_{ph\_Pt/Au}}, \quad R_5 = \frac{1}{AG_{ph\_sap/Pt}}, \quad (3.12)$$

where A is the area and, h is the thickness. Excitation by the pump beam is represented by the current sources *I1* and *I2* that are connected to Pt and Au electrons, respectively. Voltages of each capacitor represent the temperature excursions of each heat reservoir.

To model the thermal transport within each layer, the individual layers that are demarcated by blue dashed lines in Fig. 3.7 (a) are divided into multiple sublayers (Fig. 3.7 (b)). In other words, I divide the single capacitors of each layer into multiple sub-capacitors and connect them with resistors that represent thermal resistance by electronic thermal conductivity, phonon thermal conductivity, and electron-phonon coupling.

$$C_{sub} = CAh_{sub}, \quad R_{ee} = \frac{h_{sub}}{A\Lambda_e}, \quad R_{pp} = \frac{h_{sub}}{A\Lambda_{ph}}, \quad R_{ep} = \frac{1}{Ah_{sub}g}, \tag{3.13}$$

where h_{sub} is the sublayer thickness, Λ_e is the electronic thermal conductivity, and Λ_{ph} is the phonon thermal conductivity. I use 2 nm and 10 nm for the thickness of the sublayers of the Pt and Au layers, respectively.

Values for heat capacity is taken from literature and those for thermal conductivity are obtained from electrical conductivity measurements and Wiedemann-Franz law. In the case of my work in chapter 6, the fitting parameter is the electron-phonon coupling (g). For the case of the Pt/Au bilayer, g_{Au} controls the equilibration time between Pt and Au, and g_{Pt} only affect the initial energy distribution between Pt and Au at around 1 ps because $g_{\mathrm{Pt}} >> g_{\mathrm{Au}}$. In Fig. 3.8, I show the fitting result of thermal modeling with $g_{\mathrm{Pt}} = 4.2\times10^{17}$ and $g_{\mathrm{Au}} = 2.2\times10^{12}$ W m^{-3} K^{-1}.

3.3 References

1. H. Ebert, Rep. Prog. Phys. **59**, 1665 (1996).

2. J. Schoenes, Magneto-Optical Properties of Metals, Alloys, and Compounds. *Materials Science and Technology* (Wiley, 2006).
3. P. Bruno, Y. Suzuki, and C. Chappert, Phys. Rev. B **53**, 9214 (1996).
4. D. G. Cahill, K. Goodson, and A. Majumdar, J. Heat Transfer **124**, 223 (2002).
5. D. G. Cahill, Rev. Sci. Instrum. **75**, 5119 (2004).
6. G.-M. Choi, R. B. Wilson, and D. G. Cahill, Phsy. Rev. B **89** 064307 (2014).
7. R. B. Wilson, B. A. Apgar, L. W. Martin, and D. G. Cahill, Opt. Exp. **20**, 28829 (2012).
8. T. Q. Qiu and C. L. Tien, Int. J. Heat Mass Transfer **37**, 2789 (1994).

3.4 Figures

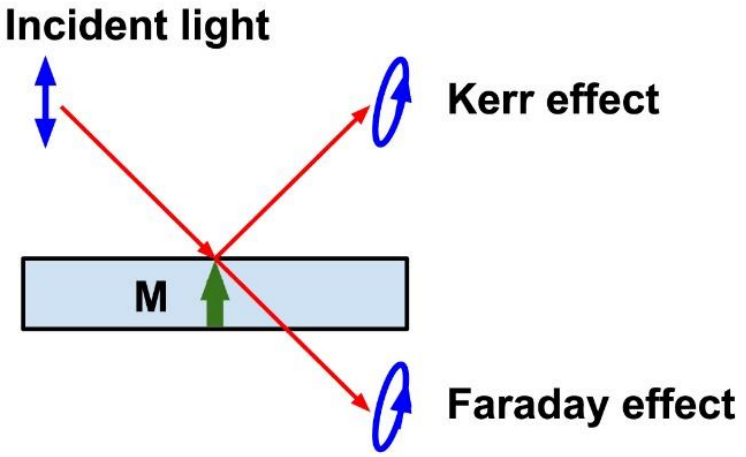

Fig. 3.1: Schematic illustration of Faraday effect and Kerr effect by the interaction between light and magnetization.

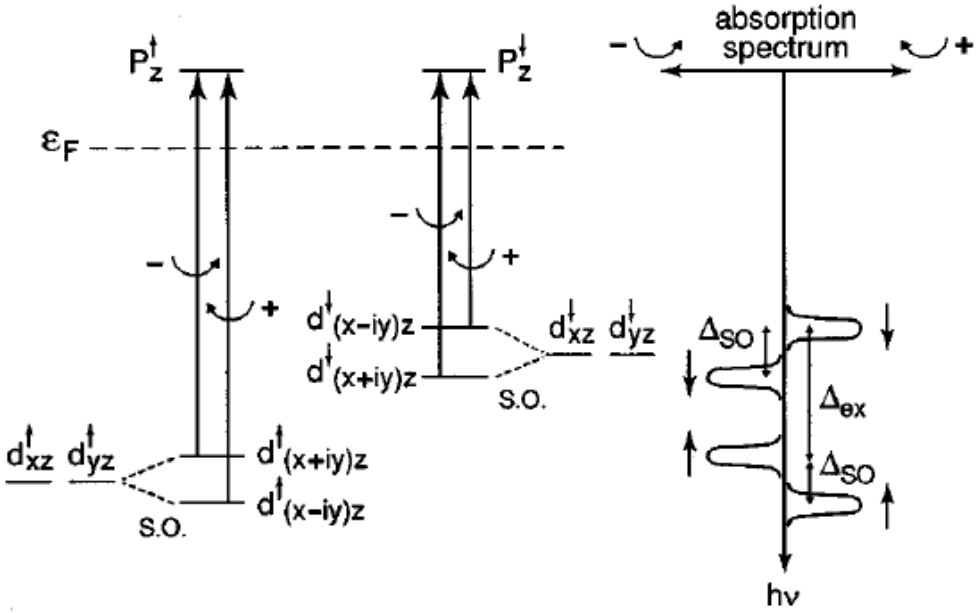

Fig. 3.2: Schematic of energy levels in a ferromagnet. Δ_{ex} is the exchange splitting, and Δ_{SO} is the spin-orbit splitting. All plots are reproduced from Ref. 3.

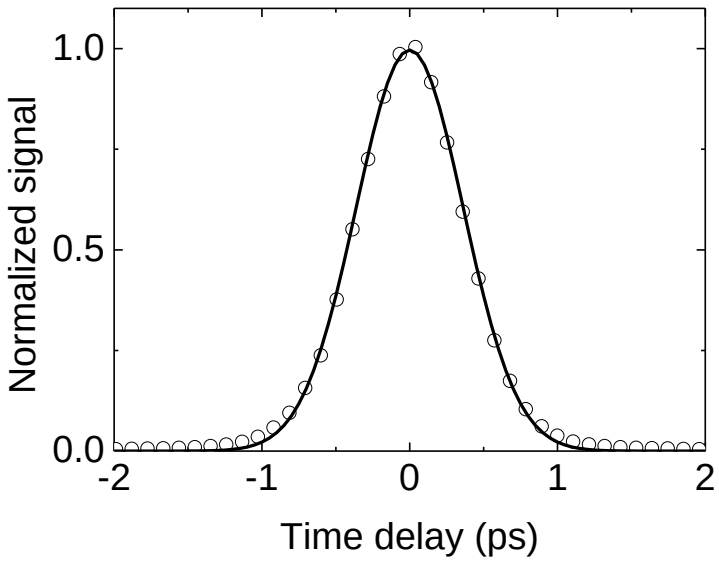

Fig. 3.3: The measured time correlation between pump and probe with GaP detector (black circles). The solid line is the calculated time correlation with FWHM of 0.8 and 0.3 ps for pump and probe, respectively.

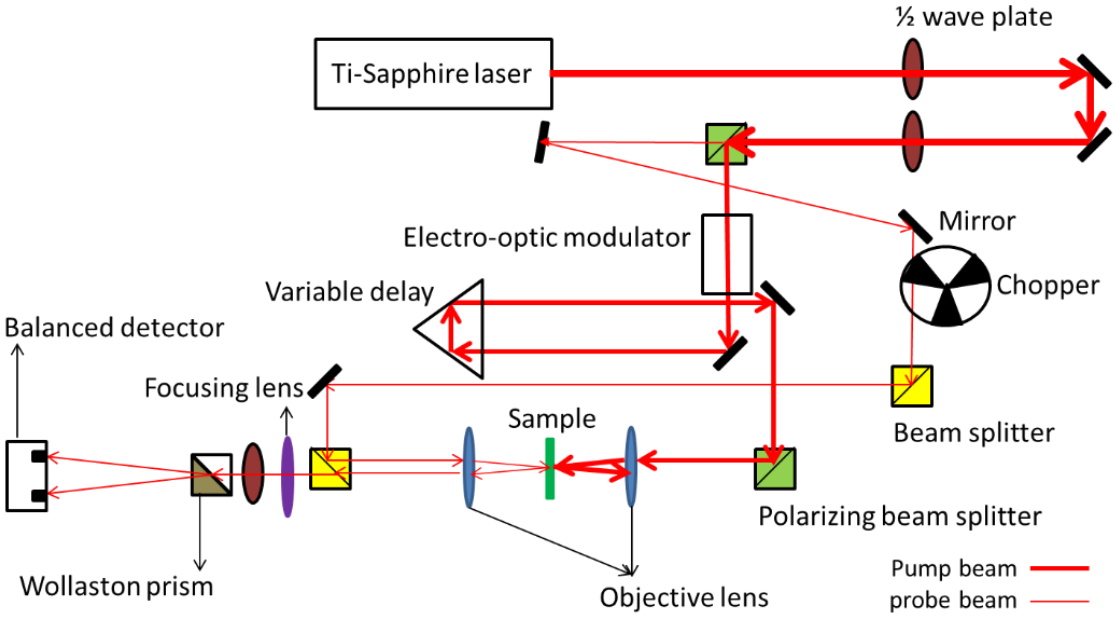

Fig. 3.4: Schematic illustration of TRMOKE setup. Pump and probe beams are incident on the opposite side of the sample. The Kerr rotation of the reflected probe beam is measured by the balanced detector.

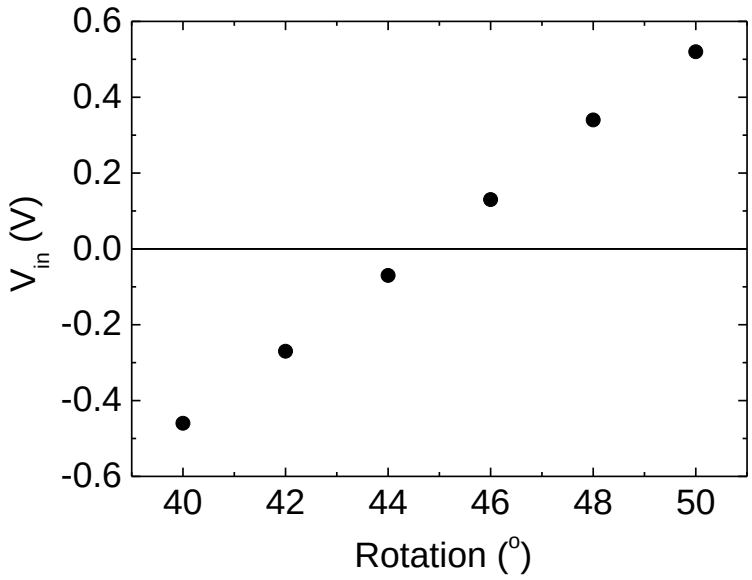

Fig. 3.5: The measured voltage response of the balanced detector by manually rotating ½ wave plate.

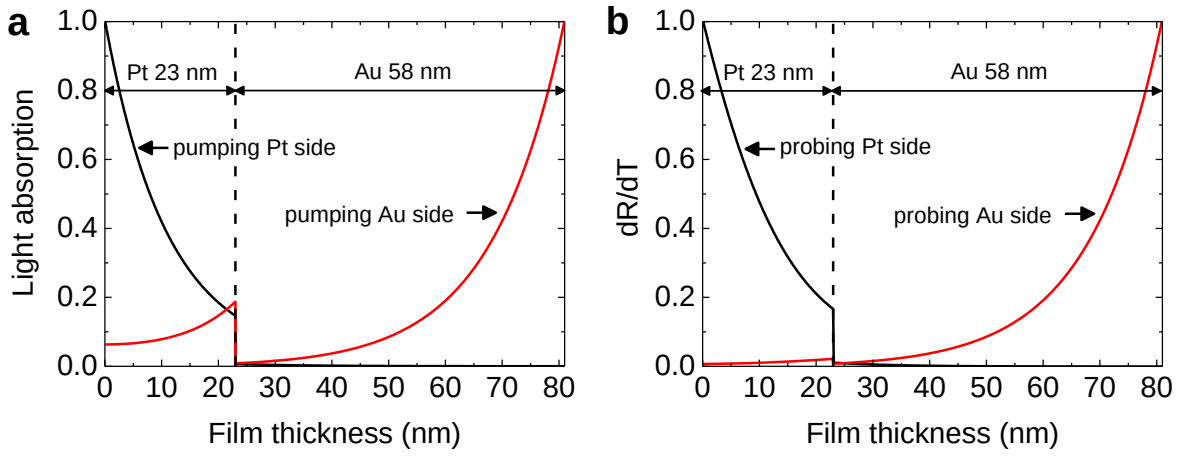

Fig. 3.6: (a) The distribution of light absorption as a function of depth in the Pt (23)/ Au (58) bilayer. The calculation is done by a transfer matrix method with refractive indexes of Pt and Au, 2.67+i5.9 and 0.15+i4.90, respectively. The light absorption of the pump beam incident on the Pt/sapphire interface is shown as a black line, and that for the pump beam incident on the Au surface is shown as a red line. (b) The reflectance (dR/dT) weighting factor of the Pt (23)/ Au (58) bilayer. The calculation is done by the transfer matrix method with refractive indexes as well as temperature coefficients of those, $dn_{Pt}/dT = 2.6\times10^{-4}$ K^{-1}, $dk_{Pt}/dT = -3\times10^{-4}$ K^{-1}, $dn_{Au}/dT = 2\times10^{-4}$ K^{-1}, and $dk_{Au}/dT = 0$. The black solid line corresponds to when light is incident on the Pt side, and the red solid line corresponds to when light is incident on the Au side [6].

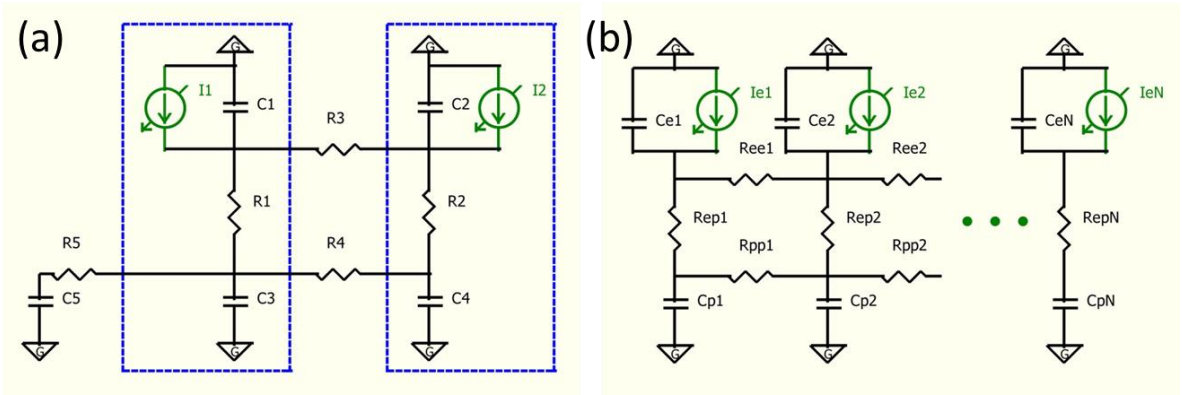

Fig. 3.7: (a) Equivalent circuit for modeling the thermal transport between the Pt/Au bilayer. *C*, *R*, *I* represent capacitors, resistors, and current source, respectively. *C1* and *C2* represent the electronic heat capacities of the Pt and Au layers. *C3*, *C4*, and *C5* represent the corresponding lattice heat capacities of the Pt, Au, and sapphire layers; *R1* and *R2* represent the thermal resistances due to the electron-phonon coupling of the Au and Pt layers; *R3* represents the thermal resistance due to the electronic thermal conductance of the Pt/Au interface; *R4* and *R5* represent the thermal resistances due to the phonon thermal conductance of the Pt/Au and sapphire/Pt interfaces, respectively; and *I1* and *I2* represent the current sources, which mimic the excitation of electrons of the Pt and Au layers by the pump optical pulse. (b) Transmission line model for each layer. *Ce* and *Cp* represent the heat capacities of electrons and phonons, respectively, of each sublayer; *Ree* and *Rpp* represent the thermal resistances due to electronic and phonon, respectively, thermal conductivities between sublayers; *Rep* represents the thermal resistance due to electron-phonon coupling of the sublayer; *Ie*, the current source, represents the excitation of electrons of the sublayer by the pump optical pulse [6].

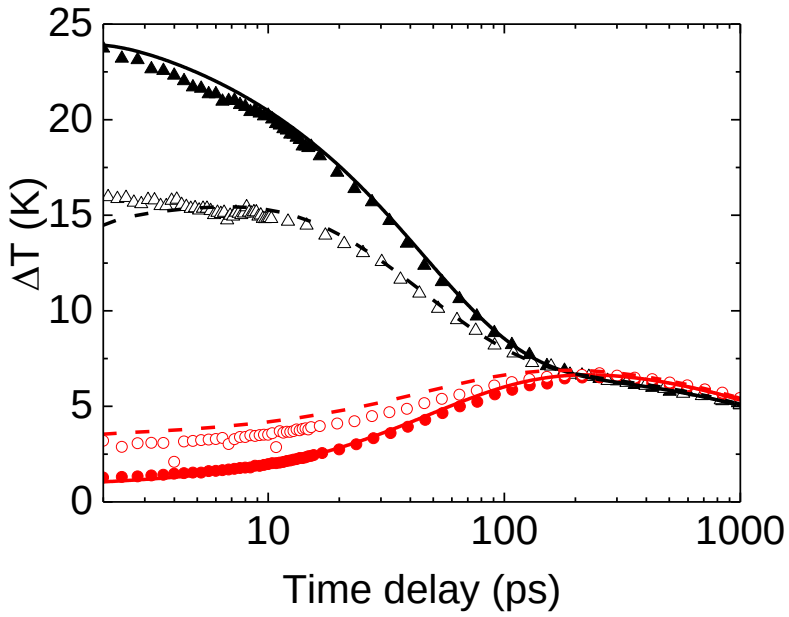

Fig. 3.8: TDTR data of the sapphire/ Pt (23)/ Au (58) sample with four different configurations of the pump and probe beams: i) pump and probe at the Pt side of the bilayer (▲); ii) pump at Au surface and probe at the Pt side (△); iii) pump at the Pt side and probe at the Au surface (●); and iv) pump and probe at the Au surface (○). Solid and dashed lines are for the thermal modeling with $g_{Pt} = 4.2\times10^{17}$ and $g_{Au} = 42.2\times10^{12}$ W m^{-3} K^{-1}; black lines are for Pt phonon temperatures and red lines are for Au phonon temperatures; Solid lines are for the pump beam incident on the Pt side of the bilayer and dashed lines are for the pump beam incident on the Au surface [6].

CHAPTER 4

DEMAGNETIZATION-DRIVEN SPIN ACCUMULATION

Parts of this chapter were published in "Kerr rotation in Cu, Ag, and Au driven by spin accumulation and spin-orbit coupling" Gyung-Min Choi and David G. Cahill, Phys. Rev. B **90**, 214432 (2014).

4.1 Introduction

In metallic spintronic devices, spin injection from a ferromagnet (FM) to a nonmagnetic metal (NM) is a central issue. Experimental investigations of the spin injection require a method to generate spin current from FM and detect spin accumulation in NM. The generation of spin currents has been achieved by passing charge currents through FM [1, 2], by passing heat currents through FM [3], by spin pumping [4], and by spin Hall effect [5]. These methods operate on time scales that are long compared to the time scales of spin relaxation and spin diffusion; therefore, the spin currents generated by these methods are essentially in steady-state.

Spin accumulation in NM can be detected electrically using a second FM [1, 2] or via the inverse spin Hall effect [6]. Recently, optical detection of spin accumulation in NM has been reported [7, 8]. Fohr *et al.* used Brillouin light scattering to measure stationary spin accumulation

in NM produced by spin pumping [7]. Melnikov *et al.* used the polarization of optical second harmonic generation to measure transient spin accumulation in Au [8], and their interpretation is based on the superdiffusive model that explains the demagnetization-driven spin current by the spin-dependent transport of hot carriers [9]. In Ref. [8], the constant of proportionality that relates the rotation of polarization and spin accumulation was not studied by either experiment or theory.

In this work, I show ultrafast demagnetization of FM can generate a transient spin accumulation in NM, and the spin accumulation can be detected by the linear magneto-optical Kerr effect (MOKE) [10]. MOKE is conventionally applied to studies of metallic FM and semiconductors. Our results show that spin accumulation in NM also produces a useful MOKE signal that has its origin in spin-orbit coupling.

4.2 Experiment

The concept of how I generate a spin accumulation on NM from demagnetization of FM is shown schematically in Fig. 4.1. The pump laser pulse excites the Pt layer and leads to the demagnetization of FM by thermal transport from Pt to FM. The ultrafast demagnetization of FM generates a spin current by electron-magnon coupling in FM, and the generated spins accumulate on NM by spin diffusion. The spin accumulation on NM can be measured by TRMOKE.

I prepared FM/NM structure of sapphire substrate/ Pt (20)/ FM (6)/ NM (*h*) (unit in nm). The FM is a [Co/Pt] multilayer with perpendicular magnetization ([Co (0.4)/ Pt (1)]$_{\times 4}$/ Co (0.4)), and the NM layer is Cu, Ag, or Au. Depending on the thickness of NM, I refer these samples as the Cu-*h*, Ag-*h*, or Au-*h* sample. Metal layers are deposited by magnetron sputter at University of

Illinois (UIUC). For Cu and Ag samples, I deposit a thin topcoat of SiO_2 by e-beam evaporation to protect Cu and Ag from oxidation or corrosion by sulfides.

I apply a laser pulse on the Pt side of the samples to minimize the contribution from hot electron transport with excess energy on the order of the photon energy [9]. The inelastic mean free path of hot electrons in Pt is ≈5 nm [11]. Because the [Co/Pt] multilayer is indirectly heated by a relatively thick Pt layer (20 nm), the strong electron-electron and electron-phonon scattering in Pt [12] should greatly suppress the density of hot electrons that reach the [Co/Pt] layer. When the density of far-from-equilibrium hot electrons is negligible in the [Co/Pt] layer, the superdiffusive model [9] does not predict the demagnetization or a demagnetization-induced spin current.

The magnetic properties of the [Co/Pt] layer were characterized with a vibrating sample magnetometer by our colleagues at Korea Institute of Science and Technology (KIST): the saturation magnetization is 4×10^5 A m^{-1}, the coercivity is 0.09 T, and the remanence is close to one. Electric conductivities of the Pt, [Co/Pt], Cu, Ag, and Au layers are measured using a four-point probe with separately prepared samples (sapphire/ Pt (100), sapphire/ Pt (2)/ [Co (0.4)/ Pt (1)]$_{\times15}$/ Pt (1), sapphire/ Cu (100), sapphire/ Ag (100), and sapphire/ Au (100)) and are summarized in Table 4.1.

I use time-resolved polar MOKE to detect the transient spin accumulation in the direction normal to the film. The light wavelength is 785 nm, and the full-width-at-half-maximum of the pump and probe are ≈0.8 and ≈0.3 ps, respectively. The incident pump fluence is 10.6 J m^{-2}; the absorbed fluence is 3.7 J m^{-2}. A perpendicular magnetic field of ±0.3 T was applied to samples before MOKE measurement to set the [Co/Pt] magnetization to ±z direction. All measurements are done at room temperature without magnetic field.

4.3 Results and discussion

When both pump and probe beams are incident on the Pt side of the samples, I observe a rapid demagnetization of [Co/Pt] on a sub-picosecond timescale followed by a slow recovery (Fig. 4.2). By comparing the transient Kerr rotation (ΔM) and static Kerr rotation (M), I determine the peak $\Delta M/M$: 0.25±0.04, 0.25±0.04, and 0.28±0.04, for Cu, Ag, and Au samples, respectively. Therefore, to within experimental uncertainties, the peak change in magnetization is independent of the composition of the NM layer. (The rate of recovery of magnetization is reduced in the Au sample because Au has weaker electron-phonon coupling than Cu or Ag.) The demagnetization data are also independent of the NM thickness.

To model the spin current generation, I assume that electron-magnon coupling conserves spin-angular-momentum. Adapting the viewpoint that demagnetization is a result of excitation of magnons [13-15], the spin loss by demagnetization (magnon excitation) should be converted to spin generation, i.e., spin polarization in the electrons. The angular momentum conservation of electron-magnon coupling was implicitly considered by several prior reports to explain ultrafast demagnetization [14, 16, 17]. Owing to this conservation, the demagnetization-driven spin generation rate is the negative of the demagnetization rate,

$$g_S = -\frac{dM}{dt}. \tag{4.1}$$

I obtain dM/dt from the time derivative of measured $M(t)$. In contrast to the superdiffusive model [9], our model is a thermodynamic description of demagnetization-induced spin generation: the temperature difference between electron and magnon drives flows of energy and spin-angular-momentum.

Spin generated in [Co/Pt] accumulates in NM via spin diffusion [18]. In Fig. 4.3, I plot time-resolved measurements of the spin accumulation in NM by probing Kerr rotation at the surface of NM; the probe beam is incident on the Cu, Ag, or Au side of the samples while the pump beam is incident on the Pt side of the samples. The Kerr rotation changes sign when the [Co/Pt] magnetization is changed from the +*z* to the –*z* direction and closely resembles the rate of change of magnetization plotted in Fig. 4.2 (b). At an NM thickness of 100 nm, the peak Kerr rotation is the highest in Au, but it decreases more quickly with thickness than Cu and Ag.

To quantify the spin accumulation, I use the spin diffusion equation [18] including spin generation terms,

$$\frac{\partial \mu_S}{\partial t} = D\frac{\partial^2 \mu_S}{\partial^2 z} - \frac{\mu_S}{\tau_S} + \left(\frac{g_S}{N_S}\right), \tag{4.2}$$

where $\mu_S=\mu_\uparrow-\mu_\downarrow$ is the spin chemical potential, D is the spin diffusion constant, τ_S is the spin relaxation time, g_S is the spin generation rate, and N_S is the spin density of states ($N_S = \frac{N_{FM1}}{2}$, where N_{FM} is the electronic density of states of FM). The D of Pt, [Co/Pt], Cu, and Au are calculated by $D = \frac{\sigma}{e^2 N_F}$, where σ is the electrical conductivity and N_F is the density of states at the Fermi level, $N_F = \frac{3\gamma}{\pi^2 k_B^2}$, where γ is the electronic heat capacity coefficient [19], and k_B is the Boltzmann constant. The τ_S is related to the spin diffusion length l_S, $\tau_S = \frac{l_S^2}{D}$. The l_S values at room temperature are reported to be 7~10 nm for Pt [20, 21], 350~500 nm for Cu [2, 22], 150 nm for Ag [23], and 60 nm for Au [22]. Assuming l_S of 8, 400, 150, and 60 nm, I obtain τ_S of 0.3, 16, 1.5, and 0.4 ps for Pt, Cu, Ag, and Au, respectively. The τ_S of [Co/Pt] is determined to be 0.01 ps from comparison between spin accumulation and STT results, which will be described in Chapter 5.

I solve the coupled diffusion equations for Cu-*h*, Ag-*h*, and Au-*h* samples by equating μ_S at interfaces and setting the spin generation rate of [Co/Pt] to be –d*M*/d*t*. The predicted spin accumulation n_S, $\mu_S = 2\frac{n_S}{N_F}$, at the surface of NM is shown in Fig. 4.4. The calculation is in good agreement with the positions of the positive-negative peaks and the thickness dependence. At the same NM thickness, the spin accumulation is the largest in Cu because of its relatively long l_S and large N_F.

The thickness dependence of the Kerr rotation can be explained with l_S of NM. While it has a weak dependence on the thickness of Cu and Ag, spin accumulation shows a much stronger dependence on the Au thickness due to the short l_S (Fig. 4.5). From the thickness dependence of the peak Kerr rotation in Au, I determine l_S=60±10 nm, which leads to τ_S=0.4±0.1 ps. Melnikov *et al.* observed a spin signal in Fe/Au structures and interpreted their data using a model based on ballistic transport of hot carriers [8]. From this analysis, the authors of Ref. 8 obtained a hot-carrier τ_S=1.2 ps for Au [8]. Our result of τ_S=0.4 ps, obtained from diffusive transport, is an important point of comparison with Ref. [8].

The τ_S of each layer has a different effect on spin accumulation in NM (Fig. 4.6). The τ_S of Pt does not affect the spin accumulation in NM because the low diffusivity of [Co/Pt] essentially decouples Pt from NM. The τ_S of [Co/Pt] has a dominant role in the spin accumulation in NM as it is the smallest time scale: spin accumulation in NM is approximately proportional to the τ_S of [Co/Pt]. At the NM thickness of 100 nm, the τ_S of Cu or Ag has little effect on the spin accumulation due to relatively long τ_S, while the τ_S of Au has a significant impact. Therefore, the critical parameters are τ_S of [Co/Pt] and Au, which are determined experimentally to be 0.01 and 0.4 ps.

As discussed in Chapter 3, the Kerr rotation has contributions from interband and intraband transitions, and that of 3*d*-transition ferromagnets mostly comes from interband transition. However, because our photon energy ($\hbar\omega$ =1.58 eV) cannot reach the *d*-bands of Cu, Ag, or Au which lie >2 eV below the Fermi level, I assume that only intraband transitions contribute to the Kerr rotation.

The conventional way to describe intraband transition is the Drude model [24, 25]. Within the assumptions of the Drude model, the diagonal and off-diagonal conductivity tensors are

$$\sigma_{xx} = \omega_P^2 \varepsilon_0 \frac{\left(\frac{1}{\tau} - i\omega\right)}{\left(\frac{1}{\tau} - i\omega\right)^2 + \omega_C^2} \approx i \frac{\omega_P^2 \varepsilon_0}{\omega}, \tag{4.3}$$

$$\sigma_{xy} = \omega_P^2 \varepsilon_0 \frac{\omega_C}{\left(\frac{1}{\tau} - i\omega\right)^2 + \omega_C^2} \approx -\left(\frac{\omega_P}{\omega}\right)^2 \varepsilon_0 \omega_C, \tag{4.4}$$

where ω_P is the plasma frequency, $\omega_p = \sqrt{\frac{ne^2}{m^* \varepsilon_0}}$, n is electron concentration, e is electron charge, m^* is effective mass, and ω_C is the cyclotron frequency, $\omega_C = \frac{eB}{m^*}$, and B is the magnetic field. Taking n from the free electron model and m^* from Ref. [26] (n = 8.45×10^{28}, 5.85×10^{28}, and 5.9×10^{28} m^{-3} for Cu, Ag, and Au, respectively, and $m^*=1.5m_e$ for Cu and $m^*=m_e$ for Ag and Au, where m_e is the electron rest mass), $\hbar\omega_P$ is 8.8, 9.0, and 9.0 eV for Cu, Ag, and Au, respectively. The approximation on the right hand side of the equation is the limit of $\omega >> 1/\tau$ and $\omega >> \omega_C$.

Kerr rotation of nonmagnetic metals (Al, Cu, Ag, and Au) has been investigated by applying a static magnetic field [24, 25] and explained by ω_C. Although a magnetic field can also produce spin accumulation by splitting the energy of spin sub-bands, the ω_C term dominates the measured Kerr rotation in noble metals.

Elezzabi *et al*. reported the Kerr rotation of an Au film induced by a transient magnetic field with a picosecond rise-time [27]. They interpreted the Kerr rotation as a result of the magnetic field driven spin accumulation and obtained $\tau_S \approx 45$ ps from the time delay between the magnetic field and Kerr rotation. I argue, however, that the Kerr rotation observed in Ref. [27] has a significant contribution from ω_C. Substituting (4.3) and (4.4) into (3.2), the magnetic field driven Kerr rotation is,

$$\tilde{\theta}_K = i\frac{\omega_C}{\omega}\frac{1}{\sqrt{1-\frac{\omega_P^2}{\omega^2}}} \approx \frac{\omega_C}{\omega_P} \tag{4.5}$$

The peak magnetic field of 50 mT of Ref. [27] produces $\hbar\omega_C \approx 6\times10^{-6}$ eV. Using $\hbar\omega_P$=9.0 eV, the Kerr rotation is ≈0.7 μrad, which is comparable to the observation of 0.45 μrad of Ref. [27]. Furthermore, $\tau_S \approx 45$ ps is inconsistent with a l_S of 60 nm of Au.

In materials such as TmS, TmSe, and Gd, it has been reported that the magnetic field driven Kerr rotation can have a significant contribution from spin accumulation [28-30]. However, in noble metals, the magnetic field driven Kerr rotation mostly comes from ω_C. Since I produce spin accumulation from demagnetization of a ferromagnet without a magnetic field, spin accumulation should be the only source of Kerr rotation in our experiments. I find no Kerr rotation in a control sample of Pt/Au (without [Co/Pt]), in which there is no demagnetization-induced spin accumulation.

Kerr rotation driven by spin accumulation can be described by skew scattering theory [28-30]. The contribution of spin accumulation to the off-diagonal conductivity tensor is

$$\sigma_{xy} = \frac{n_\uparrow - n_\downarrow}{n_\uparrow + n_\downarrow}\left(\omega_p^2\varepsilon_0\right)\frac{\Omega}{(1/\tau - i\omega)^2 + \Omega^2}, \tag{4.6}$$

where Ω is the skew scattering frequency. Substituting (4.6) into (3.2) and taking the limit $\omega >> 1/\tau$ and $\omega >> \Omega$,

$$\tilde{\theta}_K \approx \frac{n_\uparrow - n_\downarrow}{n_\uparrow + n_\downarrow}\left(\frac{\Omega}{\omega_p}\right), \tag{4.7}$$

I determine Ω for Cu, Ag, and Au by comparing the measured Kerr rotations (Fig. 4.3) and calculated spin accumulations (Fig. 4.4) for the Cu-100, Ag-100, and Au-100 samples. With $n_\uparrow - n_\downarrow$ from the peak spin accumulation in Fig. 4.4 divided by the Bohr magneton and $n_\uparrow + n_\downarrow$ from the free electron model, $\frac{n_\uparrow - n_\downarrow}{n_\uparrow + n_\downarrow}$ are 1.35×10^{-4}, 1.26×10^{-4}, and 0.64×10^{-4} for Cu-100, Ag-100, and Au-100, respectively. By comparing the experimental Kerr rotation with equation (4.7), I find $\hbar\Omega$ =0.02, 0.01, and 0.12 eV for Cu, Ag, and Au, respectively.

I equate $\hbar\Omega$ with the strength of spin-orbit coupling in the conduction band. The atomic spin-orbit splitting are 0.25 eV for Cu 3d, 0.03 eV for Cu 4p, 0.55 eV for Ag 4d, 0.11 eV for Ag 5p, 1.52 eV for Au 5d, and 0.47 eV for Au 6p [31], which are much larger than our values of $\hbar\Omega$. I speculate that the small values of $\hbar\Omega$ in our experiments can be attributed to the fact that the conduction band has a mostly *s* character and that the spin-orbit coupling I observe is generated by weak *s*-*d* or *s*-*p* hybridization. It is surprising that $\hbar\Omega$ of Ag is smaller than Cu despite larger atomic spin-orbit splitting. I speculate that the small $\hbar\Omega$ of Ag is because the *d*-band of Ag lies ≈4 eV below the Fermi level, a factor of ≈2 larger than Cu and Au. I also perform identical experiments with a Pt (20)/ [Co/Pt] (6)/ Al (100) sample and find no Kerr rotation presumably due to extremely small spin-orbit coupling in Al.

I note that an energy splitting of 0.11 eV for the surface states of Au (111) has been reported using photoemission spectra and interpreted as a result of spin-orbit coupling due to s-p

hybridization of the surface state [32]. Photoemission spectra were unable to resolve the energy splitting of Cu (111) or Ag (111) surface states [33]; theory predicts orders of magnitude smaller values of the splitting for Cu(111) or Ag(111) than Au (111) [34].

4.4 Conclusion

I achieve optical detection of the demagnetization-driven spin accumulation in Cu, Ag, and Au by magneto-optical Kerr effect. Our modeling well describes the time evolution of the Kerr rotation: the angular momentum conservation of electron-magnon coupling converts spin loss of demagnetization to spin generation in electrons of FM; generates spins in FM diffuse to NM by the spin diffusion process. The magnitude of the Kerr rotation is described by the product of spin accumulation and spin-orbit coupling of conduction bands of NM.

4.5 References

1. M. Johnson and R. H. Silsbee, Phys. Rev. Lett. **55**, 1790 (1985).
2. F. J. Jedema, A. T. Filip, and B. J. van Wees, Nature **410**, 345 (2001).
3. A. Slachter, F. L. Bakker, J-P. Adam, and B. J. van Wees, Nature Phys. **6**, 879 (2010).
4. Y. Tserkovnyak, A. Brataas, and G. E. W. Bauer, Phys. Rev. Lett. **88**, 117601 (2002).
5. S. O. Valenzuela and M. Tinkham, Nature **442**, 176 (2006).
6. T. Kimura, Y. Otani, T. Sato, S. Takahashi, and S. Maekawa, Phys. Rev. Lett. **98**, 156601 (2007).
7. F. Fohr, S. Kaltenborn, J. Hamrle, H. Schultheiss, A. A. Serga, H. C. Schneider, B. Hillebrands, Y. Fukuma, L. Wang, and Y. Otani, Phys. Rev. Lett. **106**, 226601 (2011).

8. A. Melnikov, I. Razdolski, T. O. Wehling, E. Th. Papaioannou, V. Roddatis, P. Fumagalli, O. Aktsipetrov, A. I. Lichtenstein, and U. Bovensienpen, Phys. Rev. Lett. **107**, 076601 (2011).
9. M. Battiato, K. Carva, and P. M. Oppeneer, Phys. Rev. Lett. **105**, 027203 (2010).
10. G.-M. Choi and D. G. Cahill, Phys. Rev. B **90**, 214432 (2014).
11. E. V. Chulkov, A. G. Borisov, J. P. Gauyacq, D. Sánchez-Portal, V. M. Silkin, V. P. Zhukov, and P. M. Echenique, Chem. Rev. **106**, 4160 (2006).
12. Z. Lin and L. V. Zhigilei, Phys. Rev. B **77**, 075133 (2008).
13. E. Beaurepaire, J.-C. Merle, A. Daunois, and J.-Y. Bigot, J.-Y. Phys. Rev. Lett. **76**, 4250 (1996).
14. A. Manchon, Q. Li, L. Xu, S. Zhang, Phys. Rev. B **85** 064408 (2012).
15. A. J. Schellekens and B. Koopmans, Phys. Rev. Lett. **110**, 217204 (2013).
16. B. Koopmans, G. Malinowski, F. Dalla Longa, D. Steiauf, M. Fähnle, T. Roth, M. Cinchetti, and M. Aeschlimann, Nature Mater. **9**, 259 (2010).
17. B. Y. Mueller, T. Roth, M. Cinchetti, M. Aeschlimann, and B. Rethfeld, New J. Phys. 13, 123010 (2011).
18. T. Valet and A. Fert, Phys. Rev. B **48**, 7099 (1993).
19. A. Tari, *The Specific Heat of Matter at Low Temperatures*. (Imperial College Press, London, 2003).
20. L. Vila, T. Kimura, and Y.C. Otani, Phys. Rev. Lett. **99**, 226604 (2007).
21. Y. Niimi, D. Wei, H. Idzuchi, T. Wakamura, T. Kato, and Y. Otani, Phys. Rev. Lett. **110**, 016805 (2013).
22. T. Kimura, J. Hamrle, and Y. Otani, Phys. Rev. B **72**, 014461 (2005).

23. R. Godfrey and M. Johnson, Phys. Rev. Lett. **96**, 136601 (2006).

24. E. A. Stern, J. C. McGroddy, and W. E. Harte, Phys. Rev. **135**, A1306 (1964).

25. S. E. Schnatterly, Phys. Rev. **183**, 664 (1969).

26. P. B. Johnson and R. W. Christy, Phys. Rev. B **6**, 4370 (1972).

27. A. Y. Elezzabi, M. R. Freeman, and M. Johnson, Phys. Rev. Lett. **77**, 3220 (1996).

28. J. L. Erskine and E. A. Stern, Phys. Rev. B **8**, 1239 (1973).

29. W. Reim, O. E. Hüsser, J. Schoenes, E. Kaldis, P. Wachter, and K Seiler, J. Appl. Phys. **55**, 2155 (1984).

30. W. Reim and J. Schoenes, *Ferromagnetic Materials* (Elsevier, New York, 1990).

31. C. E. Moore, *Atomic Energy Levels* (National Bureau of Standards, Washington, DC, 1949).

32. S. LaShell, B. A. McDougall, and E. Jensen, Phys. Rev. Lett. **77**, 3419 (1996).

33. G. Nicolay, F. Reinert, S. Hüfner, and P. Blaha, Phys. Rev. B **65** 033407 (2001).

34. G. Bihlmayer, Yu. M. Koroteev, P. M. Echenique, E. V. Chulkov, and S. Blűgel, Surf. Sci. **600**, 3888 (2006).

4.6 Figures and Tables

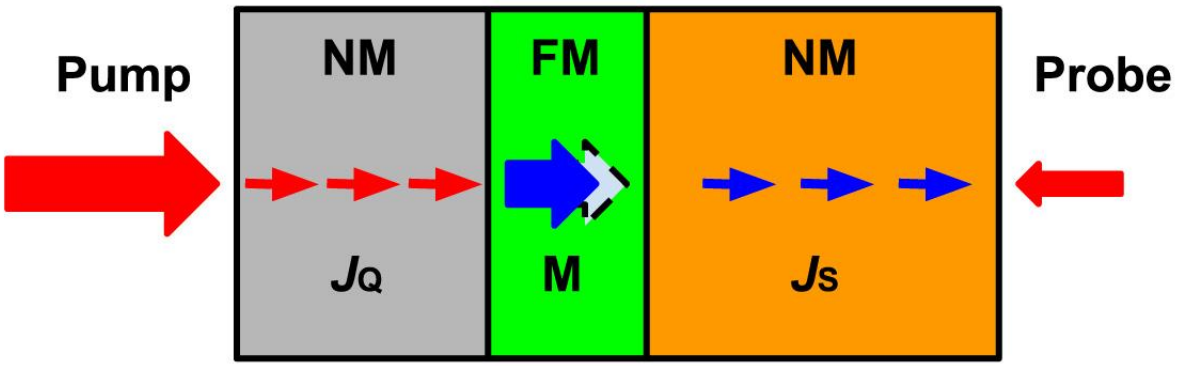

Fig. 4.1: A schematic illustration of the demagnetization-driven spin accumulation. Pump laser heat the first NM, and thermal transport from NM to FM leads to ultrafast demagnetization of FM. The ultrafast demagnetization of FM generates spins on FM, this spin diffuses and accumulates on NM.

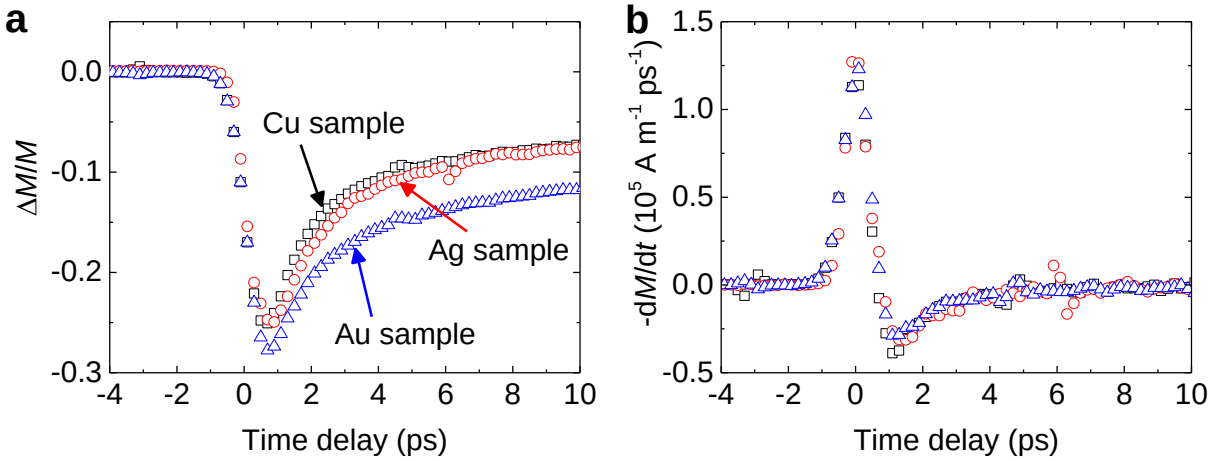

Fig. 4.2: (a) Demagnetization data measured on the Pt side of the Cu-100 (black squares), Ag-100 (red circles), and Au-100 (blue triangles) samples. (b) The -dM/dt of the Cu-100 (black squares), Ag-100 (red circles), and Au-100 (blue triangles) samples. Data are obtained by multiplying the saturation magnetization, 4×10^5 A m^{-1}, with the numerical differentiation of (a) [10].

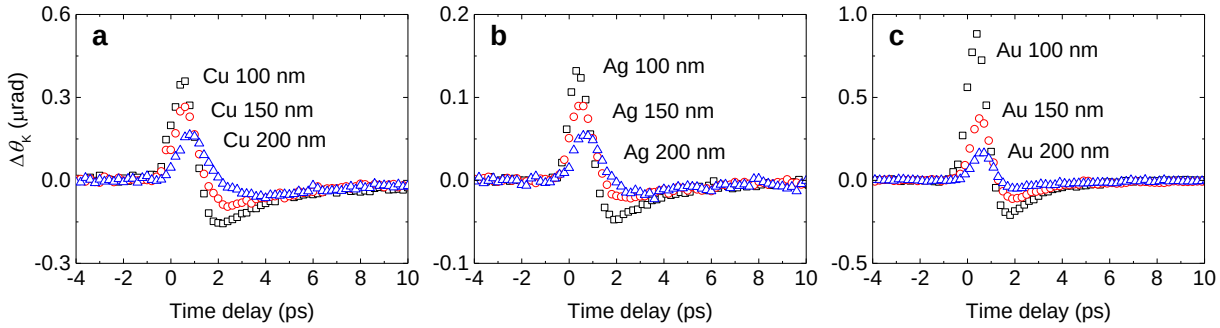

Fig. 4.3: The Kerr rotations measured on the NM side of the (a) Cu-*h*, (b) Ag-*h*, and (c) Au-*h* samples: black squares, red circles, and blue triangles are for NM thickness of 100, 150, and 200 nm, respectively [10].

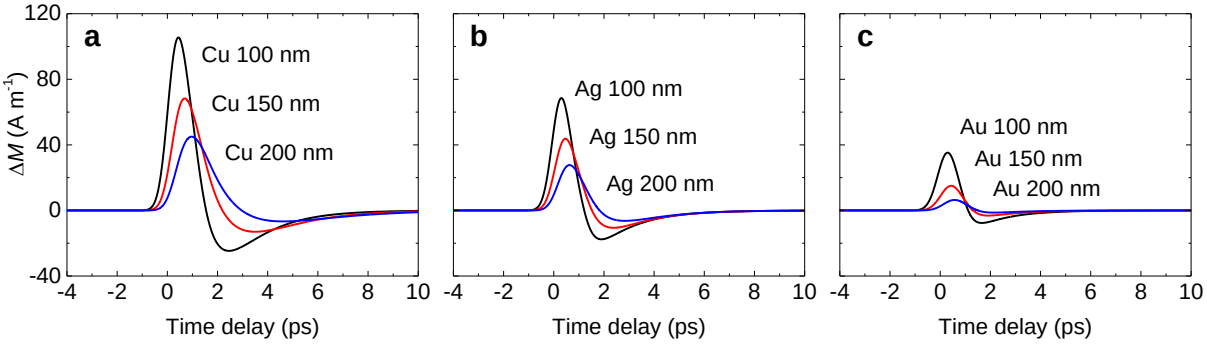

Fig. 4.4: The calculated spin accumulations at the NM surface of the (a) Cu-h, (b) Ag-h, and (c) Au-h samples: black, red, and blue lines are for NM thickness of 100, 150, and 200 nm, respectively [10].

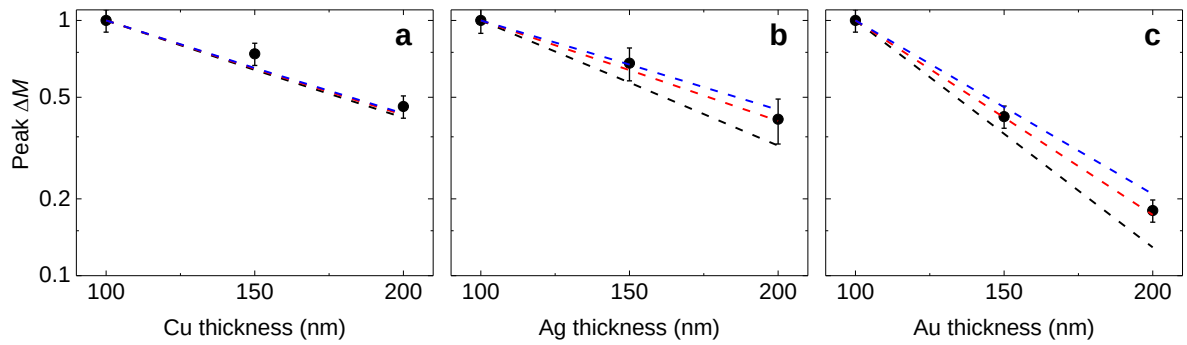

Fig. 4.5: The dependence of the peak spin accumulation on the (a) Cu, (b) Ag, and (c) Au thicknesses. (a) Black circles are experimental data from Fig. 2a and solid lines are from calculation (black, red, blue lines are for l_S of Cu of 300 (τ_S=9 ps), 400 (τ_S=16 ps), and 500 (τ_S=26 ps) nm, respectively). (b) Black circles are experimental data from Fig. 2b; solid lines are from calculation (black, red, blue lines are for l_S of Ag of 100 (τ_S=0.7 ps), 150 (τ_S=1.5 ps), and 200 (τ_S=2.7 ps) nm, respectively). (c) Black circles are experimental data from Fig. 2c; solid lines are from calculation (black, red, blue lines are for l_S of Au of 50 (τ_S=0.3 ps), 60 (τ_S=0.4 ps), and 70 (τ_S=0.5 ps) nm, respectively) [10].

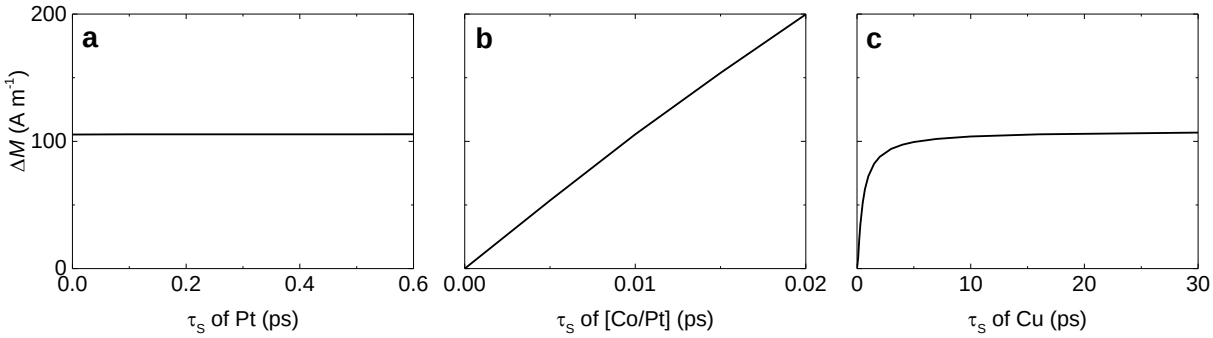

Fig. 4.6: The dependence of the spin accumulation in the spin relaxation time of Pt, [Co/Pt], and Cu in the Pt (20)/ [Co/Pt] (6)/ Cu (100) (unit in nm) structure. (a) The τ_S of Pt is varied from 0 to 0.6 ps while τ_S of [Co/Pt] and Cu are fixed at 0.01 and 16 ps, respectively. (b) The τ_S of [Co/Pt] is varied from 0 to 0.02 ps while τ_S of Pt and Cu are fixed at 0.3 and 16 ps, respectively. (c) The τ_S of Cu is varied from 0 to 30 ps while τ_S of Pt and [Co/Pt] are fixed at 0.3 and 0.01 ps, respectively [10].

Table 4.1: Parameters for the spin diffusion calculation: σ is the in-plane electric conductivity, N_F is the electronic density of states at the Fermi level, D is the diffusion constant, and τ_S is the spin relaxation time.

	Pt	**[Co/Pt]**	**Cu**	**Ag**	**Au**
σ (10^7 Ω^{-1} m^{-1})	0.6[a]	0.2[a]	3.9[a]	3.8 [a]	2.7[a]
N_F (10^{47} J^{-1} m^{-3})	11.48[b]	11.16[b]	1.55[b]	0.99 [b]	1.08[b]
D (10^{-3} m^2 s^{-1})	0.21	0.074	9.8	15	9.8
τ_S (ps)	0.3	0.01	16	1.5	0.4

[a] Obtained from four-point probe measurement.
[b] Obtained from the electronic heat capacity of reference [19].

CHAPTER 5

DEMAGNETIZATION-DRIVEN SPIN TRANSFER TORQUE

Parts of this chapter were published in "Spin current generated by thermally driven ultrafast demagnetization" Gyung-Min Choi, Byoung-Chul Min, Kyung-Jin Lee, and David G. Cahill, Nature Commun. **5**, 4334 (2014).

5.1 Introduction

Spin transfer torque (STT), transfer of the spin angular momentum of conduction electrons to the magnetization of a ferromagnet, enables the manipulation of nanomagnets with spin currents rather than magnetic fields [1, 2]. STT is intensely studied because of its potential for applications in magnetic random access memories, programmable logics, and microwave oscillators. Conventionally, STT has often been realized by passing electrical currents through magnetic layers [3-5].

Recently, Battiato *et al*. suggested that ultrafast demagnetization produces spin-polarized hot electrons which move to an adjacent metallic layer by a so-called "superdiffusive current" [6]. The findings of several subsequent experiments have been interpreted as supporting this hypothesis [7-9]. However, this superdiffusive model is contradict to the thermodynamic description of ultrafast demagnetization, which is based on energy transport among electrons,

magnons, and phonons: three temperature model [10] or microscopic three temperature model [11]. In addition, a quantitative analysis of the demagnetization-driven spin generation has not been reported. To reveal the underlying mechanism for the demagnetization-driven spin generation, more direct and quantitative evidences are required.

In this work, I observe the demagnetization-induced STT using an NM/FM1/NM/FM2 structure where the second magnetic layer FM2 has magnetization that is perpendicular to FM1 [12, 13]. STT on FM2 is well explained by the thermodynamic description: demagnetization-driven spin generation in FM1 and spin diffusion through NM [12]. Comparing the demagnetization of FM1 and STT on FM2, I determine the spin relaxation time of FM1, which is the primary dissipation channel for angular momentum during demagnetization [12].

5.2 Experiment

The concept of how I create STT from demagnetization is shown schematically in Fig. 5.1. The pump laser pulse excites NM1 and leads to the demagnetization of FM1 by thermal transport from NM1 to FM1. The ultrafast demagnetization of FM1 generates a spin current by electron-magnon coupling in FM1, as explained in chapter 4, and the generated spins in FM1 can diffuse through NM2 and lead to STT on FM2.

The sample structure is Pt (30)/ FM1 (6.4)/ Cu (10)/ FM2 (2) (units in nm). FM1 is a ferromagnet with *perpendicular* magnetization ([Co (0.4)/ Pt (1)] $_{\times 4}$/Co (0.2)/ Ni (0.4)/ Co (0.2)) multilayer. This composite ferromagnetic material, [Co/Pt/Co/Ni], has both positive (Co/Pt) and negative (Co/Ni) spin-dependent Seebeck coefficient in one stack (see Chapter 6); this material choice suppressed the spin-dependent Seebeck effect so that the demagnetization-driven spin generation becomes the dominant mechanisom for STT. FM2 is a ferromagnetic CoFeB layer with

in-plane magnetization. This perpendicular configuration of magnetization between FM1 and FM2 is an effective way of observing magnetization dynamics due to STT.

I use time-resolved measurements of the polar magneto-optical Kerr effect (TRMOKE) to detect the transient magnetic signal in the film-normal direction: (i) measure the demagnetization of [Co/Pt/Co/Ni] with the probe beam on the Pt side of the sample; (ii) measure the precession of the CoFeB layer with the probe beam on the CoFeB side of the sample. The wavelengths of the pump and probe pulses are 785 nm, and the full widths at half maximum are ≈0.8 and ≈0.3 ps, respectively. The pump beam is always incident on the Pt side of the samples with a fluence of 10.6 J m^{-2}; the absorbed fluence is 3.7 J m^{-2}.

5.3 Results and discussion

When both pump and probe beams are incident on the Pt side of the sample, I observe a rapid demagnetization of FM1 on a sub-picosecond timescale and partial recovery of the magnetization that is complete after a few picoseconds (Fig. 5.2). By comparing the transient Kerr rotation (ΔM) and static Kerr rotation (M), I determine the peak demagnetization of $\frac{\Delta M}{M}\Big|_{peak} = 0.08 \pm 0.02$ at 0.4 ps and the net demagnetization of $\frac{\Delta M}{M}\Big|_{net} = 0.03 \pm 0.01$ after 3 ps. The former is due to high electron temperature rising of FM1 by fast thermal transport from Pt and subsequent magnon temperature rising by strong electron-magnon coupling of FM1. The latter is due to thermal equilibration among electrons, magnons, and phonons of FM1. As explained in Chapter 4, I assume the demagnetization-driven spin generation rate of $g_S = -\frac{dM}{dt}$.

The demagnetization-induced spin current has a spin component collinear with the [Co/Pt/Co/Ni] magnetization. Therefore, this spin current is transverse to the CoFeB-

magnetization and could efficiently supply STT. The CoFeB layer acts as a spin sink due to a rapid absorption of the transverse spin component within a few atomic layers of a ferromagnet [14]. The absorption of the transverse spin current by the CoFeB layer produces a tilting of its magnetization followed by precession.

The precession of the CoFeB layer appears on top of the smooth background created by the demagnetization and magnetization recovery of the [Co/Pt/Co/Ni] layer (Fig. 5.3). (The Cu layer in this sample is thin, only 10 nm, and therefore the magneto-optic properties of the [Co/Pt/Co/Ni] directly affects the polarization of the probe.) Spin current from the [Co/Pt/Co/Ni] layer tilts the CoFeB-magnetization—which initially lies in-plane—out-of-plane within a few ps; the CoFeB magnetization subsequently precesses. The initial tilting of CoFeB produces a positive Kerr rotation while the demagnetization of [Co/Pt] produces a negative rotation. As the static Kerr rotations of CoFeB and [Co/Pt] are of the same sign, the direction of the initial CoFeB tilting is the same as that of the [Co/Pt] magnetization.

After subtracting the demagnetization signal, the precession signal is well described by a damped sine function whose frequency, 7.4 GHz, and damping constant, 0.02, are can be calculated from the properties of CoFeB,

$$f = \frac{\gamma_e}{2\pi}\sqrt{B_x(B_x + \mu_0 M_S)}, \tag{5.1}$$

$$\alpha^{-1} = \tau_\alpha \gamma_e \left(B_X + \frac{\mu_0 M_S}{2}\right), \tag{5.2}$$

where γ_e=1.76×10^{11} rad s^{-1} T^{-1} is the electron gyromagnetic ratio, B_x=0.045 T is the in-plane magnetic field, μ_0 is the vacuum permeability, M_S=1.2×10^6 A m^{-}1 is the saturation magnetization of CoFeB, and τ_α=400 ps is the decay time. Comparing the oscillation amplitude is 0.45±0.5 µrad with the static Kerr rotation, 240±50 µrad, of the full magnetization of the CoFeB layer, the oscillation amplitude corresponds to $\frac{\Delta M_Z}{M} = 2 \pm 0.6 \times 10^{-3}$.

I compare the spin gain of the CoFeB layer and the spin loss of the [Co/Pt/CoNi] layer. For the CoFeB layer, the calculate the spin gain as 4.8×10^{-6} A by multiplying M_S (1.2×10^{6} A m^{-1}), thickness (2×10^{-9} m), and $\frac{\Delta M_Z}{M} = 2 \times 10^{-3}$. For the [Co/Pt/Co/Ni] layer, the spin loss by demagnetization is 7.8×10^{-5} A is calculated in the same manner by multiplying M_S (4×10^{5} A m^{-1}), thickness (6.4×10^{-9} m), and $\frac{\Delta M}{M}\Big|_{net} = 0.03$. Thus, only 6 % of the spin loss of the [Co/Pt] layer is converted to STT on the CoFeB layer.

For a more quantitative estimate of the spin transfer, I solve the spin diffusion equation [15] for the four-layer Pt/[Co/Pt/Co/Ni]/Cu/CoFeB structure.

$$\frac{\partial \mu_S}{\partial t} = D\frac{\partial^2 \mu_S}{\partial^2 z} - \frac{\mu_S}{\tau_S} + \left(\frac{g_S}{N_S}\right), \tag{5.3}$$

where set the demagnetization-driven spin generation rate of $g_S = -\frac{dM}{dt}$ at the FM1. I set $\mu_S = 0$ in the CoFeB layer as the CoFeB layer acts as a spin sink. I use the same diffusion constant and relaxation time of each layer as described in chapter 4 except the spin relaxation time of [Co/Pt/Co/Ni], which is the free parameter for matching STT experiment with spin diffusion modeling.

I also include finite spin conductances at normal metal-ferromagnet interfaces [16, 17] because the interfacial spin conductance becomes dominant over the bulk diffusivity at thin Cu thickness. For the longitudinal component, the spin conductance is $\frac{G_\uparrow + G_\downarrow}{2e^2}$, and for the transverse component the spin conductance is $\frac{\mathrm{Re}\{G_{\uparrow\downarrow}\}}{e^2}$, where $G_{\uparrow,\downarrow}$ is the conductance of the spin up/down and $G_{\uparrow\downarrow}$ is the spin mixing conductance [16]. The electrical conductance, $G_\uparrow + G_\downarrow$, at the Co/Cu interface has been reported to 0.75×10^{15} Ω^{-1} m^{-2} from theoretical calculation [17] and 2×10^{15} Ω^{-1} m^{-2} from experimental measurement [18]. Since each Co layer is very thin, I expect adjacent layers,

Pt or Ni, also affect the electrical conductance of the Co/Cu interface; experimentally measured electrical conductances are 1.3, 5.6, and 1.2×10^{15} Ω^{-1} m^{-2} for Pt/Cu [19], Ni/Cu [20], and Co/Pt [21] interfaces, respectively. Considering these values, I use electrical conductances of 1.5 and 3×10^{15} Ω^{-1} m^{-2} for Pt/[Co/Pt/Co/Ni] and [Co/Pt/Co/Ni]/Cu interfaces, respectively. For the Cu/CoFeB interface, I use the transverse spin conductance because the spin in Cu is transverse with the CoFeB magnetization. For the spin mixing conductance, $G_{\uparrow\downarrow}$, I take the theoretically calculated value, 0.56×10^{15} Ω^{-1} m^{-2}, of the Co/Cu interface [17].

Solving the spin diffusion equation, one can obtain the spin current, J_S, which is absorbed by FM2 (Fig. 5.4 (a)). Given the spin generation rate, -dM/dt, at FM1, the amount of J_S to FM2 is determined by τ_S of FM1: a longer τ_S produces a larger J_S. I determine τ_S of [Co/Pt/Co/Ni] to be 0.02 ps from comparing dM/dt of [Co/Pt/Co/Ni] and the amplitude of precession of CoFeB. Using the obtained J_S as an input, I perform magnetization dynamics simulation for CoFeB with the Landau-Lifshitz-Gilbert equation incorporating STT [22-24],

$$\dot{\mathbf{m}} = -\gamma_e \mathbf{m} \times \mathbf{H}_{\text{eff}} + \alpha \mathbf{m} \times \dot{\mathbf{m}} + \frac{J_S}{M_S h} \mathbf{m} \times (\mathbf{m} \times \mathbf{m}_{\text{fixed}}), \quad (5.4)$$

where $\mathbf{m}$ and $\mathbf{m}_{\text{fiexd}}$ are unit vectors in the direction of the CoFeB and [Co/Pt/Co/Ni] magnetizations, $\dot{\mathbf{m}}$ is the time derivative of $\mathbf{m}$, M_S and h are the saturation magnetization and thickness of the CoFeB layer, $\mathbf{H}_{\text{eff}}$ is the effective field due to applied field of 0.045 T and shape anisotropy of 1.5 T of CoFeB, γ_e is the gyromagnetic ratio, α is the Gilbert damping constant, and J_S is the spin current. The simulation result is in good agreement with the precession data (Fig. 5.4 (b)).

I also find that the τ_S of FM1 depends on its composition (Fig. 5.5). At the same demagnetization, the spin accumulation in Cu of the Pt/FM1/Cu structure is two times smaller with [Co/Pt] ($[Co(0.4)/Pt(1)]_{x4}$/Co(0.4) made at UIUC) as FM1 than with [Co/Pt/Co/Ni] (made at KIST)

as FM1. Therefore, I determine τ_S of [Co/Pt], used in chapter 4, to be 0.01 ps. The spin accumulation increases with reducing the repetition number (n) of [Co(0.4)/Pt(1)]×n/Co(0.4). Since the amount of demagnetization is nearly the same, the increase in spin accumulation suggests that τ_S of [Co/Pt] increases with a smaller repetition number.

The τ_S of FM1 can be estimated from $\tau_s = \frac{\tau_0}{a_{sf}}$, where τ_0 is the momentum relaxation time, and a_{sf} is the spin-flip probability from theory of Elliot-Yafet [25, 26]. The τ_0 of [Co/Pt/Co/Ni] is calculated to be 5 fs using $\tau_0 = \frac{3D}{v_F^2}$, where D is the diffusivity, and v_F is the Fermi velocity; v_F=0.24×10^6 m sec^{-1} for Pt [111] direction [27]. The a_{sf} of typical ferromagnetic transition metals is 0.1~0.2 [11]. When I use a_{sf}=0.1 and τ_0=5 fs; the τ_S of [Co/Pt] is then 0.05 ps, which has a reasonable agreement with our finding of 0.02 ps. Another explanation for τ_S of FM1 is the spin flipping at the Co/Pt interface. Recently, the interface spin-flipping parameter, δ, at the Co/Pt interface was reported to be $0.9^{+0.5}_{-0.2}$, which leads to the spin-flipping probability of $0.6^{+0.2}_{-0.1}$ at the interface by $P = 1 - \exp(-\delta)$ [28].

5.4 Conclusion

I have shown that demagnetization of FM1 can generate STT on FM2. For the modeling, I assume two important physics: first, demagnetization of FM1 fully converts its spin loss to spin generation in electrons of FM1; second, the amount of STT is determined by the relative speed of spin diffusion from FM1 to FM2 and local spin relaxation in FM1 (Fig. 5.6). Due to its short time scale, the spin relaxation time of FM1 becomes the primary dissipation channel for angular momentum of FM1 during demagnetization. I expect a ferromagnet with a long spin relaxation time can produce much larger STT. One distinct advantage of the demagnetization-driven STT is

its fast time scale, an order of one picosecond, which is extremely challenging to achieve with the electrical spin generation.

5.5 References

1. J. C. Slonczewski, J. Magn. Magn. Mater. **159**, L1 (1996).
2. L. Berger, Phys. Rev. B **54**, 9353 (1996).
3. M. Tsoi, A. G. M. Jansen, J. Bass, W.-C. Chiang, M. Seck, V. Tsoi, and P. Wyder, Phys. Rev. Lett. **80**, 4281 (1998).
4. E. B. Myers, D. C. Ralph, J. A. Katine, R. N. Louie, and R. A. Buhrman, Science **285**, 867 (1999).
5. J. A. Katine, F. J. Albert, R. A. Buhrman, E. B. Myers, and D. C. Ralph, Phys. Rev. Lett. **84**, 3149 (2000).
6. M. Battiato, K. Carva, and P. M. Oppeneer, Phys. Rev. Lett. **105**, 027203 (2010).
7. G. Malinowski, F. Dalla Longa, J. H. H. Rietjens, P. V. Paluskar, R. Huijink, H. J. M. Swagten, and B. Koopmans, Nature Phys. **4**, 855 (2008).
8. A. Melnikov, I. Razdolski, T. O. Wehling, E. Th. Papaioannou, V. Roddatis, P. Fumagalli, O. Aktsipetrov, A. I. Lichtenstein, and U. Bovensienpen, Phys. Rev. Lett. **107**, 076601 (2011).
9. D. Rudolf, C. La-O-Vorakiat, M. Battiato, R. Adam, J. M. Shaw, E. Turgut, P. Maldonado, S. Mathias, P. Grychtol, H. T. Nembach, T. J. Silva, M. Aeschlimann, H. C. Kapteyn, M. M. Murnane, C. M. Schneider, and P. M. Oppeneer, Nature Commun. **3**, 1037 (2012).
10. E. Beaurepaire, J.-C. Merle, A. Daunois, and J.-Y. Bigot, Phys. Rev. Lett. **76**, 4250 (1996).

11. B. Koopmans, G. Malinowski, F. Dalla Longa, D. Steiauf, M. Fähnle, T. Roth, M. Cinchetti, and M. Aeschlimann, Nature Mater. **9**, 259 (2010).

12. G.-M. Choi, B.-C. Min, K.-J. Lee, and D. G. Cahill, Nature Commun. **5**, 4334 (2014).

13. A. J. Schellekens, K. C. Kuiper, R. R. J. C. de Wit, and B. Koopmans, Nature Commun. **5**, 4333 (2014).

14. M. D. Stiles and A. Zangwill, Phys. Rev. B **66**, 014407 (2002).

15. T. Valet and A. Fert, Phys. Rev. B **48**, 7099 (1993).

16. J. Barnaś, A. Fert, M. Gmitra, I. Weymann, and V. K. Dugaev, Phys. Rev. B **72**, 024426 (2005).

17. M. Zwierzycki, Y. Tserkovnyak, P. J. Kelly, A. Brataas, and G. E. W. Bauer, Phys. Rev. B **71**, 064420 (2005).

18. J. Bass and W. P. Pratt Jr., J. Magn. Magn. Mater. **200**, 274-289 (1999).

19. H, Kurt, R. Loloee, K. Eid, W. P. Pratt Jr., and J. Bass, Appl. Phys. Lett. **81**, 4787 (2002).

20. C. E. Moreau, I. C. Moraru, N. O. Birge, and W. P. Pratt Jr., Appl. Phys. Lett. **90**, 012101 (2007).

21. A. Sharma, J. A. Romero, N. Theodoropoulou, R. Loloee, W. P. Pratt Jr., and J. Bass, J. Appl. Phys. **102**, 113916 (2007).

22. L. Landau, and E. Lifshitz, Phys. Z. Sowietunion, **8**, 153 (1935).

23. T. L. Gilbert, IEEE Trans. Magn. **40**, 3443 (2004).

24. J. C. Slonczewski, J. Magn. Magn. Mater. **247**, 324 (2002).

25. R. J. Elliot, Phys. Rev. **96**, 266 (1954).

26. Y. Yafet, *Solid State Physics* Vol. 14 (Academic, 1963).

27. D. H. Dye, J. B. Ketterson, and G. W. Crabtree, J. Low Temp. Phys. **30**, 813 (1978).

28. H. Y. T. Nguyen, W. P. Pratt Jr., and J. Bass, J. Magn. Magn. Mater. **361**, 30 (2014).

5.6 Figures

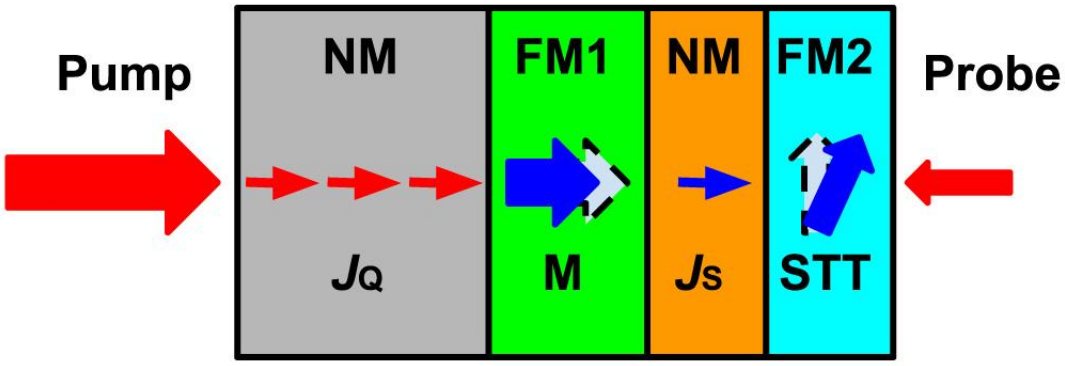

Fig. 5.1: Conceptual diagram. Pump laser is incident on NM1 and creates an ultrafast temperature excursion. Thermal transport from NM1 to FM1 drives demagnetization. The demagnetization of FM1 generates spins, and this spin diffuses through NM2 and absorbed by FM2. The absorbed spin results in STT on FM2 [12].

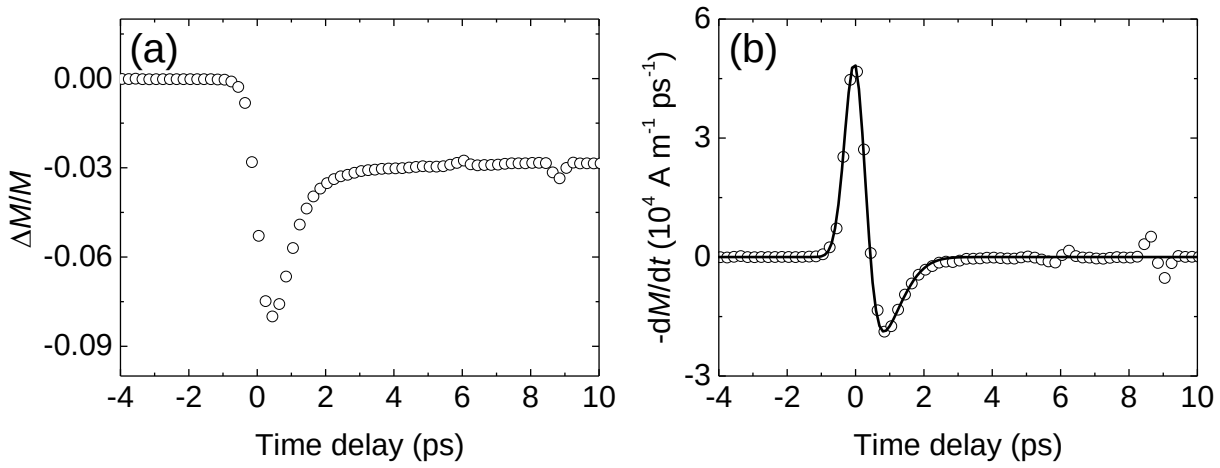

Fig. 5.2: (a) Demagnetization data measured on the Pt side of the sample. (b) The -dM/dt of the sample obtained by multiplying the saturation magnetization, 4×10^5 A m^{-1}, with the numerical differentiation of (a) [12].

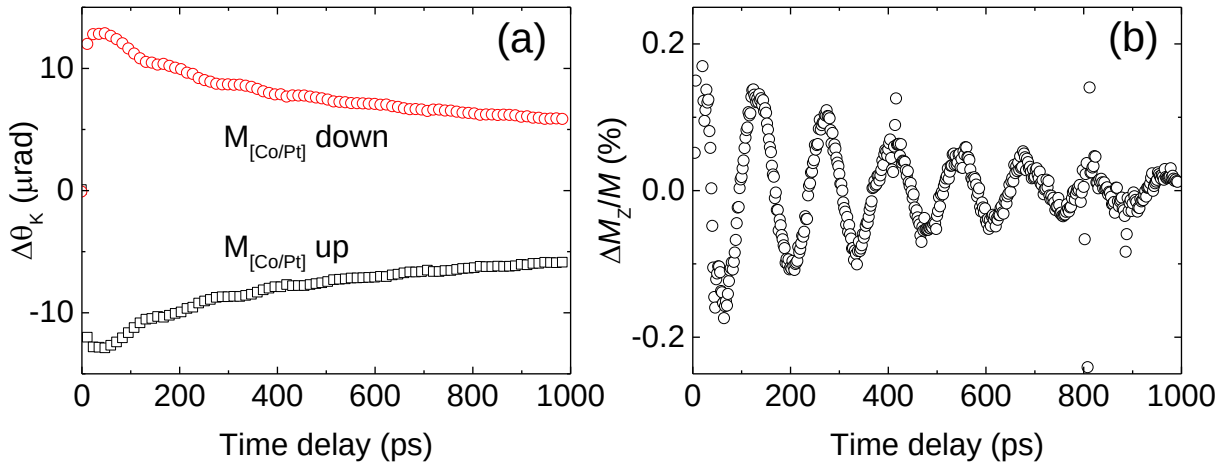

Fig. 5.3: Spin transfer torque on the CoFeB layer. (a) Kerr rotation of the CoFeB side of the sample with the [Co/Pt/Co/Ni] magnetization up (black square) or down (red circle). (b) The precession data (black circle) is obtained by subtracting the demagnetization signal of (a) [12].

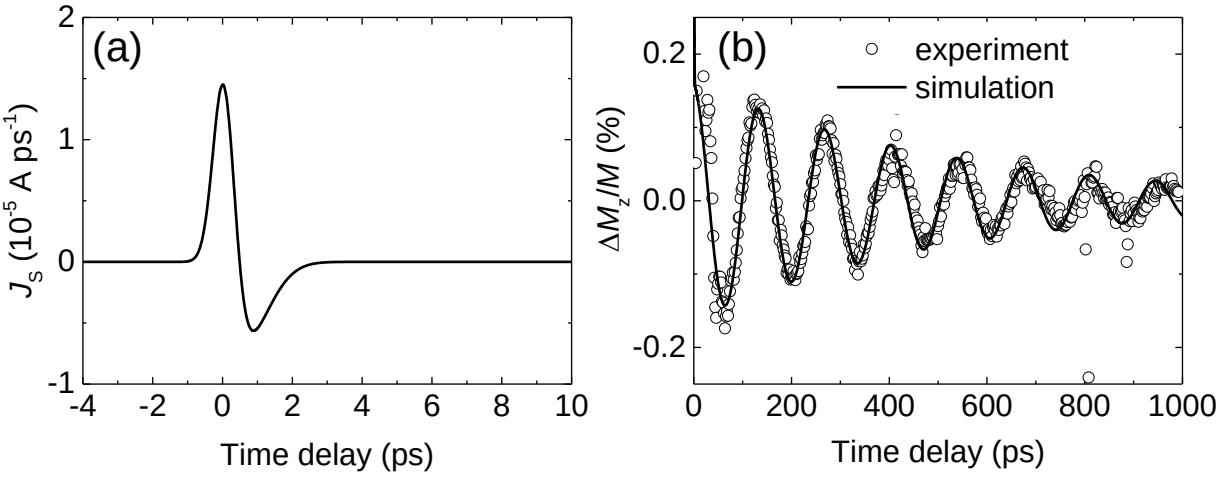

Fig. 5.4: Spin transfer torque on the CoFeB layer. (a) The calculated spin current that goes to CoFeB by demagnetization of [Co/Pt/Co/Ni], whose spin relaxation is set to 0.02 ps. (b) The precession data (black circles) and magnetization dynamics simulation (solid line). The simulation is done by Landau-Lifshitz-Gilbert equation with an input spin current of (a) [12].

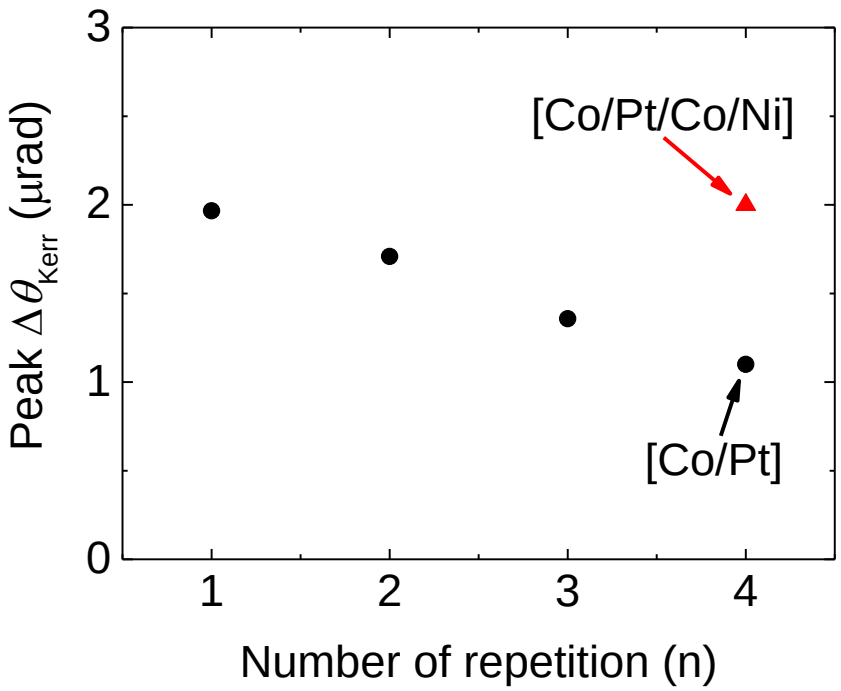

Fig. 5.5: The peak Kerr rotation in Cu by spin accumulation in the Pt(30)/FM/Cu(100) structure: black circles is with [Co(0.4)/Pt(1)]xn/Co(0.4) made at UIUC; red triangle is with [Co(0.4)/Pt(1)]x4/Co(0.2)/Ni(0.4)/Co(0.2) made at KIST.

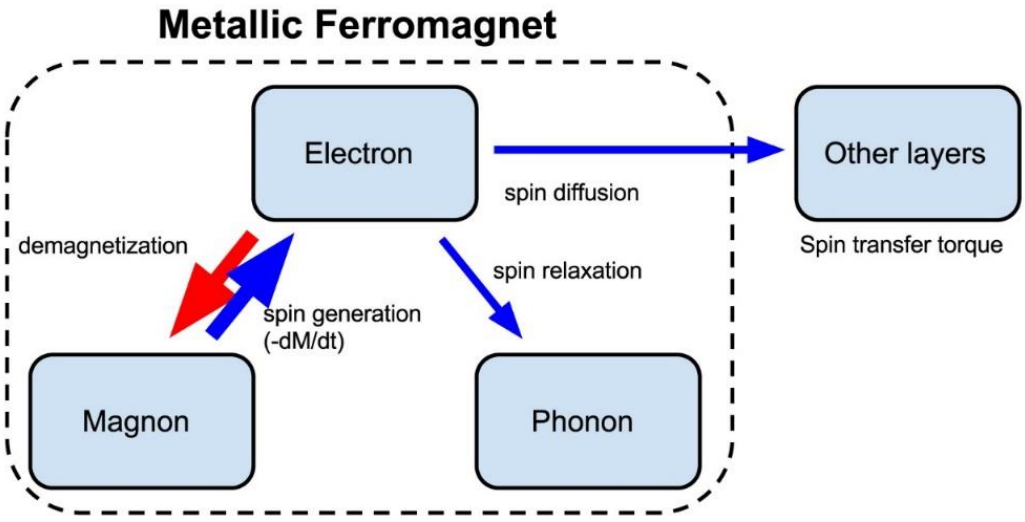

Fig. 5.6: Schematic illustration of mechanisms of the demagnetization-driven STT. Electron-magnon coupling of FM converts spin loss in magnons to spin gain in electrons of FM. The generated spins in FM can diffuse to other layer and lead to STT. Given the demagnetization, the amount of STT depends on the relative speed of spin diffusion and spin relaxation.

CHAPTER 6

SDSE-DRIVEN SPIN TRANSFER TORQUE

Parts of this chapter will be published in "Thermal spin transfer torque driven by spin-dependent Seebeck effect in metallic spin-valve structures" Gyung-Min Choi, Chul-Hyun Moon, Byoung-Chul Min, Kyung-Jin Lee, and David G. Cahill, Nature Phys. accepted.

6.1 Introduction

The coupling of spin and heat gives rise to new physical phenomena in nanoscale spin devices. In particular, spin transfer torque (STT) driven by passing heat currents through magnetic layers provides a new way to manipulate local magnetization. Hatami *et al*. theoretically predicted thermally-driven STT in metallic spin valves [1]; Slonczewski suggested the initiation of thermally-driven STT in ferrite/metal structures and predicted a greatly enhanced quantum efficiency compared to charge-current-driven STT [2]. These new phenomena, namely, "thermal STT" rely on the transport of thermal energy, in contrast to the transport of electrical charge, and provide a new way to manipulate magnetization [1, 2].

To fully realize the envisioned advantages of thermal STT, it is important to observe thermal STT directly and quantify its sign and magnitude. Although thermal spin injection in ferromagnetic metal (FM)/normal metal (NM) [3], ferrite/NM [4], and FM/semiconductor [5] has been achieved, direct and conclusive evidence of thermal STT has remained elusive [6, 7]. Yu *et*

al. observed a change in the switching field of a Co/Cu/Co nanowire with application of a heat current and interpreted the second harmonic voltage response of the nanowire as evidence of thermal STT [6]. Their interpretation is controversial, since, in order to explain their data with a small heat current of ~1 MW m^{-2}, the authors had to assume a Seebeck coefficient that is three orders of magnitude larger than the typical Seebeck coefficient of metals. Flipse *et al.* attempted to identify thermal STT in current-driven magnetization switching but found that the signal is dominated by overall heating of the magnetic layer [7].

6.2 Experiment

Here I provide direct evidence of thermal STT in metallic spin valves with the structure Pt/FM1/Cu/FM2 (Fig. 6.1) [8]. Heating by the ultra-fast pump optical pulse generates spin currents in the structure by two distinct mechanisms: i) volume spin generation in the FM1 layer by ultrafast heating and associated ultrafast demagnetization of FM1; ii) interfacial spin generation at the Pt/FM1 and FM1/Cu interfaces by heat current passing through the FM1 layer. The spin-dependent Seebeck effect (SDSE) of FM1 converts the heat current into spin current, which in turn exerts STT on FM2.

The demagnetization-driven spin generation is due to temperature imbalance between electrons and magnons of FM1, and its rate (g_S) is the negative of the time derivative of demagnetization (dM/dt) [9, 10]. The explanation $g_S = -\frac{dM}{dt}$ is shown on chapter 4 and 5. The demagnetization-driven spin generation is significant for only the first ~3 ps after the pump optical pulse; 3 ps is approximately the time required for electrons, magnons, and phonons of FM1 to equilibrate.

The main focus of our work is the SDSE-driven spin generation and corresponding thermal STT. In contrast to ultrafast demagnetization, the heat current passing through FM1 persists for a much longer time, ~100 ps, the time required for the various layers in the structure (Pt, FM1, Cu, and FM2) to equilibrate. The SDSE of FM1 converts this heat current to interfacial spin generation [1, 3]. The generated spin diffuses through the non-magnetic Cu layer and exerts STT on FM2. Selection of the FM1 material provides control of the sign and magnitude of thermal STT. I find that [Co/Pt] multilayers have a positive spin-dependent Seebeck coefficient (S_S) whereas [Co/Ni] multilayers have a negative S_S. In addition, the amount of thermal STT can be controlled by the thickness of Cu, which acts a heat sink layer.

The sample structure has two types. The first type of sample structure is used for measurements of spin accumulation and consists of Pt (20)/ [Co/Pt] or [Co/Ni] (3.2)/ Cu (100) (units in nm) (I refer to this as the [Co/Pt]/Cu-100 or [Co/Ni]/Cu-100 sample); the second type of sample structure is used for measurements of STT and consists of Pt (20)/ [Co/Pt] or [Co/Ni] (3.2)/ Cu (*h*)/ CoFeB (2) (I refer to this as the [Co/Pt]/Cu-*h*/CoFeB or [Co/Ni]/Cu-*h*/CoFeB sample). The thickness of Cu, *h*, is 10 or 100 nm. I note that the magnetization of the [Co/Pt] or [Co/Ni] layer is perpendicular to the film plane, whereas the magnetization of the CoFeB layer is in the plane. The [Co/Pt] and [Co/Ni] layers consist of [Co (0.2)/ Pt (0.4)]$_{\times 5}$/ Co (0.2) and [Co (0.2)/ Ni (0.4)]$_{\times 5}$/ Co (0.2), respectively. All samples are prepared using a seven-target sputter deposition system with a base pressure of $<5\times10^{-8}$ Torr at the Korea Institute of Science and Technology. Additional MgO (10)/ Al_2O_3 (5) layers are deposited to protect the Cu or CoFeB layer from oxidation.

The magnetic properties of the perpendicularly magnetized [Co/Pt] and [Co/Ni] layers is characterized with a vibrating sample magnetometer (VSM): the saturation magnetizations are 4.2 and 5.9×10^{5} A m^{-1}, respectively; the coercivities are 340 and 200 mT, respectively, and the

remanence is close to unity for both. Electric conductivities of the Pt, [Co/Pt], [Co/Ni], and Cu layers are measured using a four-point probe with separately prepared samples (sapphire/ Pt (20), sapphire/ Pt (2)/ [Co (0.2)/ Pt (0.4)]$_{\times 30}$/ Pt (2), sapphire/ Ni (2)/ [Co (0.2)/ Ni (0.4)]$_{\times 30}$/ Pt (2), and sapphire/ Cu (100)) and are summarized on Table 6.1.

I use pump-probe technique to create ultrafast heat current and measure spin and temperature responses on sub-picosecond timescales: for temperature measurements, I use time-domain thermoreflectance (TDTR); for spin measurements, I use time-resolved magneto-optical Kerr effect (TR-MOKE). The wavelengths of the pump and probe pulses are 785 nm, and the full widths at half maximum are ≈0.8 and ≈0.3 ps, respectively. The pump beam is always incident on the Pt side of the samples with a fluence of 10.6 J m^{-2}; the absorbed fluence is 3.7 J m^{-2}.

6.3 Results and discussion

For the demagnetization-driven spin generation, I obtain dM/dt from the time derivative of measured $M(t)$. I measure demagnetization of [Co/Pt] and [Co/Ni] with both pump and probe beams incident on the Pt side of samples (Fig. 6.2 (a)). By comparing the transient Kerr rotation (ΔM) and static Kerr rotation (M), I determine the peak $\Delta M/M$: 0.26±0.04 and 0.23±0.04, respectively, for [Co/Pt]/Cu-10/CoFeB and [Co/Pt]/Cu-100/CoFeB samples; 0.08±0.01 and 0.07±0.01, respectively, for [Co/Ni]/Cu-10/CoFeB and [Co/Ni]/Cu-100/CoFeB samples. A change in the thickness of the Cu heat sink layer from 10 nm to 100 nm only slightly reduces the demagnetization because the peak demagnetization, which is proportional to the peak magnon temperature, is mostly controlled by the thickness of the heat absorbing layer, Pt, not by the thickness of the heat sink layer, Cu. The difference in $\Delta M/M$ between [Co/Pt] and [Co/Ni] originates from the different Curie temperatures (Fig. 6.2 (b)). When the excursion in the magnon

temperature is 100 K above room temperature (Fig. 6.3), $\Delta M/M$ is 0.22 and 0.08 for [Co/Pt] and [Co/Ni], respectively (Fig. 6.2 (b)). The $\Delta M/M$ and saturation magnetization of 4.2 and 5.9×10^5 A m^{-1} for [Co/Pt] and [Co/Ni], respectively, lead to a spin generation term g_S that is two times larger using [Co/Pt] as FM1 than with [Co/Ni].

For the SDSE-driven spin generation, a transient heat current is created by illuminating the Pt layer with an ultrashort laser pulse. I measure the temperature of each layer and model the thermal transport from numerical simulation using a finite difference method (Fig. 6.3). The temperature evolution of each layer is determined by parameters of heat capacity, thermal conductivity, and electron-phonon coupling (I find the interfacial thermal conductances of reasonable range does not affect thermal transport) (see Table 6.1). In the models, I distribute the initial absorption of energy from the pump optical pulse by the Pt electrons over an exponential decay length of 20 nm. The length-scale of 20 nm is intended to model the combined effects of the optical absorption length (11 nm) and a ballistic motion Pt electrons before thermalization. A complete description of thermal modeling is given in the Ref. [11].

In the thermal modeling shown in Fig. 6.3, the free parameters are the electron-phonon coupling parameters, $g_{e\text{-}p}$, of Pt and Cu. I determine $g_{e\text{-}p}$ of Pt to be 4.2×10^{17} W m^{-3} K^{-1} from the temperature rise of Cu phonon at ≈1 ps, which is due to fast electronic heat transport during the pump optical pulse. Previously reported values for Pt are 2.5 and 11×10^{17} W m^{-3} K^{-1} [12, 13]. After electron-phonon thermalization within the Pt layer, the evolution of temperature of each layer is determined by the thermal conductivity of each layer and $g_{e\text{-}p}$ of Cu. Because of relatively large thickness and small $g_{e\text{-}p}$ of Cu, $g_{e\text{-}p}$ of Cu is a dominant factor to determine thermalization time between Pt phonons and Cu phonons. I determine $g_{e\text{-}p}$ of Cu from temperature responses of Pt and

Cu at 10~200 ps and find $g_{e\text{-}p}=7\times10^{16}$ W m^{-3} K^{-1}, within experimental uncertainties of the previously reported value of 7.5×10^{16} W m^{-3} K^{-1} [14].

By analyzing the time evolution of the temperature of each layer (Figs. 6.3), I determine the heat current passing through the [Co/Ni] layer. The heat current shows two characteristic features (Fig. 6.4): i) a sharply peaked component that essentially follows the time-evolution of the pump optical pulse; and ii) a slowly decaying component. The heat current during the pump optical pulse reaches ≈700 GW m^{-2} at ≈0.3 ps for the Cu-100 nm samples. After two ps, the heat current falls to <100 GW m^{-2} and then decays exponentially with a relaxation time of ≈30 ps. The estimated heat current passing through the [Co/Ni] layer is in good agreement—because of the small thickness of the [Co/Ni] layer—with the measured heat current leaving the Pt layer, $J_{\mathrm{Q}} = -\frac{dT_{\mathrm{Pt}}}{dt} C_{\mathrm{Pt}} h_{\mathrm{Pt}}$ (Fig. 6.4 (b)), where T_{Pt}, C_{Pt}, and h_{Pt} are temperature, heat capacity, and thickness of the Pt layer, respectively.

The heat current, J_{Q}, through FM1 in the Pt/FM1/Cu structure can be estimated by assuming that the initial energy from the pump optical pulse is confined to Pt and J_{Q} has a functional form of exponential decay, $J_{\mathrm{Q}} = J_0 \exp(-t/\tau)$. (The effect of FM2 on heat transfer through FM1 can be ignored since its thickness is much smaller than the other layers.) Pt acts as a heat absorbing layer and Cu acts as a heat sink layer. The total energy transferred from Pt to Cu, i.e., the time integral of J_{Q}, is determined by the relative thicknesses of the Cu and Pt layers,

$$\int_0^\infty J_0\, e^{-t/\tau}\, dt = E_{\mathrm{abs}} \frac{C_{\mathrm{Cu}} h_{\mathrm{Cu}}}{C_{\mathrm{Pt}} h_{\mathrm{Pt}} + C_{\mathrm{Cu}} h_{\mathrm{Cu}}}, \tag{6.1}$$

where τ is the relaxation time, E_{abs} is the energy fluence absorbed by Pt, C_{Pt} is the heat capacity of Pt, C_{Cu} is the heat capacity of Cu, h_{Pt} is the thickness of Pt, and h_{Cu} is the thickness of Cu. Solving this equation leads to the expression for the heat current,

$$J_{\mathrm{Q}} = \frac{E_{abs}}{\tau} \times \frac{C_{\mathrm{Cu}} h_{\mathrm{Cu}}}{C_{\mathrm{Pt}} h_{\mathrm{Pt}} + C_{\mathrm{Cu}} h_{\mathrm{Cu}}} \times e^{-t/\tau}. \tag{6.2}$$

The relaxation time, τ, is determined by the heat capacities, thicknesses, and thermal resistances of the multilayer structure. The dominant thermal resistance is different for Pt and Cu because of their large difference in the electron-phonon coupling: the major thermal resistance of Pt is h/Λ, where Λ is the electronic thermal conductivity; the major thermal resistance of Cu is $1/(gh)$, where g is the electron-phonon coupling parameter. Then, τ can be approximated by,

$$\tau \approx \left(\frac{1}{C_{\mathrm{Pt}} h_{\mathrm{Pt}}} + \frac{1}{C_{\mathrm{Cu}} h_{\mathrm{Cu}}}\right)^{-1} \times \left(\frac{h_{\mathrm{Pt}}}{\Lambda_{\mathrm{Pt}}} + \frac{h_{\mathrm{FM1}}}{\Lambda_{\mathrm{FM1}}} + \frac{1}{g_{\mathrm{Cu}} h_{\mathrm{Cu}}}\right). \tag{6.3}$$

In the Pt (20 nm)/ FM1 (3.2 nm)/ Cu (h nm) structure, this equation leads to τ of ≈30 and ≈40 ps with h_{Cu} of 100 and 10 nm, respectively. (Parameters for heat capacity, thermal conductivity, and electron-phonon coupling are summarized in Table 6.1). Applying these values for τ, $J_Q \approx 100\, e^{-t/(30\ \mathrm{ps})}$ GW m^{-2} with Cu 100 nm and $J_Q \approx 35\, e^{-t/(40\ \mathrm{ps})}$ GW m^{-2} with Cu 10 nm. Despite the simplicity, this estimation of J_{Q} agrees well with the numerical simulation using a finite difference method shown in Fig. 6.4.

The SDSE in the FM1 layer converts the heat current into a spin generation. The spin generation rate at the FM1/Cu interface is given by [3],

$$G_S = -\left(\frac{\mu_{\mathrm{B}}}{e}\right)\left(\frac{S_{\mathrm{S}}}{LT}\right) J_{\mathrm{Q}}, \tag{6.4}$$

where μ_{B} is the Bohr magneton, e is the elementary charge, $S_{\mathrm{S}} = \frac{1-P^2}{2}(S_{\uparrow} - S_{\downarrow})$ is the effective spin-dependent Seebeck coefficient, where $P = \frac{\sigma_{\uparrow} - \sigma_{\downarrow}}{\sigma_{\uparrow} + \sigma_{\downarrow}}$, $\sigma_{\uparrow,\downarrow}$ is the electric conductivity of spin up/down, and $S_{\uparrow,\downarrow}$ is the Seebeck coefficient of spin up/down, L is the Lorenz number, 2.45×10^{8} W Ω K^{-2}, T is the temperature of FM1, and J_{Q} is the heat current flowing through FM1 (the sign of G_{S} is opposite for the Pt/FM1 interface).

The spin generated in the [Co/Pt] or [Co/Ni] layer diffuses into the Cu layer and leads to a spin accumulation, which is observed as Kerr rotation probed at the Cu side of the [Co/Pt]/Cu-100 and [Co/Ni]/Cu-100 samples (Fig. 6.5 (a)). The spin accumulation in the Cu layer consists of two distinct components: i) a component driven by demagnetization and ii) a component driven by SDSE. The demagnetization-driven spin generation ($g_S = -dM/dt$) of [Co/Pt] and [Co/Ni], obtained from experimental demagnetization data, has positive and negative peaks at 0 and ~1 ps, respectively, and decays to zero within error range after ~3 ps (Fig. 6.5 (b)). Although magnetization continues to increase as T_m decreases until > 100 ps (Fig. 6.3), the rate of change in M is so slow after 3 ps that dM/dt becomes negligible at t>3 ps.

In addition to the short time response, and critical for the discussion that follows, I observe that the Kerr signal has a vertical offset at ten ps. The offset is negative for [Co/Pt] and positive for [Co/Ni] (inset of Fig. 6.5 (a)). The offset at 10 ps indicates that there is a spin generation mechanism on relatively long timescales which has an opposite sign for [Co/Pt] and [Co/Ni].

An unequivocal demonstration of thermal STT requires evidence of torque exerted on FM2. I demonstrate thermal STT through the magnetization dynamics of a CoFeB layer separated from the [Co/Pt] or [Co/Ni] layer by a Cu layer. Because spin currents from the [Co/Pt] or [Co/Ni] layer have a polarization that is transverse to the CoFeB magnetization, the CoFeB layer absorbs the spin current within a few atomic layers [15]. The absorbed spin current produces STT and triggers precession of the CoFeB magnetization. Although the SDSE produces just a small offset in spin accumulation, its effect on the CoFeB dynamics can be significant because it lasts much longer (~100 ps) than dM/dt (~3 ps).

I measure the CoFeB precession by probing on the CoFeB side of the [Co/Pt] or [Co/Ni]/Cu-10 or Cu-100/CoFeB sample with an in-plane magnetic field of 0.05 T. Normalizing

the signal with the static Kerr rotation, I obtain the relative precession amplitude ($\Delta M/M$) of CoFeB in the out-of-plane direction. (For Cu 10 nm, the CoFeB precession appears on top of the demagnetization of [Co/Pt] or [Co/Ni] because the thin Cu layer is not optically opaque. I subtract this demagnetization signal to obtain the CoFeB precession signal.)

The amplitude of the CoFeB precession are substantially different with [Co/Pt] and [Co/Ni] (Figs. 6.6 (a) and (b)): the amplitude of the precession signal is approximately five (with Cu 10 nm) and three (with Cu 100 nm) times larger with [Co/Ni] than with [Co/Pt]. Since the peak spin accumulation at ~0.5 ps with [Co/Ni] is only twice as large as that with [Co/Pt] (Fig. 6.5 (a)), this much larger difference in the precession amplitude indicates that the SDSE-driven spin generation produces a significant STT.

More direct evidence of the SDSE-driven STT can be found in the initial slope of the CoFeB magnetization dynamics (Fig. 6.7 (a)). Both [Co/Pt] and [Co/Ni] produce a sharp +z tilting of the CoFeB magnetization at ≈1 ps as a result of a pulse-like demagnetization-driven STT. After 3 ps, the demagnetization-driven STT is no longer significant and the more persistent SDSE-driven STT produces –z and +z slopes of the CoFeB dynamics with [Co/Pt] and [Co/Ni], respectively. The different slopes at delay times between 3 and 10 ps clearly reveal the different sign of the SDSE-driven STT.

Lastly, the phase of the CoFeB precession depends on the composition of FM1 and the thickness of the Cu heat sink layer (Fig. 6.7 (b)). I define the phase ϕ relative to a damped cosine function of $\cos(2\pi ft+\phi)\exp(-t/\tau)$, where f=7.8 GHz is the precession frequency that is partially determined by the in-plane magnetic field of 0.05 T. Since the pulse-like STT by demagnetization does not create a phase, the positive and negative phases are consequences of the SDSE-driven STT from [Co/Pt] and [Co/Ni], respectively, and approximately proportional to the ratio between

the SDSE-driven STT and demagnetization-driven STT. The phase difference, $\Delta\phi$, between [Co/Pt] and [Co/Ni] of 130° with Cu 100 nm suggests a significant role of the SDSE-driven STT. The $\Delta\phi$ decreases to 60° with Cu 10 nm because the heat current with Cu 10 nm is 2~3 times smaller than with Cu 100 nm (Fig. 6.4), while the Cu thickness has a negligible effect on the demagnetization of FM1 (Fig. 6.2 (a)).

Understanding the STT results requires modeling of spin transport. I use the spin diffusion equation [9, 16] including spin generation terms,

$$\frac{\partial \mu_S}{\partial t} = D\frac{\partial^2 \mu_S}{\partial^2 z} - \frac{\mu_S}{\tau_S} + \left(\frac{g_S}{N_S}\right), \tag{6.5}$$

where μ_S=$\mu_\uparrow$-$\mu_\downarrow$ is the spin chemical potential, D is the spin diffusion constant, τ_S is the spin relaxation time, g_S is the spin generation rate, and N_S is the spin density of states ($N_S = \frac{N_{FM1}}{2}$, where N_{FM1} is the electronic density of states of FM1). The μ_S of adjacent layers are related by the spin conductance at the interfaces; μ_S is set to zero at the boundary with CoFeB. I incorporate two spin generation terms: i) the volumetric $g_S = -\frac{dM}{dt}$ in FM1; and ii) the interfacial $G_S = (-/+)\left(\frac{\mu_B}{e}\right)\left(\frac{S_S}{LT}\right)J_Q$ at FM1/Cu and Pt/FM1 interfaces. For g_S, I obtain dM/dt from the experimental demagnetization data (Fig. 6.5 (b)), and for G_S, I use S_S as a free parameter with J_Q from our models of the thermal transport (Fig. 6.4).

The amount of spin current that is absorbed by the CoFeB layer depends on the spin transport coefficients and spin relaxation times. Values for D, τ_S, and spin conductances are estimated from previous reports with the exception of τ_S of [Co/Pt] and [Co/Ni] (chapter 4 and 5). Given the same spin generation rate in FM1, the larger τ_S of FM1 leads to a larger spin current to FM2. Therefore, S_S and τ_S of [Co/Pt] and [Co/Ni] are free parameters that I adjust to fit the model to spin accumulation and STT data.

The SDSE effect is revealed most clearly in the STT data with the 100 nm thick Cu heat sink layer. Solving Eq. (6.5) in the [Co/Pt] or [Co/Ni]/Cu-100/CoFeB sample, we obtain spin currents to CoFeB (J_{S_FM2}) (Figs. 6.8 (a) and (b)) then calculate STT-driven magnetization dynamics using J_{S_FM2} as the spin torque term (Eq. (5.4)). The sign and magnitude of S_S determine the initial slope and phase of the CoFeB precession dynamics (Figs. 6.8 (c) and (d)). From the simultaneous fitting of calculations both to the spin accumulation (Fig. 6.5) and STT results (Figs. 6.6 and 6.7, we determine τ_S = 0.02 and 0.1 ps, and S_S = 6 and -12 μV for [Co/Pt] and [Co/Ni], respectively. Previously, the S_S of NiFe and Co were reported from non-local measurements of spin accumulation of a 3D-nanostructure and the simulations of the temperature fields with steady-state heating [3, 17]. Our result shows that S_S can be obtained from STT measurement of thin-film structures with a pulsed heating and time-resolved optical-based temperature measurements of each layer in the structure.

We show comparisons between experiments and calculations in Figs. 6.5 and 6.6. The calculations show that the offset component of the spin accumulation is predominantly due to SDSE (Solid lines in Fig. 6.5 (a)). For STT, we calculate the magnetization dynamics of FM2 from J_{S_FM2} of Figs. 6.8 (a) and (b). The calculation accurately describes the amplitudes and phases of the precession of FM2 (Solid lines in Fig. 6.6 (a) and (b)).

The magnitude and phase of the precession can be understood from the Fourier transform of J_{S_FM2} (F_J) at the precession frequency of 7.8 GHz (Fig. 6.6 (c) and (d)). The Fourier component of the demagnetization-driven J_{S_FM2} is mostly real because its timescale is much shorter than the precession period, 130 ps. By contrast, the Fourier component of the SDSE-driven J_{S_FM2} has a significant imaginary part due to its long lifetime. The vector sum of Fourier component of the

demagnetization-driven J_{S_FM2} and the SDSE-driven J_{S_FM2} determines the amplitude and phase of precession of FM2.

Experimental support for the large difference in τ_S of [Co/Pt] and [Co/Ni] can be found in recent research on the interface spin-flipping parameter (δ) of [Co/Pt] and [Co/Ni] interfaces [18, 19], δ = 0.9 and δ = 0.35 for [Co/Pt] and [Co/Ni], respectively. If interface spin-flips are the primary source for the spin relaxation, δ should be inversely proportional to the effective spin diffusion length (l_S) of the multilayer. Using $\tau_S = \frac{l_S^2}{D}$, the difference of δ leads to a seven times smaller τ_S of [Co/Pt] than [Co/Ni]. Table 6.2 summarizes the experimentally determined τ_S of different FMs.

For the opposite sign of S_S of [Co/Pt] and [Co/Ni], I propose an explanation in terms of τ_S. The thermoelectric power S depends on the energy derivative of electrical conductivity $\partial\sigma/\partial E$ at the Fermi energy E_F, and the spin-dependent $\partial\sigma/\partial E$ gives the spin-dependent S [20, 21],

$$S_{\uparrow,\downarrow} = -eL_oT\frac{1}{\sigma_{\uparrow,\downarrow}}\frac{\partial\sigma_{\uparrow,\downarrow}}{\partial E}\bigg|_{E_F}. \tag{6.6}$$

In the 3*d* transition metals, the *s* electrons are the main carriers of electrical current, and the interband *sd* scattering controls σ [20-22]. I approximate $\sigma = ne^2\tau_{sd}/m^*$, where n is number density, m^* is the effective mass, and τ_{sd} is the relaxation time and is primarily determined by the density of states of *d* electrons at E_F, $N^d(E_F)$, and the *sd* scattering matrix $V_{k,k'}^{sd}$,

$$\frac{1}{\tau_{sd}} = \frac{2\pi}{\hbar}N^d(E_F)\cdot\sum_{k'}\left|V_{k,k'}^{sd}\right|^2. \tag{6.7}$$

Mott's original two current model assumes that the spin of *s* electrons is conserved during scattering process at a temperature well below the Curie temperature where the number of magnons is negligible [20-22]. In our experiment, the relatively short spin relaxation time, especially for [Co/Pt], suggests that the spin-flip scattering occurs with a not negligible number of magnons.

Here I extend the Mott's *sd* scattering model including the spin-flip scattering process. Using Matthiessen's rule, the relaxation time of *s* electron can be expressed in terms of spin-conserved and spin-flipping relaxation times, τ_{sd}^{sc} and τ_{sd}^{sf}:

$$\frac{1}{\tau_{sd}} = \frac{1}{\tau_{sd}^{\mathrm{sc}}} + \frac{1}{\tau_{sd}^{\mathrm{sf}}}. \tag{6.8}$$

Consequently, the difference in the density of states of the majority and minority *d* electrons gives rise to the spin-dependent relaxation time of the majority and minority *s* electrons:

$$\frac{1}{\tau_{sd}^{\uparrow,\downarrow}} = \frac{2\pi}{\hbar}\left(N_{\uparrow,\downarrow}^{\mathrm{d}}(E_{\mathrm{F}}) \cdot \Sigma^{\mathrm{sc}} + N_{\downarrow,\uparrow}^{\mathrm{d}}(E_{\mathrm{F}}) \cdot \Sigma^{\mathrm{sf}}\right), \tag{6.9}$$

where Σ^{sc} and Σ^{sf} are the summations in Eq. (6.7) for the spin-conserved and spin-flipping *sd* scatterings, respectively. Then spin-dependent σ is then

$$\sigma_{\uparrow,\downarrow} = \frac{ne^2}{m^*}\frac{\hbar}{2\pi}\left(N_{\uparrow,\downarrow}^{\mathrm{d}}(E_{\mathrm{F}}) \cdot \Sigma^{\mathrm{sc}} + N_{\downarrow,\uparrow}^{\mathrm{d}}(E_{\mathrm{F}}) \cdot \Sigma^{\mathrm{sf}}\right)^{-1}. \tag{6.10}$$

Thus, the energy derivative of $\sigma_{\uparrow,\downarrow}$ becomes

$$\frac{\partial \sigma_{\uparrow,\downarrow}}{\partial E} = -\frac{ne^2}{m^*}\frac{\hbar}{2\pi}\left(\left.\frac{\partial N_{\uparrow,\downarrow}^{\mathrm{d}}}{\partial E}\right|_{E_{\mathrm{F}}} \cdot \Sigma^{\mathrm{sc}} + \left.\frac{\partial N_{\downarrow,\uparrow}^{\mathrm{d}}}{\partial E}\right|_{E_{\mathrm{F}}} \cdot \Sigma^{\mathrm{sf}}\right)\left(N_{\uparrow,\downarrow}^{\mathrm{d}}(E_{\mathrm{F}}) \cdot \Sigma^{\mathrm{sc}} + N_{\downarrow,\uparrow}^{\mathrm{d}}(E_{\mathrm{F}}) \cdot \Sigma^{\mathrm{sf}}\right)^{-2}. \tag{6.11}$$

Here, I ignored the energy dependency of Σ for simplicity under the assumption that the scattering matrix is approximately constant near E_{F}.

These simple derivations indicate that the sign of S_{S} is determined by the signs and magnitudes of $\left.\frac{\partial N_{\uparrow,\downarrow}^{\mathrm{d}}}{\partial E}\right|_{E_{\mathrm{F}}}$, and the relative magnitude of Σ^{sc} and Σ^{sf}. The band structure shows $\left.\frac{\partial N_{\uparrow}^{\mathrm{d}}}{\partial E}\right|_{E_{\mathrm{F}}} < 0$ and $\left.\frac{\partial N_{\downarrow}^{\mathrm{d}}}{\partial E}\right|_{E_{\mathrm{F}}} > 0$ for [Co/Pt] and [Co/Ni] [23]. If $\Sigma^{\mathrm{sc}} >> \Sigma^{\mathrm{sf}}$, $\partial\sigma^{\uparrow}/\partial E > 0$ and $\partial\sigma^{\downarrow}/\partial E < 0$, which consequently gives $S_{\mathrm{S}} < 0$. This is the case of the [Co/Ni] layer which shows a relatively long spin relaxation time. By contrast, if $\Sigma^{\mathrm{sc}} \approx \Sigma^{\mathrm{sf}}$, there could be a sign inversion in the spin-dependent $\partial\sigma/\partial E$, i.e., $\partial\sigma^{\uparrow}/\partial E < 0$ and $\partial\sigma^{\downarrow}/\partial E > 0$, which consequently result in $S_{\mathrm{S}} > 0$. The very short spin relaxation time of the [Co/Pt] layer suggests $\Sigma^{\mathrm{sc}} \approx \Sigma^{\mathrm{sf}}$.

6.4 Conclusion

For thermal STT, the input is an energy density rather than a charge current density as in more conventional spintronics. Using a [Co/Ni] layer as a spin source, an energy fluence of ≈4 J m^{-2} induces thermal STT that generates a ≈1 % tilting of the 2 nm-thick CoFeB magnetization. One route to greater energy efficiency is to increase S_S by controlling $\frac{\partial N_{\uparrow,\downarrow}^{d}}{\partial E}$. For example, the minority band of half-metallic materials have $\left.\frac{\partial N_{\downarrow}^{d}}{\partial E}\right|_{E>E_F} > 0$ and $\left.\frac{\partial N_{\downarrow}^{d}}{\partial E}\right|_{E<E_F} < 0$. If the Fermi energy of these materials can be controlled, the sign and magnitude of S_S can be tuned. Recently, it was reported that the CoFeAl alloy can have a much larger S_S because of its favorable band structure [24]. The engineering of ferromagnet band structure raises prospects for an enhanced thermal STT.

6.5 References

1. M. Hatami, G. E. W. Bauer, Q. Zhang, and P. J. Kelly, Phys. Rev. Lett. **99**, 066603 (2007).
2. J. C. Slonczewski, Phys. Rev. B **82**, 054403 (2010).
3. A. Slachter, F. L. Bakker, J-P. Adam, ad B. J. van Wees, Nature Phys. **6**, 879 (2010).
4. K. Uchida, J. Xiao, H. Adachi, J. Ohe, S. Takahashi, J. Ieda, T. Ota, Y. Kajiwara, H. Umezawa, H. Kawai, G. E. W. Bauer, S. Maekawa, and E. Saitoh, Nature Mater. **9**, 898 (2010).
5. J.-C. Le Breton, S. Sharma, H. Saito, S. Yuasa, and R. Jansen, Nature **475**, 82 (2011).
6. H. Yu, S. Granville, D. P. Yu, and J.-Ph. Ansermet, J.-Ph. Phys. Rev. Lett. **104**, 146601 (2010).
7. J. Flipse, F. K. Dejene, and B. J. van Wees, Phys. Rev. B **90**, 104411 (2014).

8. G.-M. Choi, C.-H. Moon, B.-C. Min, K.-J. Lee, and D. G. Cahill, Nature Phys. accepted.
9. G.-M. Choi, B.-C. Min, K.-J. Lee, and D. G. Cahill, Nat. Commun. **5**, 4334 (2014).
10. G.-M. Choi and D. G. Cahill, Phys. Rev. B **90**, 214432 (2014).
11. G.-M. Choi, R. B. Wilson, and D. G. Cahill, Phys. Rev. B **89** 064307 (2014).
12. J. Hohlfeld, Chem. Phys. **251**, 237 (2000).
13. A. P. Caffrey, P. E. Hopkins, J. M. Klopf, and P. M. Norris, P. M. Microscale Thermophys. Eng. **9**, 365 (2005).
14. W. Wang and D. G. Cahill, Phys. Rev. Lett. **109**, 175503 (2012).
15. M. D. Stiles and A. Zangwill, Phys. Rev. B **66**, 014407 (2002).
16. T. Valet and A. Fert, Phys. Rev. B **48**, 7099 (1993).
17. F. K. Dejene, J. Flipse, B. J. van Wees, Phys. Rev. B **86** 024436 (2012).
18. H. Y. T. Nguyen, R. Acharyya, E. Huey, B. Richard, R. Loloee, W. P. Pratt Jr., J. Bass, S. Wang, and K. Xia, Phys. Rev. B **82**, 220401(R) (2010).
19. H. Y. T. Nguyen, W. P. Pratt Jr., and J. Bass, J. Magn. Magn. Mater. **361**, 30 (2014).
20. N. F. Mott, Proc. R. Soc. Lond. A **156**, 368 (1936).
21. N. F. Mott, Proc. R. Soc. Lond. A **153**, 699 (1936).
22. T. R. Mcguire and R. I. Potter, IEEE Trans. Magn. **11**, 1018 (1975).
23. S. Uba, L. Uba, A. N. Yaresko, A. Ya. Perlov, V. N. Antonov, and R. Gontarz, Phys. Rev. B **53**, 6526 (1996).
24. S. Hu, H. Itoh, and T. Kimura, NPG Asia Mater. **6**, e127 (2014).
25. Y. S. Touloukian, ed. *Thermophysical Properties of High Temperature Solid Materials*. vol. 1 (Macmillan, New York, 1967).

26. A. Tari, *The Specific Heat of Matter at Low Temperatures*. (Imperial College Press, London, 2003).

6.6 Figures and Tables

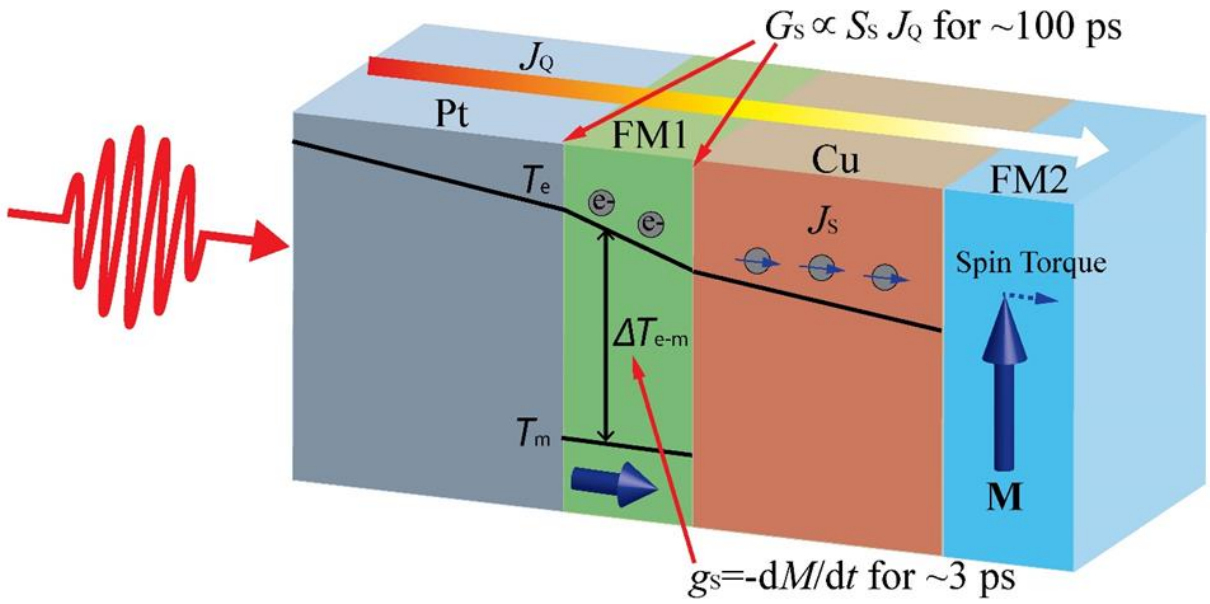

Fig. 6.1: Conceptual diagram. The pump optical pulse is incident on the Pt side and creates an ultrafast temperature excursion. The temperature difference between electron (T_e) and magnon (T_m) of FM1 induces rapid demagnetization, ΔM. The time derivative of demagnetization produces a volumetric spin generation rate g_S that persists for the first ~3 ps. The temperature difference between Pt and Cu induces heat current through FM1, J_Q, which persists for ~100 ps. The J_Q produces an interfacial spin generation rate $G_S \propto S_S J_Q$, where S_S is spin-dependent Seebeck coefficient. Gradients in the spin chemical potential drive a diffusive spin current J_S that passes through the Cu layer and applies a spin torque to FM2 [8].

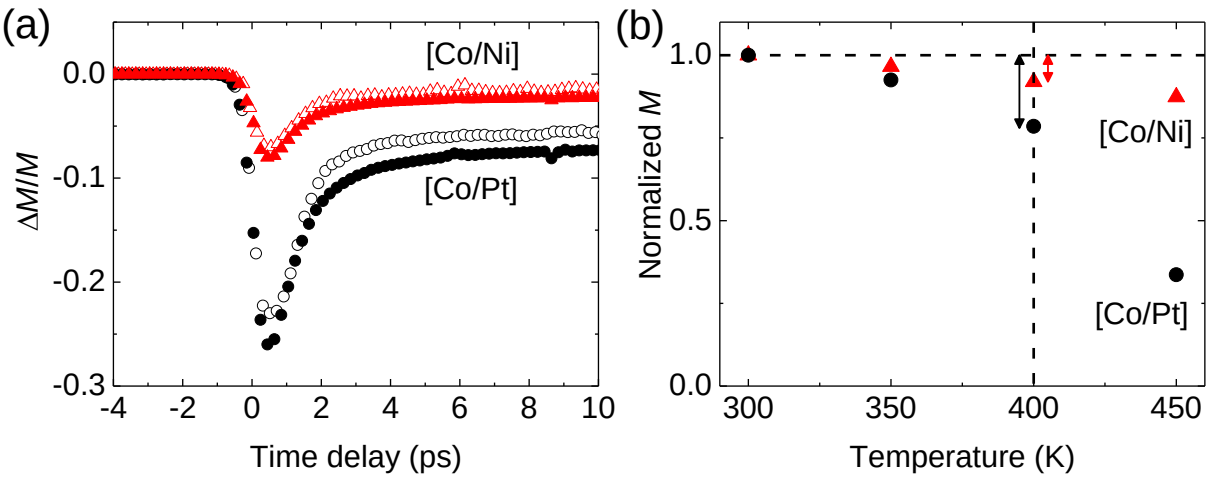

Fig. 6.2: (a) Demagnetization data measured on the Pt side of the [Co/Pt]/Cu-10/CoFeB (black filled circles), [Co/Pt]/Cu-100 (black open circles), [Co/Ni]/Cu-10/CoFeB (red filled triangles), and [Co/Ni]/Cu-100 (red open triangles) samples. (b) The magnetization of the [Co/Pt] (black circles) and [Co/Ni] (red triangles) layers at different temperature. At the temperature excursion of ΔT=100 K, indicated by vertical dotted line, $\Delta M/M$ are 0.22 (black arrow) and 0.08 (red arrow) for [Co/Pt] and [Co/Ni], respectively [8].

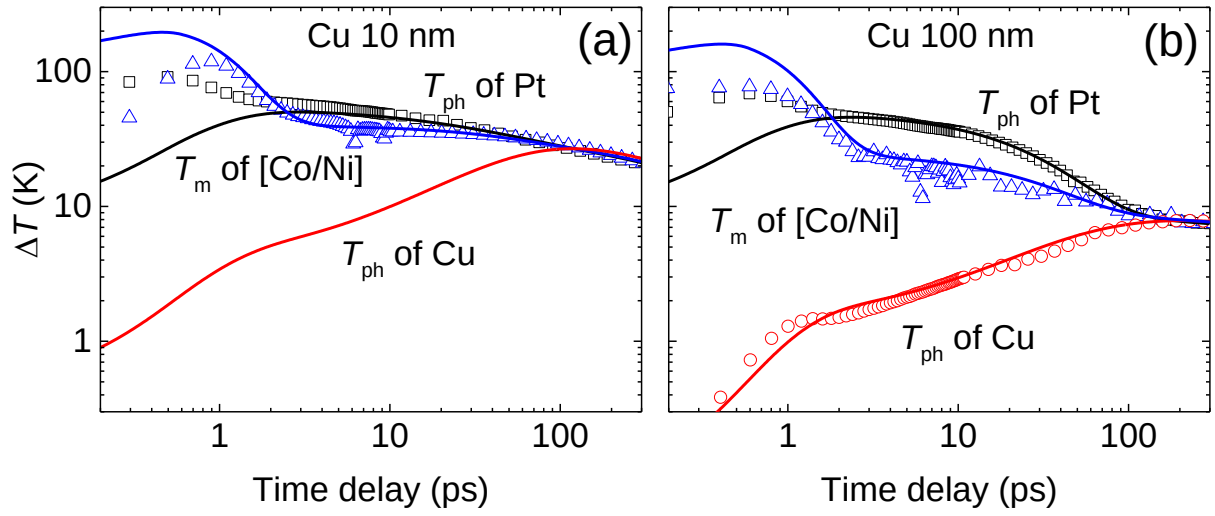

Fig. 6.3: Thermal analysis. Temperature measurements of each layer of the (a) [Co/Ni]/Cu-10/CoFeB and (b) [Co/Ni]/Cu-100 samples: Pt phonon temperature from a TDTR measurement on the Pt side (black squares); Cu phonon temperature from a TDTR measurement on the Cu side (red circles); [Co/Ni] magnon temperature from MOKE measurement on the Pt side (blue triangles). Solid lines are results of thermal modeling: black solid line is for Pt phonon temperatures; red solid line is for Cu phonon temperatures; blue solid line is for [Co/Pt] electron temperatures (I neglect magnon heat capacity in the modeling for simplicity) [8].

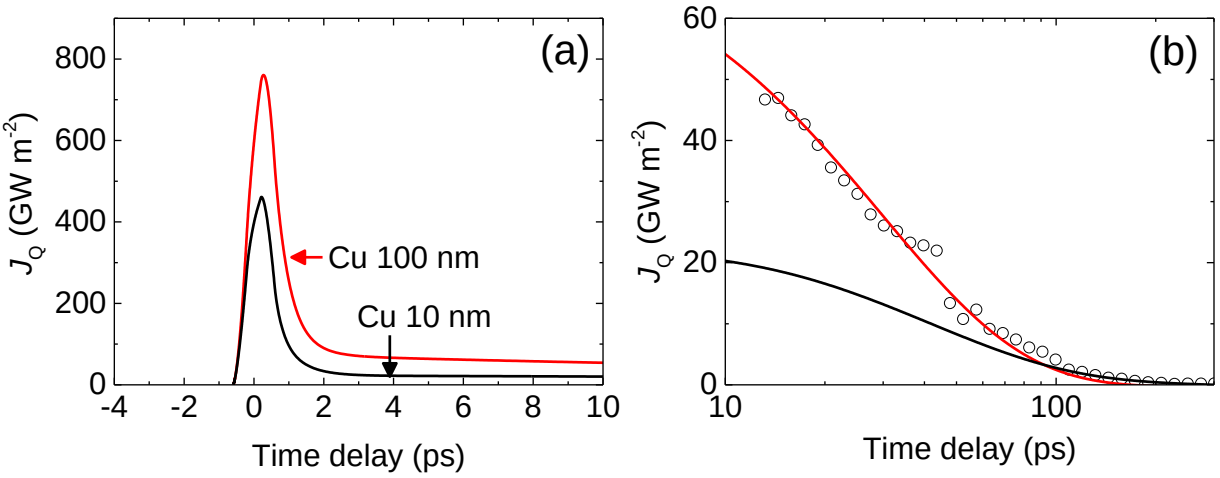

Fig. 6.4: The estimation of the heat current through FM1. (a) The heat current through the [Co/Ni] layer of the [Co/Ni]/Cu-10/CoFeB (black line) and [Co/Ni]/Cu-100 (red line) samples from thermal modeling. (b) The heat current at the time scale of 10~300 ps: solid lines are from modeling, and black circles are the heat current leaving the Pt layer determined from the measured cooling rate of the Pt layer [8].

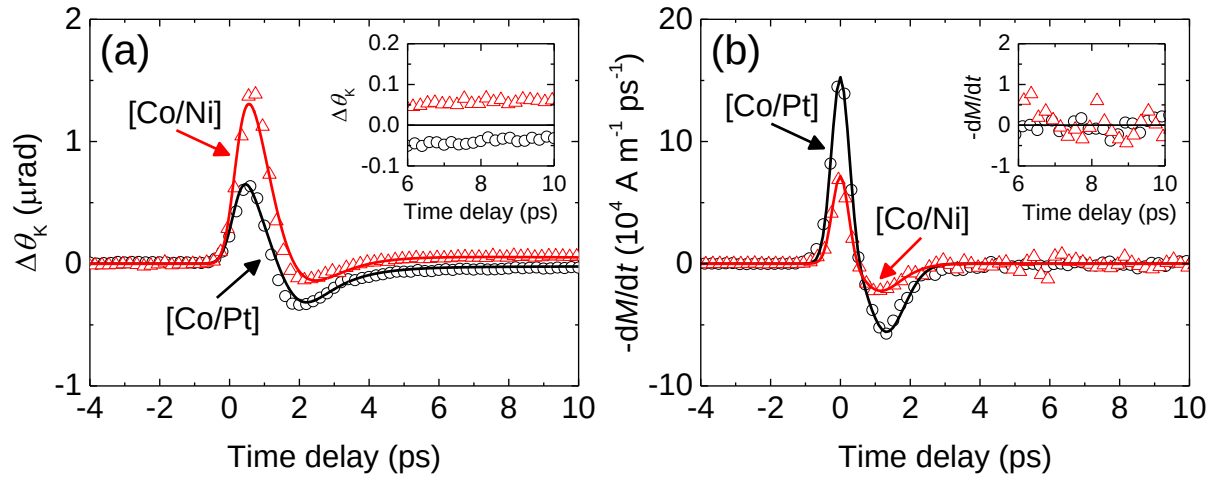

Fig. 6.5: Spin accumulation in Cu. (a) Kerr rotation measured on the Cu side of the [Co/Pt]/Cu-100 (black circles) and [Co/Ni]/Cu-100 samples (red triangles). Solid lines are calculations with τ_S = 0.02 and 0.1 ps, and S_S = 6 and -12 μV for [Co/Pt] and [Co/Ni], respectively (Supplementary Note 8). (b) The negative of demagnetization rate, -dM/dt, of [Co/Pt]/Cu-100 (black circles) and [Co/Ni]/Cu-100 samples (red triangles): data points are obtained by numerical differentiation of demagnetization data (Supplementary Note 1) and solid lines are fittings with Gaussian function. Insets of (a) and (b) are zoomed-in data around y-axis at zero (units of the y-axis are the same as those of (a) and (b), respectively.) All measurements are done without a magnetic field [8].

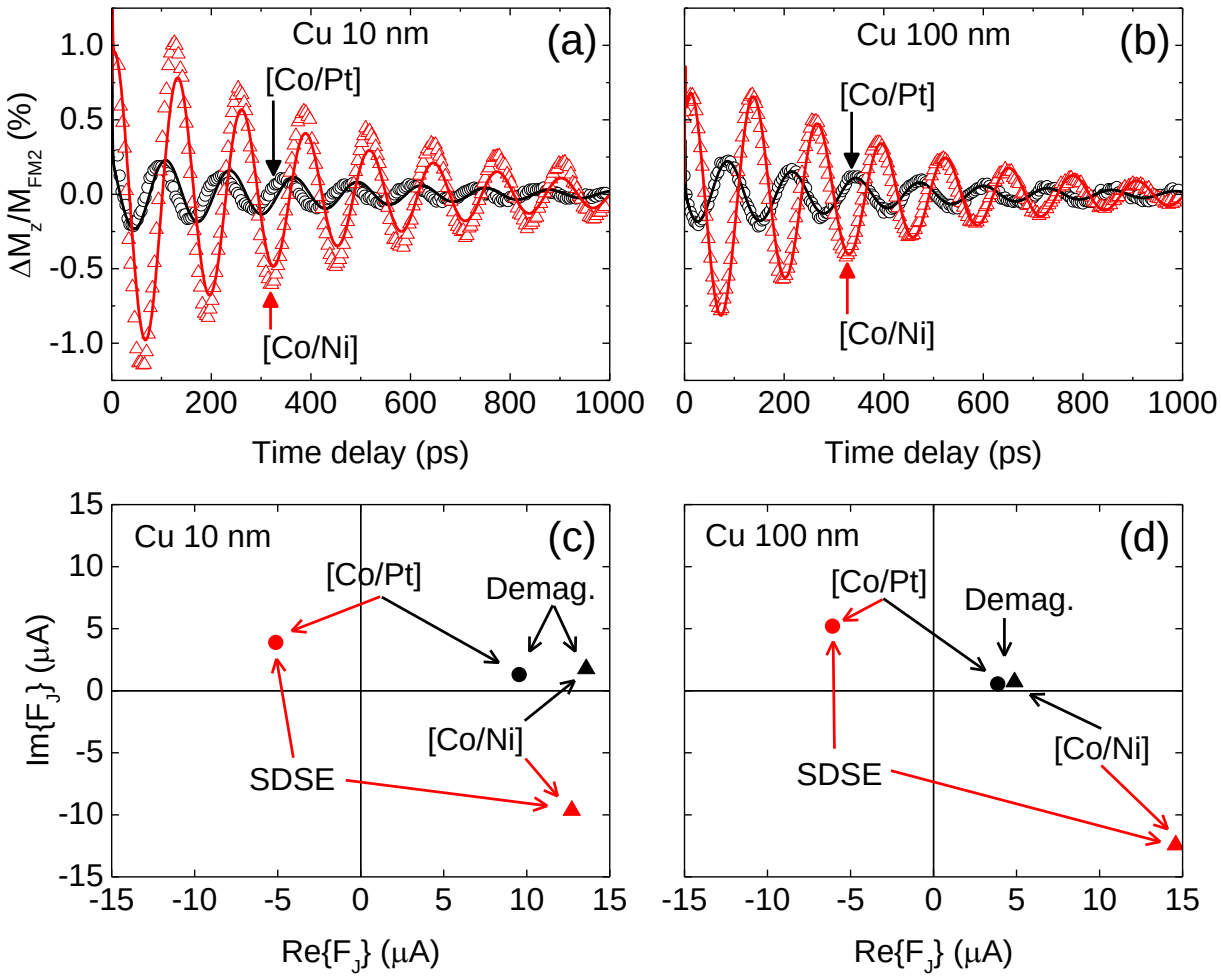

Fig. 6.6: STT on CoFeB at long time scale. (a) The magnetization dynamics of CoFeB of the [Co/Pt]/Cu-10/CoFeB (black circles) and [Co/Ni]/Cu-10/CoFeB (red triangles) samples. (b) The magnetization dynamics of CoFeB of the [Co/Pt]/Cu-100/CoFeB (black circles) and [Co/Ni]/Cu-100/CoFeB (red triangles) samples. All measurements are done with an in-plane magnetic field of 0.05 T. Solid lines are calculations with τ_S = 0.02 and 0.1 ps, and S_S = 6 and -12 μV for [Co/Pt] and [Co/Ni], respectively. Fourier transform of spin currents (F_J) to CoFeB with (c) Cu 10 nm and (f) Cu 100 nm at frequency of 7.8 GHz (*x*-axis (*y*-axis) is the real (imaginary) parts of Fourier transform): circles are with [Co/Pt] and triangles are with [Co/Ni]; black color is for the demagnetization-driven contribution and red color is for the SDSE-driven contribution [8].

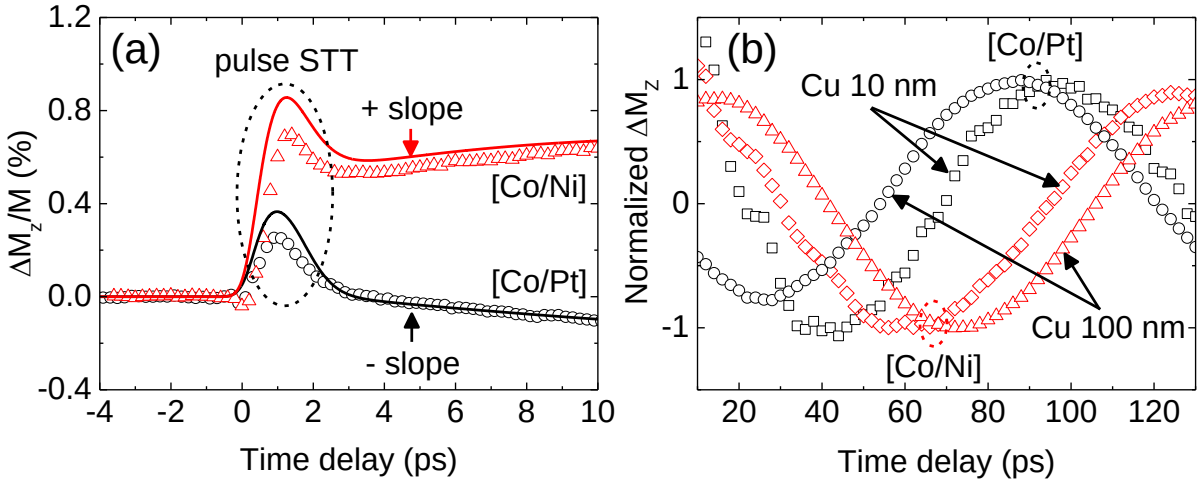

Fig. 6.7: STT on CoFeB at short time scales. (a) The magnetization dynamics of CoFeB at time scales of -4 to 10 ps: black circles are for [Co/Pt]/Cu-100/CoFeB; red triangles are for [Co/Ni]/Cu-100/CoFeB; solid lines are the same as those of Fig. 4 (b). (b) The magnetization dynamics of CoFeB at time scales of 10 to 130 ps: black squares are for [Co/Pt]/Cu-10/CoFeB; black circles are for [Co/Pt]/Cu-100/CoFeB; red diamonds are for [Co/Ni]/Cu-10/CoFeB; red triangles are for [Co/Ni]/Cu-100/CoFeB. All data are normalized by their peak value. All measurements are done with an in-plane magnetic field of 0.05 T [8].

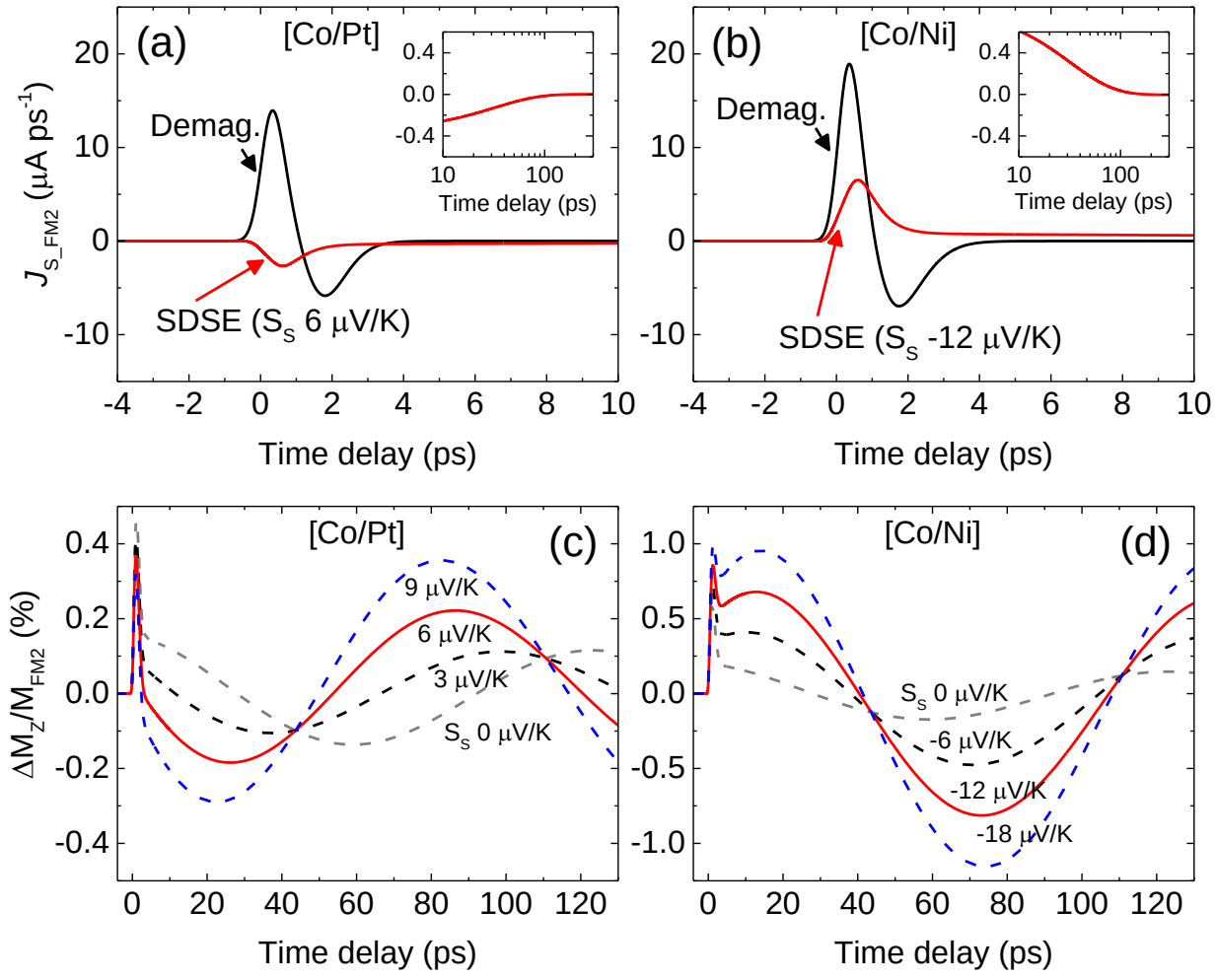

Fig. 6.8: The effect of SDSE on STT. The calculated spin current that is absorbed by the CoFeB layer in the (a) [Co/Pt]/Cu-100/CoFeB and (b) [Co/Ni]/Cu-100/CoFeB samples: the black and red solid lines are driven by demagnetization and SDSE, respectively. Insets of (a) and (b) are the SDSE-driven spin currents at time scale of 10~300 ps. Plots of (a) and (b) are done by setting τ_S of 0.02 and 0.1 ps, and S_S of 6 and -12 μV for [Co/Pt] and [Co/Ni], respectively. STT-driven magnetization dynamics of CoFeB of the (c) [Co/Pt]/Cu-100/CoFeB and (d) [Co/Ni]/Cu-100/CoFeB samples. For (c), τ_S of [Co/Pt] is fixed at 0.02 ps, and S_S is set to 0, 3, 6, and 9 μV K^{-1} for grey dotted, black dotted, red solid, and blue dotted line, respectively. For (d), τ_S of [Co/Ni] is fixed at 0.1 ps, and S_S is set to 0, -6, -12, and -18 μV K^{-1} for grey dotted, black dotted, red solid, and blue dotted line, respectively [8].

Table 6.1: Parameters for the thermal modeling: C_{total} is the total heat capacity, γ the electronic heat capacity coefficient, σ is the electrical conductivity, Λ the thermal conductivity, and $g_{e\text{-}p}$ the electron-phonon coupling parameter. I set the interfacial thermal conductance, G=100 MW m^{-2} K^{-1}, at the sapphire/Pt interface [8].

	sapphire	**Pt**	**[Co/Pt]**	**[Co/Ni]**	**Cu**
C_{total} (10^6 J m^{-3} K^{-1})	3.08 [a]	2.85 [a]	3.15 [b]	3.89 [b]	3.45 [a]
γ (J m^{-3} K^{-2})		721 [c]	699 [b]	930 [b]	97 [c]
σ (10^7 Ω^{-1} m^{-1})		0.66 [d]	0.23 [d]	0.3 [d]	3.9 [d]
Λ (W m^{-1} K^{-1})	30 [f]	50 [e]	20 [e]	26 [e]	300 [e]
$g_{e\text{-}p}$ (10^{16} W m^{-3} K^{-1})		42 [f]	42 [g]	42 [g]	7 [f]

[a] Reference 25.
[b] Obtained by the weighted sum of heat capacities of Pt, Co, and Ni.
[c] Reference 26.
[d] Obtained from four-point probe measurement.
[e] Obtained by from electrical conductivity and Wiedemann-Franz law.
[f] Obtained as fitting parameters for thermal transport analysis.
[g] I use the same value of Pt.

Table 6.2: Comparison of spin accumulation in the Pt/FM/Cu structure with different FM: $\Delta M/M$ is the peak demagnetization of FM, $\Delta\theta_K$ is the peak Kerr rotation on Cu, and τ_S is the spin relaxation time of FM. Samples 1, 4, and 5 are fabricated at KIST; samples 2 and 3 are at UIUC [8].

	$\Delta M/M$	$\Delta\theta_K$ (μrad)	τ_S (ps)
Sample 1[a]	0.08	0.18 (0.25*)	0.02
Sample 2[b]	0.08	0.11	0.01
Sample 3[c]	0.24	0.36	0.01
Sample 4[d]	0.23	0.61	0.02
Sample 5[e]	0.07	1.4	0.1

[a] Pt(30)/[Co(0.4)/Pt(1)]$_{\times 4}$/Co(0.2)/Ni(0.4)/Co(0.2)/Cu(80) (unit in nm)
[b] Pt(30)/[Co(0.4)/Pt(1)]$_{\times 4}$/Co(0.4)/Cu(100) (unit in nm)
[c] Pt(20)/[Co(0.4)/Pt(1)]$_{\times 4}$/Co(0.4)/Cu(100) (unit in nm)
[d] Pt(20)/[Co(0.2)/Pt(0.4)]$_{\times 5}$/Co(0.2)/Cu(100) (unit in nm)
[e] Pt(20)/[Co(0.2)/Ni(0.4)]$_{\times 5}$/Co(0.2)/Cu(100) (unit in nm)
*value after subtracting demagnetization signal from raw data

CHAPTER 7

OPTICAL HELICITY-DRIVEN SPIN TRANSFER TORQUE

Parts of this chapter will be published in "Optical helicity-driven spin transfer torque in metallic ferromagnets" Gyung-Min Choi and David G. Cahill, in preparation.

7.1 Introduction

While the demagnetization-driven and SDSE-driven STT is originated from photon's energy, it would be a natural question if photon's angular momentum can contribute to STT. Optical spin generation has been investigated mostly in III-V semiconductors [1-3]. For the direct bandgap semiconductor GaAs, a circularly polarized light can generate spin-polarized electrons in the conduction band by spin-selective transition from the valence band to the conduction band [1-3]. From the optical selection rule, the relationship between number of photons and number of spin-polarized electrons is $\frac{n_{spin}}{n_{photon}} = 0.5$ [2, 3]. When the semiconductor has a collective magnetic moment, the spin-polarized electrons in the conduction band can interact with magnetization and results in STT. Nemec *et al.* reported this optical STT with the (Ga, Mn)As ferromagnet semiconductor, where Mn provides the ferromagnetic moment [4]. They observed the precession

of the Mn magnetic moment driven by circularly polarized light and interpreted it as a result of the optical STT [4].

Another mechanism for the optical-helicity-driven magnetization dynamics is the Inverse Faraday effect (IFE). IFE was reported with the ferrimagnetic garnet system [5, 6]. It has been interpreted that IFE creates a strong axial magnetic field during the light pulse; then this magnetic field triggers the magnetization dynamics of the ferrimagnetic garnet [5, 6].

For metallic ferromagnets, it has been shown that optical helicity of the pump beam produces a transient Kerr rotation of probe beam at zero-time delay during the overlap between pump and probe [7, 8]. However, its effect on magnetization dynamics was shown to be negligible [7, 8]. On the contrary, Lambert *et al.* reported that optical-helicity dependent magnetization switching of metallic ferromagnets [9]. They claimed that when a high intensity of light heats up metallic ferromagnets close to the Curie temperature the light helicity has a detrimental role in the direction of remagnetization during cooling [9]. However, whether the light helicity affects magnetization by optical STT or IFE is not clear, and its quantitative analysis has not been shown.

In this work, I show that light helicity triggers magnetization dynamics of metallic Co film [10]. The dynamics can be explained with optical STT but not with IFE. I also quantify the magnitude of optical STT and explain it with the optical selection rule and band structure of Co.

7.2 Experiment

The concept of how I generate STT from optical helicity is shown schematically in Fig. 7.1. The circularly polarized pump laser pulse excites a metallic ferromagnet, whose magnetization lies in in-plane direction. The pump pulse induces the dipolar transitions in electrons of the

ferromagnet layer and results in a finite spin polarization in electrons. The spin-polarized electrons can interact with magnetization and result in STT. The linearly polarized probe beam detects the optical STT-driven magnetization dynamics by magneto-optical Kerr effect (MOKE).

I prepared a thin ferromagnetic structure of the sapphire substrate/ Co (10 nm)/ Pt (2 nm) using a three target sputtering system in university of Illinois. The base pressure is less than 5×10^{-8} Torr. The magnetization of the Co layer lies in in-plane direction due to its shape anisotropy. It also has a finite crystalline anisotropy in in-plane direction. The Pt layer acts as a capping layer preventing Co from oxidation.

The pump beam is incident on the sapphire side of the sample and creates optical STT by the dipolar transition in electrons in the Co layer. I use time-resolved measurements of the polar MOKE to detect the perpendicular component of the magnetization dynamics of the Co layer with the linearly polarized probe beam on the Pt side of the sample. The light wavelength is 785 nm, and the full-width-at-half-maximum of the pump and probe are ≈0.8 and ≈0.3 ps, respectively. The incident pump fluence is 7 J m^{-2}; the absorbed fluence is 3.5 J m^{-2}. An in-plane magnetic field of 0.05 T is applied during the MOKE measurement to set the direction of magnetization of Co. All measurements are performed at room temperature.

7.3 Results and discussion

For a prerequisite experiment, I first measure the magnetization dynamics of Co with a linearly polarized pump pulse (Fig. 7.2). As there is a crystalline magnetization anisotropy at in-plane direction, I measure magnetization dynamics of Co varying the angle, ϕ, between the easy axis of crystalline anisotropy and the direction of applied magnetic field. When the ϕ is not zero, even a linearly polarized pump can trigger the magnetization precession of Co. I consider this is

because the pump pulse creates a rapid heating and subsequent change of magnetization anisotropy. This rapid change of the magnetization anisotropy creates the anisotropy field pulse that triggers a coherent precession of the magnetization [11]. Note that the precession is suppressed by aligning the easy axis of the crystalline anisotropy to the direction of the magnetic field.

I measure the effect of the light helicity on the magnetization dynamics using a circularly polarized pump beam (Fig. 7.3). The light helicity clearly affects the magnetization dynamics of Co. Especially, when the ϕ is close zero, the magnetization dynamics driven by left (LCP) and right (RCP) circularly polarized pump is close to symmetric. The unsymmetrical behavior with increasing ϕ is because the anisotropy-field-driven precession is superposed on the light-helicity-driven precession. I extract the helicity dependent part by plotting the difference between LCP and RCP results, and it stays nearly the same irrespective of ϕ (Fig. 7.4). The helicity dependent part, LCP – RCP, is well fitted with a damped cosine function of $A\times\cos(2\pi ft+\phi)\times\exp(-t/\tau)$: the amplitude, A, is 0.7 μrad; the frequency, f, is 8.1 GHz; the decay time, τ, is 400 ps. The frequency is well explained by Kittel's equation, $f=\frac{\gamma_e}{2\pi}\sqrt{B_x(B_x+\mu_0 M_S)}$, where γ_e =1.76×10^{11} rad s^{-1} T^{-1} is the electron gyromagnetic ratio, B_x is the in-plane magnetic field of 0.05 T, μ_0 is the vacuum permeability, and M_S is the saturation magnetization of Co of 1.3×10^6 A m^{-1}.

The fact that the helicity dependent part can be fitted with a cosine-like function is sharp contrast to IFE. The IFE-driven magnetization dynamics should be a sine-like function, $A\times\sin(2\pi ft+\phi)\times\exp(-t/\tau)$ because the IFE initially rotates the magnetization in the in-plane direction due to an axial magnetic field during the pump pulse [6]. After the pump pulse, the magnetization starts to evolve in the out-of-plane direction as it precesses around its easy axis [6]. On the contrary, the optical STT should tilt magnetization initially in the out-of-plane direction as the optically induced spin polarization of electrons points to out-of-plane direction [4].

The spin-polarized electrons either relax to phonon by the spin relaxation or be absorbed by magnetization by the so-called dephasing [12]. Considering a typical dephasing length of less than 1 nm [12] and Fermi velocity of 0.3×10^6 m sec^{-1} for Co [12], the time scale for the dephasing would be less than three femtoseconds. The spin relaxation time of Co has been reported to be about two picoseconds from the measured spin diffusion length of 38 nm at room temperature [13]. Although the *spin relaxation time* could be much smaller than 2 ps for optically excited electrons as it tends to decrease with energy [14, 15], I expect it is still larger than the timescale for the dephasing in our case, therefore most of spins of electrons should be absorbed by the magnetization.

To quantify the amount of optical STT, I compare the magnitude of the precession with the static Kerr rotation, due to the whole magnetization, M, of Co. With the static Kerr rotation of 0.46 degree (=8 mrad), the tilting angle of the precession is,

$$\frac{\Delta M}{M} = \frac{\Delta\theta_K}{\theta_K} = \frac{\Delta\theta_K(LCP) - \Delta\theta_K(RCP)}{2\theta_K} \approx 10^{-4}. \quad (7.1)$$

Then the number of spin-polarized electrons is calculated to be $10^{-4} \times \frac{M_S}{\mu_B} = 1.4 \times 10^{25}$ m^{-3}, where M_S of 1.3×10^6 A m^{-1} and μ_B of 9.27×10^{-24} A m^{-2}. The number of photons is calculated to be $\frac{E_{abs}}{\hbar\omega\times d_{Co}} = 1.4 \times 10^{27}$ m^{-3}, where E_{abs} is the absorbed energy flounce by the pump beam of 3.5 J m^{-2}, $\hbar\omega$ is the photon energy of 1.58 eV, and d_{Co} is the thickness of Co of 10 nm. Consequently, the ratio between the number of spin-polarized electrons and number of photons is $\frac{n_{spin}}{n_{photon}} \approx 10^{-2}$, which is almost two orders of magnitude smaller than that of the GaAs semiconductor [2, 3].

The small efficiency of optical STT in the Co film is because of the band structure. With a photon energy of 1.58 eV, the major dipolar transition is from the occupied 3*d* states to the empty 4*p* states. Using the dipolar selection rule (Δl=±1 and Δm_l=±1, where l is the orbital quantum

number, and m_l is the magnetic quantum number), I can calculate the matrix elements for relevant transitions. Similar calculation with the 3*d*-transition metals has been done with the x-ray magnetic circular dichroism, where x-ray triggers the interband transition from the 2*p* core state to the 3*d* valence state [16, 17]. With one photo with left circular polarization, the $3d_{3/2}$ ($j=l-s=3/2$) state produces 0.35 up spin and 0.05 down spin at the 4*p* state, and the $3d_{5/2}$ ($j=l+s=5/2$) state produces 0.15 up spin and 0.45 down spin at the 4*p* state (Fig. 7.5 (a)). If $3d_{3/2}$ and $3d_{5/2}$ states are degenerate, the net spin polarization will be zero.

Due to the spin-orbit coupling, there is an energy splitting (ΔE_{SO}) between $3d_{3/2}$ and $3d_{5/2}$ states (Fig. 7.5 (b)). The amount of spin polarization by a circularly polarized light is proportional to the ratio between the ΔE_{SO} and the bandwidth (ΔE_{3d}) of the 3d band. With $\Delta E_{SO} \approx 0.08$ eV [18] and $\Delta E_{3d} \approx 4$ eV, the fractional spin polarization per photon approximately is,

$$\frac{n_{spin}}{n_{photon}} = P_S(3d_{3/2} \rightarrow 4p) \times \frac{\Delta E_{SO}}{\Delta E_{3d}} = 0.3 \times \frac{0.08\ \text{eV}}{4\ \text{eV}} = 6 \times 10^{-3}, \qquad (7.2)$$

where P_S is the spin polarization of the dipolar transition from $3d_{3/2}$ to 4*p* bands. Although I ignored the complicated details of the band structure, this estimation reasonably explains with our experimental finding of $\frac{n_{spin}}{n_{photon}} \approx 10^{-2}$.

7.4 Conclusion

I have shown that circularly polarized light generates STT on magnetization of a metallic ferromagnet. The mechanism for the optical STT is the non-zero spin polarization during the dipolar transition from 3*d* to 4*p* bands of Co. The magnitude of the optical STT is approximately explained with the ratio of the spin-orbit splitting and bandwidth of the 3*d* band. Because the spin-orbit splitting is much smaller than the bandwidth, the spin polarizability is around 0.01 per photon.

7.5 References

1. F. Meier and B. P. Zakharchnya, *Optical Orientation* (North-Holland, 1984).
2. B. T. Jonker, Proc. IEEE **91**, 727 (2003).
3. T. Taniyama, E. Wada, M. Itoh, and M. Yamaguchi, NPG Asia Mater. **3**, 65 (2011).
4. P. Němec, E. Rozkotová, N. Tesařová, F. Trojánek, E. De Ranieri, K. Olejník, J. Zemen, V. Novák, M. Cukr, P. Malý, and T. Jungwirth, Nature Phys. **8**, 411 (2012).
5. A. V. Kimel, A. Kirilyuk, P. A. Usachev, R. V. Pisarev, A. M. Balbashov, and Th. Rasing, Nature **435**, 655 (2005).
6. F. Hansteen, A. Kimel, A. Kirilyuk, and T. Rasing, Phys. Rev. Lett. **95**, 047402 (2005).
7. R. Wilks, R. J. Hicken, M. Ali, B. J. Hickey, J. D. R. Buchanan, A. T. G. Pym, and B. K. Tanner, J. Appl. Phys. **95**, 7441 (2004).
8. F. D. Longa, J. T. Kohlhepp, W. J. M. de Jonge, and B. Koopmans, Phys. Rev. B **75** 224431 (2007).
9. C-H. Lambert, S. Mangin, B. S. D. Ch. S. Varaprasad, Y. K. Takahashi, M. Hehn, M. Cinchetti, G. Malinowski, K. Hono, Y. Fainman, M. Aeschlimann, E. E. Fullerton, Science **345** 1337 (2014).
10. G.-M. Choi and D. G. Cahill, to be submitted.
11. M. van Kampen, C. Jozsa, J. T. Kohlhepp, P. LeClair, L. Lagae, W. J. M. de Jonge, and B. Koopmans, Phys. Rev. Lett. **88**, 227201 (2002).
12. M. D. Stiles and A. Zangwill, Phys. Rev. B **66**, 014407 (2002).
13. L. Piraux, S. Dubois, A. Fert, and L. Belliard, Eur. Phys. J. B **4**, 413 (1998).
14. M. Aeschlimann, M. Bauer, S. Pawlik, W. Weber, R. Burgermeister, D. Oberli, and H. C. Siegmann, Phys. Rev. Lett. **79**, 5158 (1997).

15. V. P. Zhukov, E. V. Chulkov, and P. M. Echenique, Phys. Stat. Sol. (a) **205**, 1296 (2008).

16. G. Schütz, W. Wagner, W. Wilhelm, P. Kienle, R. Zeller, R. Frahm, and G. Materlik, Phys. Rev. Lett. **58**, 737 (1987).

17. H. Ebert, Rep. Prog. Phys. **59**, 1665 (1996).

18. F. Batallan, I. Rosenman, and C. B. Sommers, Phys. Rev. B. **11**, 545 (1975).

7.6 Figures

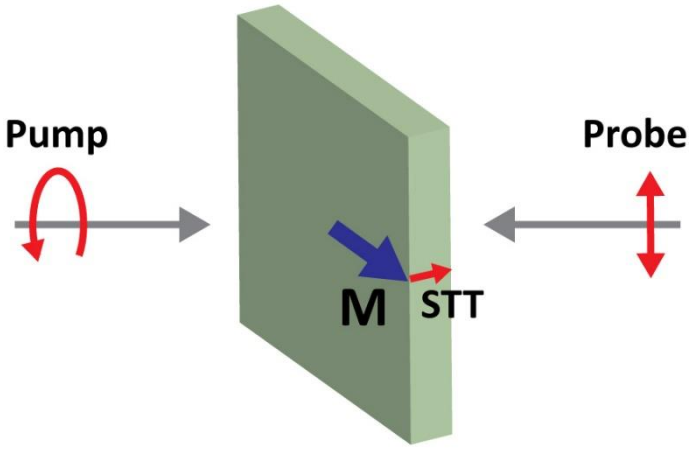

Fig. 7.1: Schematic representation of the optical STT. The magnetization of a ferromagnet lies in-plane direction. The circularly polarized pump beam creates spin-polarized electrons and subsequent STT in out-of-plane direction. The linearly polarized probe beam detects the magnetization dynamics of FM [10].

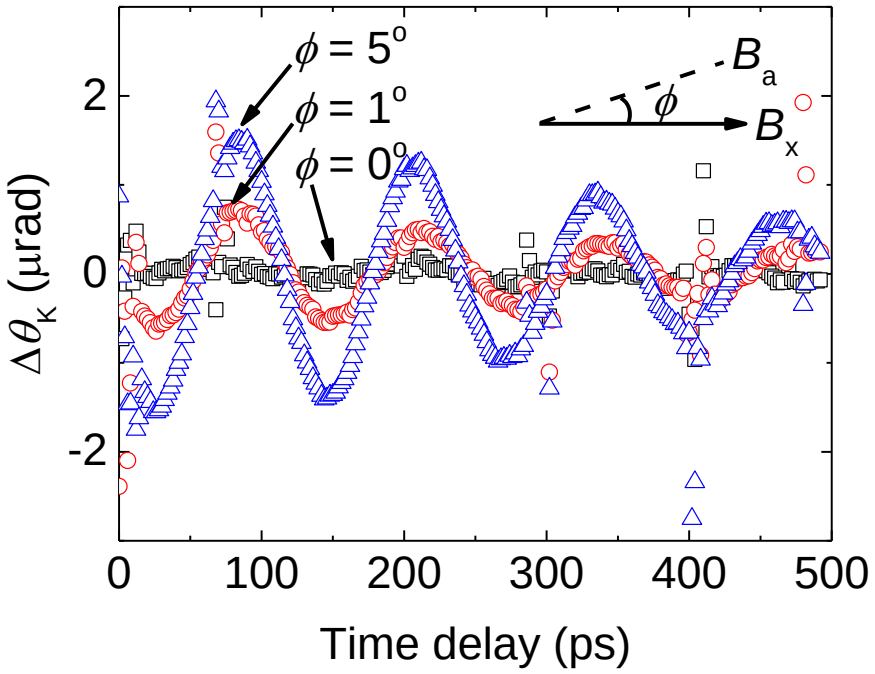

Fig. 7.2: The polar MOKE result with a linearly polarized pump beam. The ϕ is the angle between the magnetic field (B_x) and the crystalline anisotropy (B_a) [10].

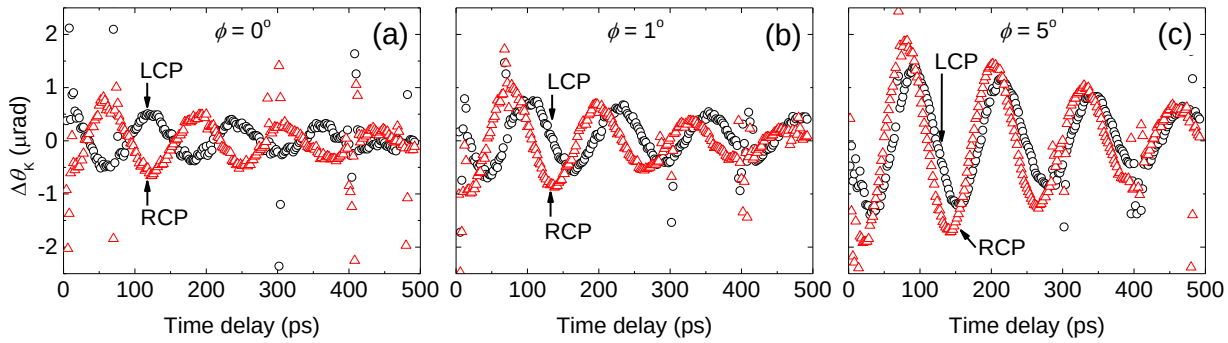

Fig. 7.3: The polar MOKE result with a circularly polarized pump beam with the ϕ of (a) 0°, (b) 1°, and (c) 5°. Black circles and red triangles are by the left (LCP) and right (RCP) circular polarized pump, respectively [10].

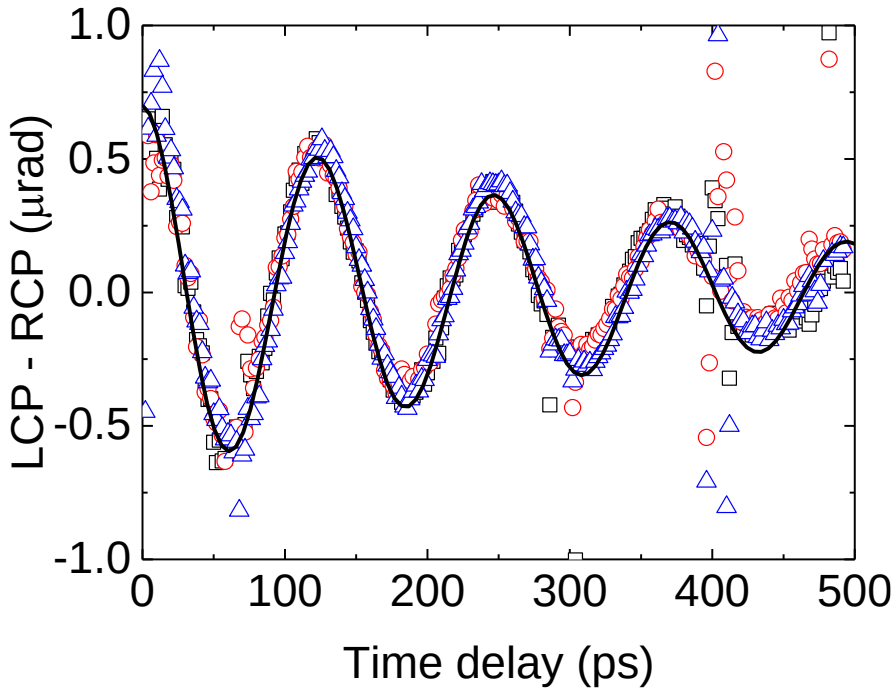

Fig. 7.4: The difference between LCP and RCP of Fig. 7.3. Black squares, red circles, and blue triangles are with the ϕ of 0°, 1°, and 5°, respectively. The black solid line is the fitting with a damped cosine function [10].

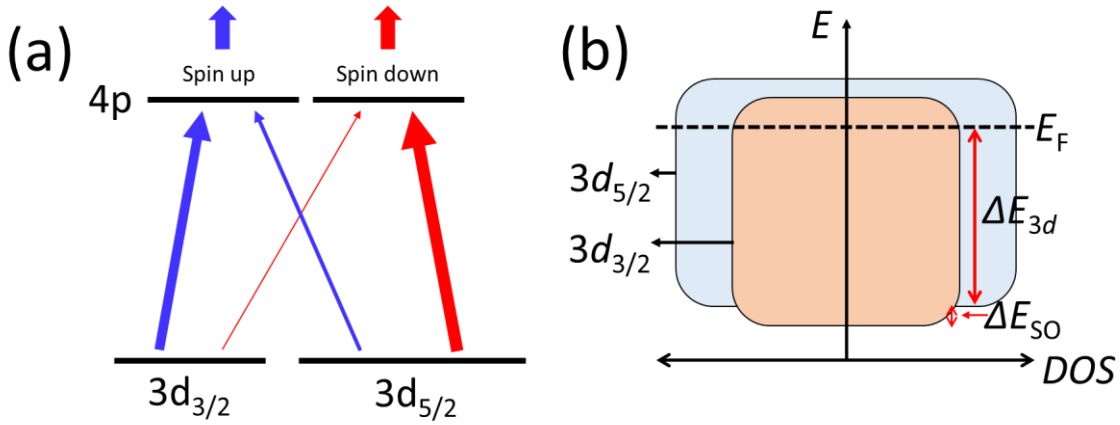

Fig. 7.5: (a) The spin polarization by the dipolar transition from the 3*d* to 4*p* states by the left circularly polarized light. The probability of transition is reflected by the thickness of the lines. (b) The energy splitting between the $3d_{3/2}$ and $3d_{5/2}$ bands due to the spin-orbit splitting. ΔE_{3d} is width of the 3*d* band, and ΔE_{SO} is the energy splitting by the spin-orbit coupling [10].

CHAPTER 8

CONCLUSION

In this dissertation, I have shown three distinct mechanisms for spin generation in metallic ferromagnet using ultrafast laser light: (i) demagnetization, (ii) spin-dependent Seebeck effect (SDSE), and (iii) optical helicity. For conclusion, I compare the energy efficiency of spin transfer torque for three mechanisms.

For the demagnetization-driven spin generation, the optimal structure is the FM1/NM/FM2. The total spin transfer torque applied to FM2 by demagnetization of FM1 is,

$$\int J_S dt \approx \frac{E_{abs}}{C} \times \frac{\Delta M}{\Delta T} \times \frac{1/\tau_{diff}}{1/\tau_{diff}+1/\tau_{relax}}, \tag{8.1}$$

where E_{abs} is the absorbed energy fluence on FM1, C is the heat capacity of FM1, $\frac{\Delta M}{\Delta T}$ is the relation between temperature rising and demagnetization of FM1, τ_{diff} is the time scale for the spin diffusion from FM1 to FM2, τ_{relax} is the time scale for the spin relaxation in FM1. The C could be the electron heat capacity when I consider only the electron-magnon coupling or it could be the total heat capacity (electron + phonon) when I consider both electron-magnon and electron-phonon couplings. The $\frac{\Delta M}{\Delta T}$ is material property and depends on the Curie temperature. The $\frac{1/\tau_{diff}}{1/\tau_{diff}+1/\tau_{relax}}$ critically depends on the spin relaxation time of FM1: for [Co/Pt], τ_{relax} is much smaller than τ_{diff}; for [Co/Ni], τ_{relax} is comparable to τ_{diff}; for Co, τ_{relax} could be much larger than τ_{diff}. Therefore, with Co as FM1, $\frac{1/\tau_{diff}}{1/\tau_{diff}+1/\tau_{relax}}$ could be close to one. When I use $C \approx$

3.75×10^6 J m^{-3} K^{-1} of Co, $\frac{\Delta M}{\Delta T} \approx 10^3$ A m^{-1} K^{-1}, and $\frac{1/\tau_{diff}}{1/\tau_{diff}+1/\tau_{relax}} \approx 1$, the total spin transfer torque per energy fluence is,

$$\frac{\int J_S dt}{E_{abs}} \approx 3 \times 10^{-4} \text{ A}. \tag{8.2}$$

To achieve a high spin transfer torque on FM2 out of demagnetization of FM1, it is important for FM1 to have a long spin relaxation time.

For the SDSE-driven spin generation, the optimal structure is the FM1/NM1/FM2/NM2, where FM1 acts as a heat absorbing layer and NM2 acts as a heat sinking layer. The total spin transfer torque applied to FM2 by SDSE of FM1 is,

$$\int J_S dt \approx E_{abs} \times \frac{C_{NM2}h_{NM2}}{C_{FM1}h_{FM1}+C_{NM2}h_{NM2}} \times \frac{\mu_B S_S}{eLT} \times \frac{1/\tau_{diff}}{1/\tau_{diff}+1/\tau_{relax}}, \tag{8.3}$$

where μ_B is the Bohr magneton, S_S is the spin-dependent Seebeck coefficient of FM1, e is the elementary charge, L is the Lorenz number, and T is the temperature of FM1. The $\frac{C_{NM2}h_{NM2}}{C_{FM1}h_{FM1}+C_{NM2}h_{NM2}}$ is the NM2's ability for heat sinking, and it could be close to one in an ideal case. When I use $\frac{C_{NM2}h_{NM2}}{C_{FM1}h_{FM1}+C_{NM2}h_{NM2}} \approx 1$, $S_S \approx 10$ μV K^{-1}, $T \approx 300$ K, and $\frac{1/\tau_{diff}}{1/\tau_{diff}+1/\tau_{relax}} \approx 1$, the total spin transfer torque per energy fluence is,

$$\frac{\int J_S dt}{E_{abs}} \approx 8 \times 10^{-5} \text{ A}. \tag{8.4}$$

To achieve a higher efficiency, a material design for much higher S_S is required.

For the optical helicity-driven spin generation, the optimal structure is the single FM1 layer. The total spin transfer torque applied to FM1 by circularly polarized light is,

$$\int J_S dt \approx E_{abs} \times \frac{\mu_B}{\hbar\omega} \times P_S \times \frac{\Delta E_{SO}}{\Delta E_{3d}} \times \frac{1/\tau_{dephase}}{1/\tau_{dephase}+1/\tau_{relax}}, \quad (8.5)$$

where $\hbar\omega$ is the photon energy, P_S is the spin polarization of the dipolar transition from the spin-orbit sub-band, ΔE_{SO} is the spin-orbit splitting of the 3*d*-band, ΔE_{3d} is the bandwidth the 3*d*-band, $\tau_{dephase}$ is the time scale for spins of hot electrons to diphase in FM, and τ_{relax} is the time scale for spins of hot electrons to relaxes FM. When I use $\hbar\omega \approx 1.58$ eV, $P_S \approx 0.3$ for the $3d_{3/2}$ sub-band, $\Delta E_{SO} \approx 0.08$ eV for the 3*d*-band of Co, $\Delta E_{3d} \approx 4$ eV for the 3*d*-band of Co, and $\frac{1/\tau_{dephase}}{1/\tau_{dephase}+1/\tau_{relax}} \approx 1$ for Co, the total spin transfer torque per energy fluence is,

$$\frac{\int J_S dt}{E_{abs}} \approx 2 \times 10^{-7} \text{ A}. \quad (8.6)$$

The energy efficiency of the optical helicity-driven spin generation is much smaller than those of demagnetization-driven and SDSE-driven ones because one photon has only one spin angular momentum and $\Delta E_{SO} << \Delta E_{3d}$ in most metallic ferromagnets.

APPENDIX A

SSE-DRIVEN SPIN ACCUMULATION

A.1 Introduction

The coupling of spin and heat gives rise to a new way to generate spin currents by thermal gradients. Slonczewski suggested the initiation of thermally-driven spin current in ferrite/ normal metal (NM) structures by the *s-d* exchange coupling [1]. The spin current is the result of the coupling between magnons of ferrite and electrons of NM at the ferrite/NM interface where magnons and electrons are out-of-equilibrium. This mechanism is now called spin Seebeck effect (SSE) and entirely different from the SDSE discussed in chapter 6 because it is magnon, not conduction electron, of ferrite that provides spins. Uchida *et al.* reported experimental observation of SSE in a Pt/YIG structure [2, 3]. They measured electrical voltage responses in the Pt strip with a steady-state temperature difference between Pt and YIG [2, 3]. The measurement was interpreted as that a spin current at Pt/YIG interface is converted to a transverse voltage due to inverse Hall effect.

The electrical measurement of SSE using inverse Hall effect is under controversy because the measured voltage signal could be contaminated by anomalous Nernst effect especially in transverse SSE experiment. Recently, it was reported even in longitudinal SSE experiment; the anomalous Nernst effect could exist due to magnetic proximity effect in NM in contact with ferrite [4]. To overcome this ambiguity, it is important to detect SSE using other than inverse Hall effect.

A.2 Experiment

Here I report optical detection of SSE in the NM (30 nm)/ Yttrium Iron Garnet (YIG) (20 nm ~ 3 μm) structure, where NM is Au or Cu (Fig. A.1). Heating by the ultra-fast pump optical pulse on NM creates a huge difference between the electron temperature of NM and magnon temperature of YIG during the pulse duration. This out-of-equilibrium between electrons and magnons leads to spin generation at the NM/YIG interface by SSE. The generated spins accumulate in NM with its characteristic spin relaxation time. The spin accumulation in NM can be detected optically by magneto-optical Kerr effect (MOKE) due to spin-orbit coupling of conduction electrons of NM [5].

I prepared four types of structures: *ex-situ*-Au-anneal-YIG, *ex-situ*-Au-plasma-YIG, *ex-situ*-Cu-anneal-YIG, and *in-situ*-Au-YIG. The "*ex-situ*" means that NM layers are deposited on separately prepared YIG films that is purchased from a commercial company, while the "*in-situ*" means that NM and YIG are deposited in the same sputter chamber. All *ex-situ* samples are made in the Korea Institute of Science and Technology, and the *in-situ* samples are made in the Ohio State University. The "anneal" means that YIG surface is clean by vacuum annealing at 300 ^{o}C before deposition of NM, and the "plasma" means that YIG surface is clean by Ar plasma for 10 minutes before deposition of NM. All NM layers are deposited by magnetron sputtering system, and thickness is 30 nm. The YIG thickness is 3 μm for the *ex-situ* samples and 20 or 100 nm for the *in-situ* samples.

I use pump-probe technique to create ultrafast temperature excursion of NM electrons and measure spin accumulation in NM on sub-picosecond timescales. The wavelengths of the pump and probe pulses are 785 nm, and the full widths at half maximum of the pump beam is ≈1.1 ps.

The pump beam is always incident on the NM side of the samples with a fluence of 9 J m^{-2}; the absorbed fluence is 0.3 J m^{-2}.

I apply an external magnetic field of ±0.3 T to the film-normal direction to align the magnetization of YIG and to generate spins in NM with the film-normal direction. This strong perpendicular magnetic field can reach the objective lens and then rotate the light polarization during the optical path through the objective lens. This Faraday rotation in the objective lens converts a reflectivity change, ΔR, to a polarization change, $\Delta\theta$, of probe light. Therefore, it is essential to block the magnetic field in front of the objective lens to prevent the MOKE signal from contamination by Faraday rotation in the objective lens. To block the magnetic field, I put a thin magnetic plate that has high permeability in between the sample and objective lens (Fig. A.2). This magnetic plate reduces the magnetic field reaching the objective lens from 150 to <10 Gauss.

After putting the magnetic plate, the signal from the Faraday rotation in the objective lens is reduced more than ten times smaller. In Fig. A.3, I compare the MOKE signal of the Au/sapphire sample. This reference sample has to have no MOKE signal because it has no magnetic layer. However, without the magnetic plate, there is a significant Kerr rotation due to the Faraday rotation in the objective lens. With the magnetic plate, the Kerr rotation becomes smaller than 0.03 μrad. To clearly measure the spin signal, the Kerr rotation driven by the spin accumulation in NM, should be much larger than this residual signal of ~0.03 μrad. All measurements of YIG samples are done with the magnetic plate.

A.3 Results and discussion

First, I show the result with the *ex-situ*-Au-YIG sample (Fig. A.4). The peak Kerr rotation is ~0.17 μrad at 1 ps then it decays to zero around 5 ps. Since the Kerr rotation driven by the

Faraday rotation in the objective lens is less than 0.03 μrad, the peak Kerr rotation of 0.17 μrad should come from spins of the sample. The peak Kerr rotation decreases to 0.05 μrad when I use interfacial treatment of Ar plasma instead of vacuum annealing. This result suggests that the quality of the Au/YIG interface is important for observation of the spin Seebeck effect [6].

With the Ar plasma treatment, the Kerr rotation does not decay to zero even after 5 ps (Fig. A.4 (b)). This residual signal is surprising given the short spin relaxation time of Au of 0.4 ps [5]. One possibility is that the measured Kerr rotation is not only from the spin accumulation in Au but also from the demagnetization of YIG. To verify this hypothesis, measurements with various thickness of Au in the Au/YIG structure is required.

Second, I compare the Au-YIG and Cu-YIG (Fig. A.5). Contrary to Au, Cu has a long spin relaxation time of around 16 ps [5]. Due to this long spin relaxation time, the spin accumulation in Cu should increase during the pump duration and then stay nearly constant up to ~16 ps. However, the actual measurement shows that the Kerr rotation has a maximum at ~0.5 ps, changes its sign at ~2 ps, and stays constant up to 10 ps. The spin accumulation in NM by spin Seebeck effect cannot explain this sign change because, in our case, a huge temperature excursion only exists in electrons of NM. One possibility would be that there is addition signal coming from demagnetization of YIG.

Third, I compare the *ex-situ* Au-YIG and *in-situ* Au-YIG (Fig. A.6). I expect the *in-situ* Au-YIG would have a better interfacial quality that the *ex-situ* Au-YIG, and consequently the spin accumulation in Au by the spin Seebeck effect would be higher with the *in-situ* Au-YIG. However, the actual measurement shows that the peak Kerr rotation is similar both *ex-situ* and *in-situ* samples. The critical difference is that the *in-situ* Au-YIG has its peak Kerr rotation at ~2 ps, which is 1 ps slower than that of the *ex-situ* Au-YIG. (For the in-situ Au-YIG, the thickness of YIG is 20 or 100

nm, but I find no difference with YIG thickness.) The spin Seebeck theory predicts the interfacial spin generation rate is proportional to the difference between the electron temperature of NM and magnon temperature of YIG [7]. Therefore, the time of the peak spin accumulation in Au is determined by the time of the peak electron temperature of ~0.5 ps and the spin relaxation time of ~0.4 ps of Au [5]. Summing these two time scales, the estimated time for the peak spin accumulation is ~1 ps. The peak time of ~2 ps disproves the simple estimation from the spin Seebeck theory and suggests there is a time-delaying mechanism.

Finally, I calculate the estimated spin accumulation in Au based on the spin Seebeck theory (Fig. A.7). The spin Seebeck theory predicts the spin generation at the NM/YIG interface is proportional to the difference between electron temperature of NM and magnon temperature of YIG and the spin mixing conductance of the interface [7],

$$G_S = \frac{\mu_B \gamma g_{\uparrow\downarrow} k_B}{\pi M_S V_a}(T_e - T_m), \tag{A.1}$$

where μ_B is the Bohr magneton, γ is the gyromagnetic ratio, $g_{\uparrow\downarrow}$ is the spin mixing conductance, k_B is the Boltzmann constant, M_S is the saturation magnetization of YIG, V_a is the coherence volume of YIG. Using $g_{\uparrow\downarrow}$ of 2.7×10^{18} m^{-2} [8], M_S of 1.4×10^{5} A m^{-1} [7], and V_a of $(1.3\times10^{-9}$ m$)^3$ [7],

$$G_S \approx 6 \times 10^{-4}(T_e - T_m). \tag{A.2}$$

Electron temperature (T_e) rising is determined by the absorbed energy and electronic heat capacity of NM (Fig. A.7 (a)). With the absorbed energy fluence of 0.3 J m^{-2}, the peak electron temperature of Au is around 200 K above the room temperature. After 0.5 ps, the electron of Au cools down by electron-phonon coupling. Phonon temperature (T_{ph}) of Au is much less than T_e of Au because heat capacity of phonon is much larger than the electron. Phonon and magnon

temperature of YIG should be less than T_{ph} of Au as heat transports from Au phonon to YIG phonon and YIG magnon. Parameters for thermal modeling is summarized in Table A.1.

The generated spins at the Au/YIG interface accumulate in Au by spin diffusion. The spin diffusion process is governed by diffusivity and spin relaxation time of Au. Given the small thickness and high diffusivity of Au, the spin accumulation is simply expressed as,

$$\frac{dM}{dt} = \frac{G_S}{h} - \frac{M}{\tau_S}, \tag{A.3}$$

where M is the spin accumulation in Au, and h is the thickness of Au, and τ_S is the spin relaxation time of Au. Combining temperature calculation of Fig. A.7 (a) and equations (A.2) and (A.3), I can calculate the spin accumulation in Au (Fig. A.7 (b)). The peak spin accumulation occurs at ~1 ps as expected and then decays quickly due to the short spin relaxation time of Au. The calculated spin accumulation exceeds 100 A m^{-1} at ~1 ps. The measured Kerr rotation with both *ex-situ* and *in-situ* Au-YIG samples is less than 0.2 μrad. Using the relationship between the spin accumulation and the Kerr rotation for Au ($\Delta\theta_K \approx 2.4 \times 10^{-8} \times \Delta M$) [5], the peak Kerr rotation of <0.2 μrad corresponds to the peak spin accumulation of <10 A m^{-1}. Therefore, there are discrepancies between theory and experiment not only in time response but also in signal magnitude.

A.4 Conclusion

Using ps pulses of laser light, I created a huge temperature difference between NM electrons and YIG magnons and measured spin accumulation in NM. The measurement cannot be explained by the spin Seebeck theory because the peak time differs by ~1 ps, and the amount of spin accumulation differs by orders of magnitude. To reveal the underlying mechanism for the measurement, further researches with different NM materials, various NM thicknesses, and different interfacial qualities are required.

A.5 References

1. J. C. Slonczewski, Phys. Rev. B **82**, 054403 (2010).
2. K. Uchida, J. Xiao, H. Adachi, J. Ohe, S. Takahashi, J. Ieda, T. Ota, Y. Kajiwara, H. Umezawa, H. Kawai, G. E. W. Bauer, S. Maekawa, and E. Saitoh, Nature Mater. **9**, 898 (2010).
3. K. Uchida, H. Adachi, T. Ota, H. Nakayama, S. Maekawa, and E. Saitoh, Appl. Phys. Lett. **97**, 172505 (2010).
4. D. Qu, S. Y. Huang, J. Hu, R. Wu, and C. L. Chien, Phys. Rev. Lett. **110**, 067206 (2013).
5. G.-M. Choi and D. G. Cahill, Phys. Rev. B **90**, 214432 (2014).
6. C. Burrowes, B. Heinrich, B. Kardasz, E. A. Montoya, E. Girt, Y. Sun, Y.-Y. Song, and M. Wu, Appl. Phys. Lett. **100**, 092403 (2012).
7. J. Xiao, G. E. W. Bauer, K. Uchida, E. Saitoh, and S. Maekawa, Phys. Rev. B **81**, 214418 (2010).
8. H. L. Wang, C. H. Du, Y. Pu, R. Adur, P. C. Hannel, and F. Y. Yang, Phys. Rev. Lett. **112**, 197201 (2014).
9. A. Tari, *The Specific Heat of Matter at Low Temperatures*. (Imperial College Press, London, 2003).
10. Y. S. Touloukian, ed. *Thermophysical Properties of High Temperature Solid Materials*. vol. 1 (Macmillan, New York, 1967).
11. S. M. Rezende, R. L. Rodriguez-Suarez, J. C. Lopez Ortiz, and A. Azevedo, Phys. Rev. B **89**, 134406 (2014).
12. G.-M. Choi, R. B. Wilson, and D. G. Cahill, Phys. Rev. B **89**, 064307 (2014).

A.6 Figures and Tables

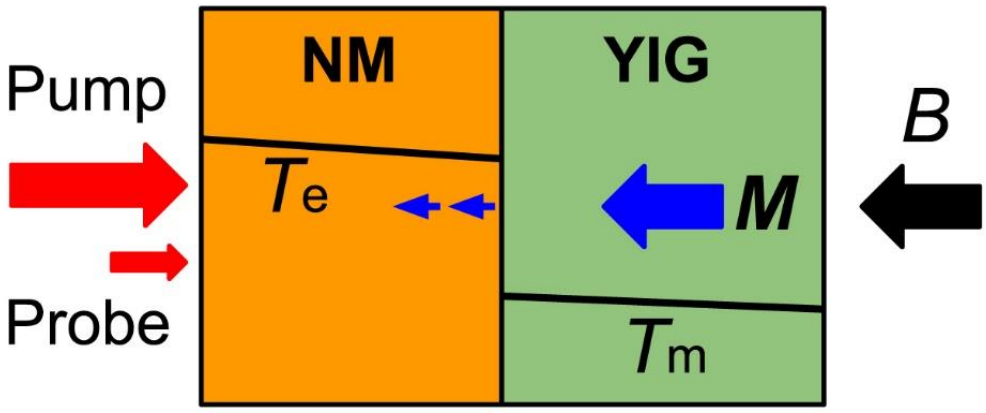

Fig. A.1: Conceptual diagram. The pump optical pulse is incident on the NM side and creates an ultrafast temperature excursion of electrons of NM. The temperature difference between electron (T_e) of NM and magnon (T_m) of YIG generates spins at the NM/YIG interface by SSE. An External magnetic field (B) of 0.3 T is applied to out-of-plane direction to align the magnetization of YIG to the out-of-plane direction. The generated spins are detected by probe light by MOKE.

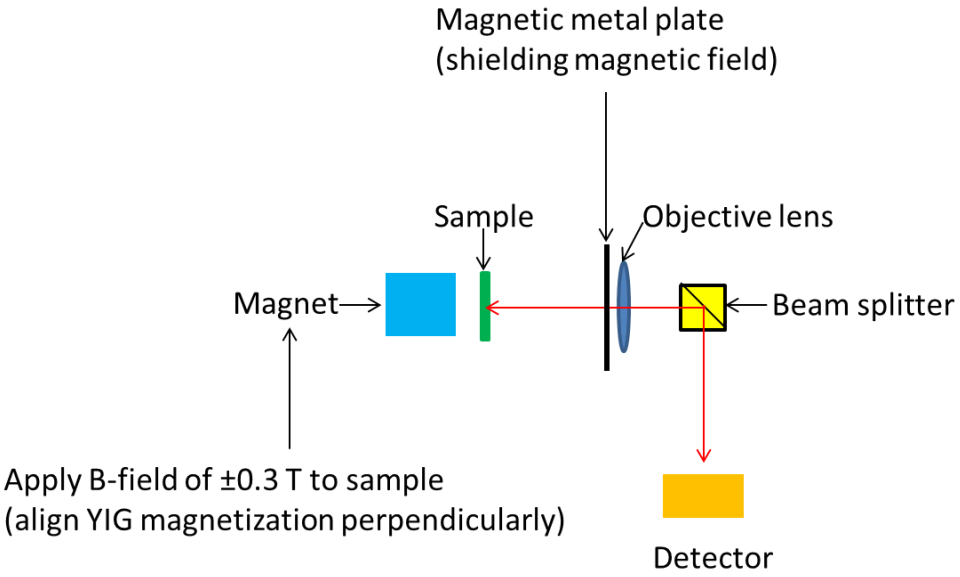

Fig. A.2: The schematic diagram of the measurement set-up. A permanent magnet is placed behind the sample to apply a perpendicular magnetic field of ±0.3 T to the sample. A magnetic plate is placed in between sample and objective lens to suppress magnetic on the objective lens.

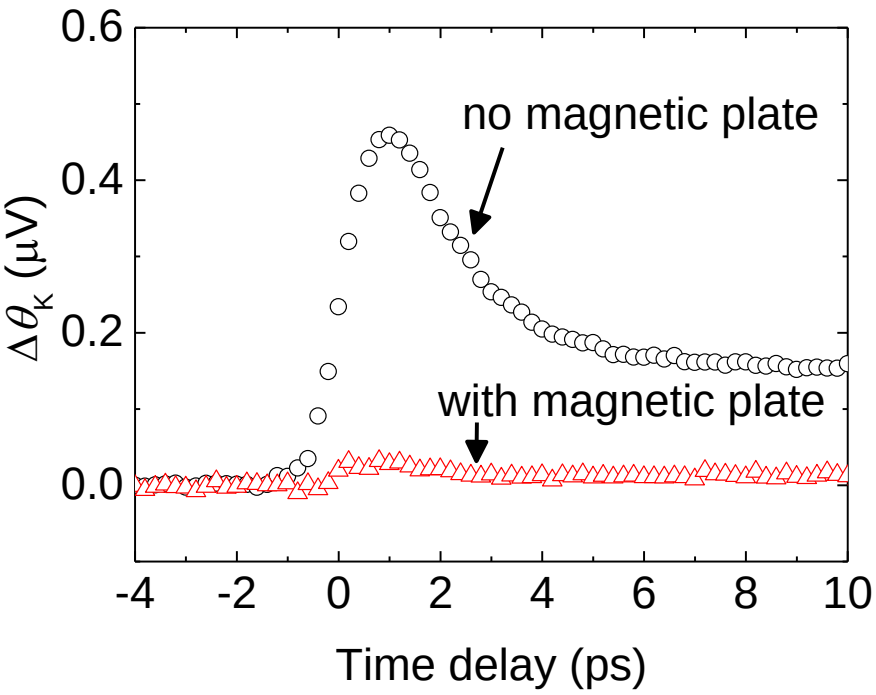

Fig. A.3: The Kerr rotation of the Au(30)/sapphire substrate. Without the magnetic plate, Faraday rotation in the objective lens produces a significant Kerr rotation. With the magnetic plate, the Kerr rotation driven by the Faraday rotation in the objective lens is reduced less than 0.03 μrad.

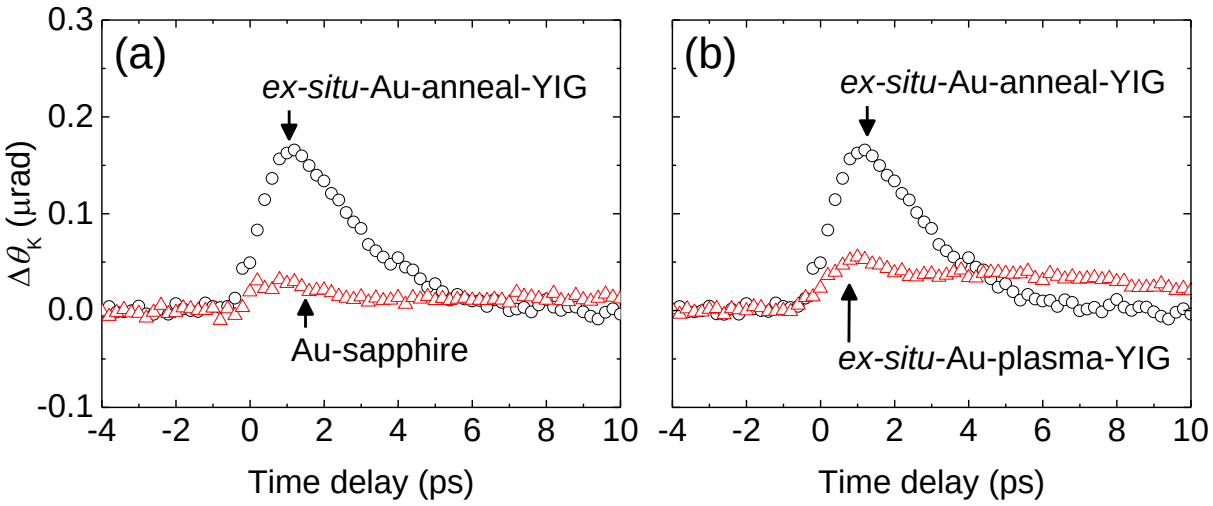

Fig. A.4: (a) The Kerr rotation of the *ex-situ*-Au-anneal-YIG (black circles) and Au-sapphire (red triangles). (b) The Kerr rotation of the *ex-situ*-Au-anneal-YIG (black circles) and *ex-situ*-Au-plasma-YIG (red triangles).

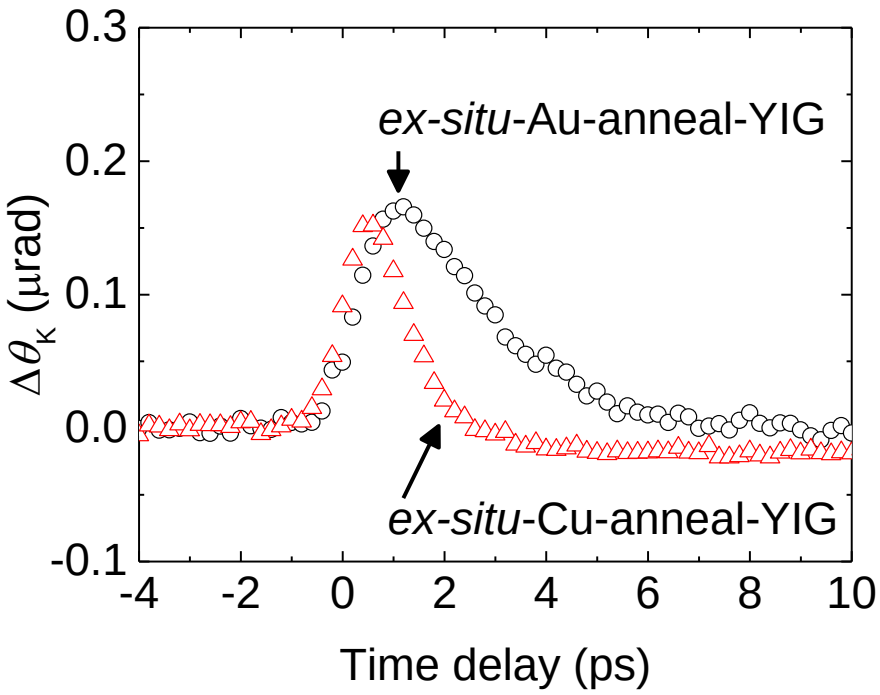

Fig. A.5: The Kerr rotation of the *ex-situ*-Au-anneal-YIG (black circles) and *ex-situ*-Cu-anneal-YIG (red triangles).

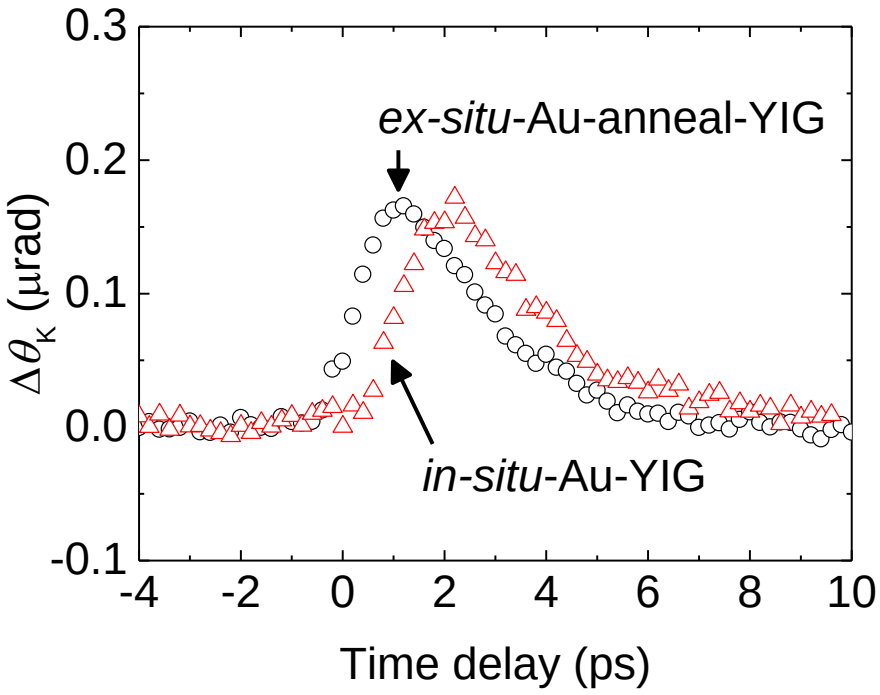

Fig. A.6: The Kerr rotation of the *ex-situ*-Au-anneal-YIG (black circles) and *in-situ*-Au-YIG (red triangles).

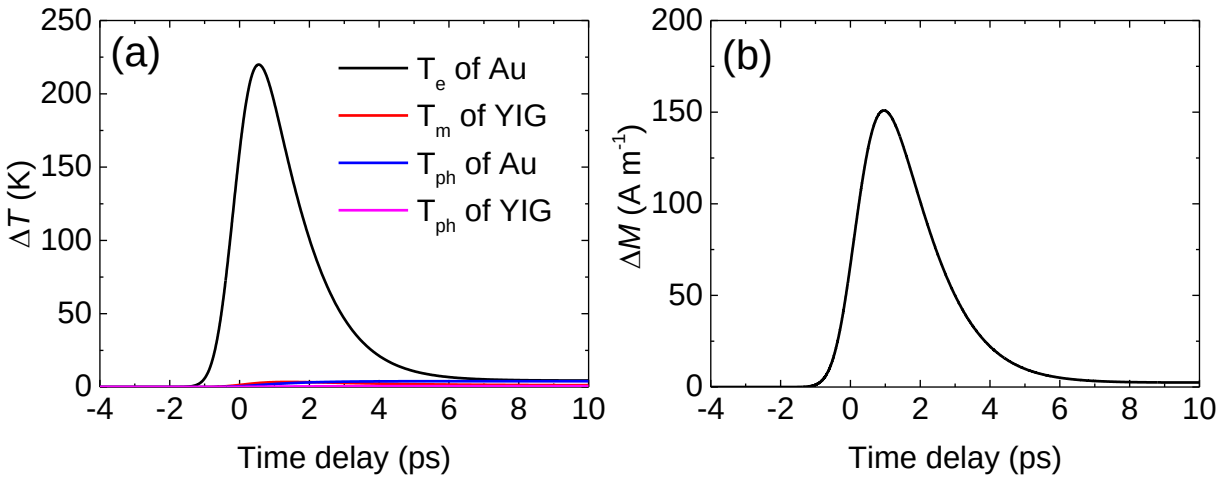

Fig. A.7: (a) The calculated temperature of Au electron, Au phonon, YIG magnon, and YIG phonon at the interface of the Au (30)/ YIG structure. (b) The calculated spin accumulation in Au due to the temperature evolution of (a) based on the equation (A.3).

Table A.1: Parameters for the thermal modeling: C is the heat capacity, Λ is the thermal conductivity, and g is the electron-phonon or magnon-phonon coupling parameter.

	Au electron	Au phonon	YIG magnon	YIG phonon
C (10^6 J m^{-3} K^{-1})	$68 \times T_e$ [a]	2.47 [b]	0.001 [c]	2.9 [c]
Λ (W m^{-1} K^{-1})	200 [d]	3 [e]	5 [c]	4 [f]
g (10^{16} W m^{-3} K^{-1})	2.2 [e]		0.002 [c]	

[a] Reference 9.
[b] Reference 10.
[c] Reference 11.
[d] Obtained by from electrical conductivity and Wiedemann-Franz law.
[e] Reference 12.
[f] Obtained as fitting parameters for thermal transport analysis.